FROM: MODERN PULSED AND CONTINUOUS-WAVE ELECTRON SPIN RESONANCE
EDITED BY: Larry Kevan and Michael Bowman
Wiley, NY (1990)

3 Two-Dimensional Electron Spin Resonance

JEFF GORCESTER,* GLENN L. MILLHAUSER,† and JACK H. FREED
Department of Chemistry, Baker Laboratory, Cornell University, Ithaca, New York

* Present address: Rijksuniversiteit Leiden, Huygens Laboratorium, Niels Bohrweg 2, 2300 RA Leiden, The Netherlands.
† Present address: Dept. of Chemistry, University of California, Santa Cruz, CA 95064.

1. INTRODUCTION

In 1979 one of us wrote a review in which a general formulation of time-domain ESR was described [1], and it was applied to saturation recovery ESR spectroscopy [1]. In the same volume, Stillman and Schwartz [2] provided a summary of the initial efforts in utilizing this formulation for ESR spin echoes and ENDOR spin echoes. Since that time there have been many experimental and theoretical developments on the subject of time-domain ESR, spin relaxation, and motional dynamics. We focus primarily (but not exclusively) in this chapter on the developments in time-domain ESR that pertain to studying molecular motions in condensed phases. Whereas the initial studies were based on spin-echo measurements of T_2 (or T_M, the phase-memory time) and T_1, summarized in part in Section 2, the new developments have emphasized the advantages of two-dimensional spectroscopies that enable one to resolve more of the spectral and relaxation details that relate to motions.

These developments have occurred in two stages. Millhauser and Freed [3], realized that a conventional electron spin-echo (ESE) spectrometer could readily be modified to produce magnetic-field swept ESE decays, and then a single fast Fourier transformation (FFT) yields a 2D spectrum. The first type, described in Section 3, provides a mapping of the homogeneous line shapes across the inhomogeneous ESR spectrum, and it is very sensitive to the details of the motional dynamics. A second type, described in Section 4, provides a mapping of the cross-relaxation rates from each point in the spectrum and is also very informative of the motional dynamics.

The epitome of techniques for cross-relaxation studies is ELDOR, because one observes the cross-relaxation from one spectral position to another position, and (for short times) this is directly related to the transition probability between these spectral positions [4]. We also describe in Section 4 a simple spin-echo ELDOR technique based upon rapidly stepping the dc magnetic field between pumping and observing resonant positions [5, 6]. The natural representation for such an experiment is two-dimensional with respect to pumping and observing frequencies. In Section 5, we describe how modern Fourier transform (FT) ESR techniques permit a direct realization of this 2D ELDOR technique by analogy to modern 2D NMR. We also describe ESR realizations of the well-known NMR two-dimensional spectroscopies, correlation spectroscopy (COSY) and spin-echo correlation spectroscopy (SECSY), and consider their utility. The

introduction of 2D FT-ESR by Gorcester and Freed represents the second stage in the development of 2D ESR [7, 8].

Special instrumentation and techniques are required to perform these new 2D FT-ESR experiments, and our spectrometer is described in Section 6. The spectrometer is of a flexible design permitting both 2D FT and 2D field swept experiments to be performed. Specific experimental requirements and the challenges of 2D FT-ESR are described in Section 7, along with our current solutions. In an appendix we summarize the time-domain data-processing techniques, based upon linear prediction with singular value decomposition (LPSVD), which have proven to be of such great value in all of our 2D ESR experiments [9, 10].

It is hoped that this chapter will enlighten the reader on the great range of possible applications of 2D ESR, especially with respect to the study of molecular dynamics in fluids, and that it will serve as a basis for initiating such experiments.

Other recent reviews focus on related matters. These include the application of ESR time-domain methods for the study of surfaces [11], their applications to biophysics [12], and to related studies of rotational dynamics of fluids [13]. The theoretical and computational methods for extracting the molecular dynamics from the 1D and 2D ESR spectra have also been reviewed recently [14], and a powerful computer program useful for simulating 1D (and 2D) slow-motional spectra is now readily available [15].

2. ELECTRON SPIN ECHOES AND MOTIONAL DYNAMICS

Figure 1 summarizes the most typically used ESE pulse sequences. These include spin echoes, stimulated echoes, inversion–recovery, and ELDOR echoes.

2.1 Phase Memory Times and Rotational Correlation Times

When an echo technique [16–20] is applied to spin systems with inhomogeneously broadened cw-ESR lines (e.g., due to unresolved or partially resolved proton shf interactions in the case of nitroxides) the measured phase memory time T_M is equal to T_2, the homogeneous line width of a single spin packet [20–23]. The ESE studies in liquids show good agreement with the motionally narrowed line widths extracted by cw techniques (cf. Fig. 2). An especially interesting observation [21] was that in the slow-motional regime, for $\tau_R \approx 10^{-7}$ to 10^{-6} s, where τ_R is the rotational correlation time, the phase memory time T_M was found to be proportional to τ_R^{α} with $\alpha \approx 0.5$–1 (cf. Fig. 2). Simple arguments suggested this was to be expected. That is, in the slow-motional regime, reorientational jumps should lead to spectral diffusion wherein each jump takes place between sites of different resonant field. This would be an uncertainty-in-lifetime broadening that is analogous to the slow exchange limit in the classic two-site case, and it contributes to T_M. The broadening would then

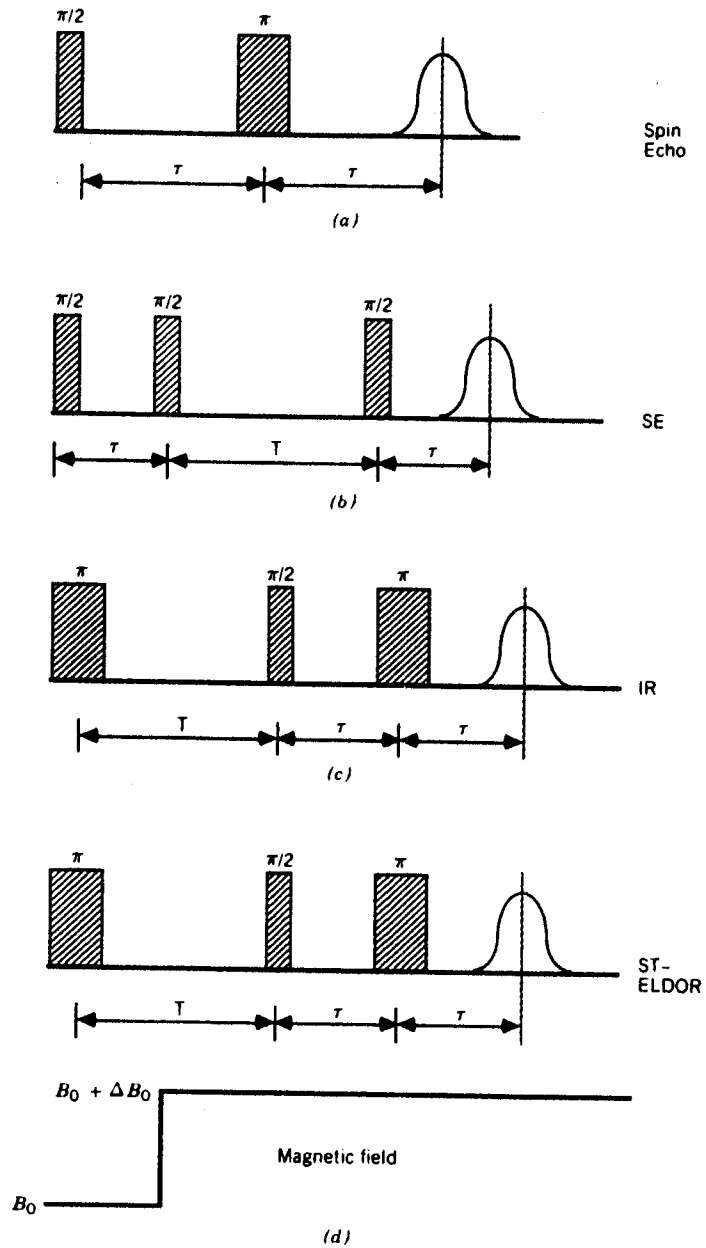

Fig. 1. Typical spin-echo pulse sequences: (*a*) Hahn spin echo, (*b*) stimulated echo, (*c*) inversion recovery, and (*d*) ST-ELDOR echoes.

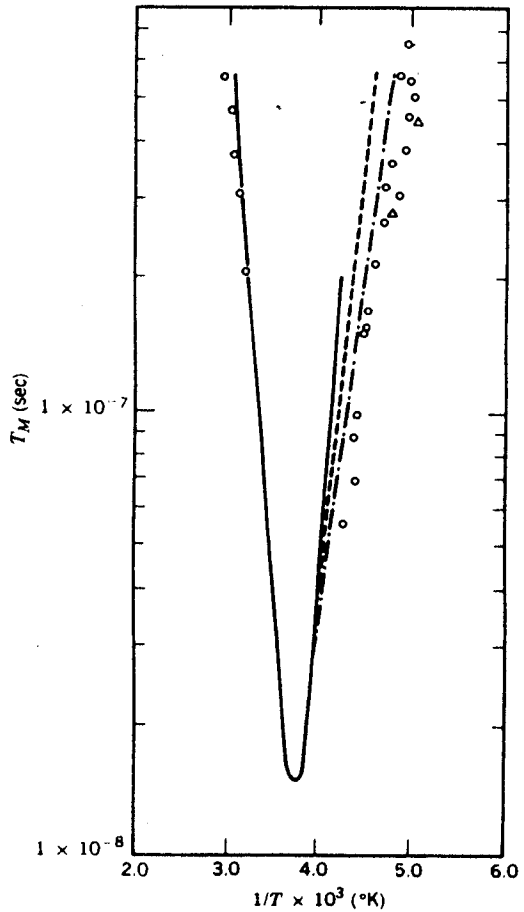

Fig. 2. Plot of T_2 (or T_M) vs. T^{-1} for the nitroxide probe Tempone in 85% glycerol/H_2O. The circles show data collected from spin-echo experiments; the triangles show T_2 as measured from the center maximum of 2D ESE spectra. The different lines show T_2 calculations from the same spectral region for the different models of jump diffusion (——), free diffusion (– – –), and Brownian diffusion (– · –). The calculations employed the values of τ_R extrapolated from the fast-motional regime. From Ref. 3.

be given by τ_R^{-1}, the jump frequency. This result suggested that studies of the ESE T_M in slow-motional spectra would supply complementary information on motional dynamics to that from cw line shape studies. A rigorous theoretical basis was established for the analysis of slow-motional ESE in order to interpret such experiments with confidence [22]. The theory may readily be computed

with the newer cw-ESR slow-motional computer programs [15]. This emphasizes that echoes relate to the same type of motional effects as do the cw line shapes, but with much better resolution.

The theoretical results on simple $\pi/2$-τ-π-τ echoes (cf. Fig. 1*a*) clarified the potential of ESE in the study of molecular dynamics. It was concluded that careful study of the variation of T_M (i.e., T_2) across the spectrum would be a useful way to proceed in applying ESE to this problem. This led to the two-dimensional spectroscopy approach outlined in Section 3.

2.2 Carr–Purcell Sequences

An important variant on the simple spin echo is the Carr–Purcell (CP) sequence: $\pi/2$-$(\tau$-π-$\tau)_n$, where the π pulse is applied n times giving rise to n echoes at times $2m\tau$, $m = 1, 2, \ldots, n$, and one detects the decay of the echo train for given τ to obtain the decay constant T_M^C. The feasibility of such experiments by ESE was demonstrated by Eliav and Freed [24], and the theory is given by Schwartz et al. [22]. It was shown that such CP sequences are potentially more informative than simple two-pulse echoes. In the latter, usually only a single T_M is obtained at each spectral position, while in the former a whole set of $T_M^C(\tau)$ versus τ would, in principle, be obtained, which could be used to explore motional dynamics in greater detail. This is particularly true as τ becomes comparable to τ_R, which results in $T_M^C > T_M$ [22]. In fact, as $\tau/\tau_R \to 0$, the successive π pulses repeatedly reverse the electron spin precession so rapidly that the hyperfine and g-tensor anisotropy is (coherently) averaged more effectively by these π pulses than it can be randomized by the slow tumbling. (This is analogous to the NMR case wherein the CP sequence is used to remove the effect on T_2 of translational diffusion in an inhomogeneous applied field.)

2.3 ESEEM and Motion

The theory for electron spin-echo envelope modulations (ESEEM) has been reasonably well developed and is summarized elsewhere in the volume (cf. Chapter 5 by Kevan). It enables the measurement of extremely weak electron–nuclear dipolar interactions such as exist between the unpaired electron of a nitroxide label and the neighboring deuterons (protons). While ESEEM has primarily been used for structural studies, it can also be utilized in the study of motional dynamics. In general, motion averages out the ESEEM. A general theoretical approach to the problem of how motion averages ESEEM has been developed [22, 23]. We find in model experiments [23] that for the nitroxide probe PD-Tempone, where the ESEEM are due to the weak deuteron shf splittings, that the patterns change significantly for τ_R values ranging from about 10^{-4} to 10^{-7} s, although residual effects may be seen for somewhat faster and slower motion. Note that the deuteron shf is significantly smaller (e.g., $A_z \approx 100$ mG) than the ^{14}N hf term ($A_z \approx 30$ mG). Thus, it will be averaged out by motions that are considerably slower than required for normal ESE spectra.

Effects from deuterons directly on PD-Tempone are averaged by any reorientation. Deuterons of the solvent can also cause ESEEM in the rigid limit [25], which would be averaged by the relative translation and rotation of solvent and solute molecules.

We now inquire as to how a two-dimensional technique enables one to obtain maximum information from T_2 measurements. (We will refer to the T_M as T_2 below.)

3. 2D ESE STUDIES OF T_2 VARIATION ACROSS THE SPECTRUM

3.1 Theory

The 2D ESE method for studying T_2 variations across the spectrum is based upon the theoretical study of ESE and slow motions by Schwartz et al. [22]. One begins with the time-dependent form of the stochastic Liouville equation (SLE)

$$\dot{\rho}(\Omega, t) = i[\mathscr{H}[(\Omega), \rho(\Omega, t)] - \Gamma_\Omega[\rho(\Omega, t) - \rho_0(\Omega)] \tag{1}$$

where $\rho(\Omega, t)$ is the density matrix with equilibrium value $\rho_0(\Omega)$, $\mathscr{H}(\Omega)$ is the spin Hamiltonian, Γ_Ω is the diffusion operator, and Ω represents the orientation of the molecule. Following the well-known procedure of expanding $\rho(\Omega, t)$ in terms of eigenfunctions of the diffusion operator Γ_Ω, taking spin matrix elements, and transforming into a rotating-frame coordinate system, we find the equation of motion for the vector of expansion coefficients to be

$$\dot{\mathbf{C}}(t) = -\mathbf{B}\mathbf{C}(t) \tag{2}$$

$\mathbf{B}$ is a time-independent evolution matrix derived from the stochastic Liouville operator in the rotating frame [1, 2]. This equation holds for conditions of free precession, that is, no radiation term in the Hamiltonian. Starting with the solution to Eq. 2 and the initial conditions as determined by the 90° pulse (designated by the vector $\mathbf{U}$) one has

$$\mathbf{C}(\tau) = e^{-\mathbf{B}\tau}\mathbf{U} \tag{3}$$

Applying the effects of the 180° pulse and then allowing evolution for the time period $\tau + t'$ (where $t' > 0$), the total time evolution of the system is described by

$$\mathbf{C}(2\tau + t') = e^{-\mathbf{B}(\tau + t')}e^{-\mathbf{B}^*\tau}\mathbf{U}^* \tag{4}$$

The averaged signal is written as

$$s(2\tau + t') = \mathrm{Re}\{\mathbf{U}^{tr}e^{-\mathbf{B}(\tau + t')}e^{-\mathbf{B}^*\tau}\mathbf{U}^*\} \tag{5}$$

which may be rewritten (after the matrix $\mathbf{B}$ is diagonalized) as a sum of complex exponentials. That is, the observed echo signal s is given by

$$s(2\tau + t) \propto \mathrm{Re}\sum_{j,k} a_{kj}\exp[-(\Lambda_k + \Lambda_j^*)\tau]\exp(-\Lambda_k t) \tag{6}$$

where τ is the time between the $\pi/2$ and π pulses (cf. Fig. 1*a*) and where $2\tau + t$ is the time period measured from the initial pulse. The echo maximum is expected at time 2τ. In Eq. 6, Re represents the real part of the complex function to its right and Λ_j and Λ_k are complex eigenvalues of $\mathbf{B}$ discussed below. Equation 6 can best be understood in terms of the concept of the *dynamic spin packet* (DSP). That is, in the rigid limit, the inhomogeneously broadened ESR spectrum from a polycrystalline (or glassy) sample is made up of the broad envelope of contributions from many, many (actually a continuum of) spin packets, each one resonating at a definite frequency and associated with the spins on molecules oriented at the appropriate angle with respect to the static magnetic field. The rigid limit spectrum is determined in the usual way in terms of the g tensor and hyperfine tensor anisotropies.

As the rotational motion increases, each spin packet in the continuum will "interact" with nearby spin packets, since the motion will transform molecules contributing to one spin packet into contributors to another at a different orientation. As a result of this coupled behavior of the original (i.e., rigid-limit) spin packets, there will be new "normal-mode" solutions, the DSPs, which will be linear combinations of the original spin packets. The physics of the problem is described by the stochastic Liouville equation [14, 22], which simultaneously includes the reversible quantum-mechanical spin dynamics and the irreversible molecular dynamics (usually treated classically). Typical spin Hamiltonians and dynamical models are summarized elsewhere [14, 22]. The eigenvectors of the stochastic Liouville operator are the DSPs, and the Λ_j in Eq. 6 are the corresponding eigenvalues in the rotating frame. The imaginary parts $\mathrm{Im}(\Lambda_j)$ represent the resonance frequencies of the associated DSP (i.e., $\omega_j \equiv \mathrm{Im}(\Lambda_j)$), while the real parts $\mathrm{Re}(\Lambda_j)$ represent the corresponding natural or homogeneous widths and are associated with the observed $T_{2j} \equiv [\mathrm{Re}(\Lambda_j)]^{-1}$. (Note that the asterisk in Eq. 6 represents a complex conjugation, which requires a simple generalization [22] if echo envelope modulation is to be considered.) In general, the relative weights of the DSPs given by the "diagonal" coefficients a_{kk} in Eq. 6 and the "beats" between pairs of DSPs given by the "off-diagonal" coefficients a_{kj} $(k \neq j)$ have a complicated dependence upon the form of these "normal modes" and of the spin transition moments as averaged over the equilibrium ensemble of molecular orientations. That is,

$$a_{kj} = \sum_{i,l,m} U_i O_{ik} O_{il} O_{ij}^* O_{mj}^* U_m^* \tag{7}$$

where $\mathbf{O}$ is the complex orthogonal matrix that diagonalizes $\mathbf{B}$. Hence, its

columns are just the components of the dynamic spin packets in the original basis set. Also, U is the vector of appropriately averaged spin-transition moments.

Near the rigid limit the elements of the complex orthogonal matrices O become nearly real [14, 15, 22]. Taking advantage of the properties of real orthogonal matrices we find

$$a_{kj} \simeq \delta_{kj} \sum_{lm} U_l O_{lj} O_{mj} U_m^* \tag{8}$$

Thus, the only contributing terms to Eq. 6 are those where $k = j$. In general, U is purely imaginary. Thus, Eq. 8 can be written compactly as

$$a_{kj} \simeq (\mathbf{O}^{\mathrm{T}}\mathbf{U})_j^2 \delta_{kj} \tag{9}$$

When Eq. 9 applies, Eq. 6 becomes

$$s(2\tau + t) \propto \sum_j a_{jj} \exp[-2\mathrm{Re}(\Lambda_j \tau)] \exp[-\mathrm{Re}(\Lambda_j t)] \cos[\mathrm{Im}(\Lambda_j t)] \tag{10}$$

Thus, in a "two-dimensional" plot of s versus the two independent variables τ and t, the t dependence includes both the resonance frequency of each DSP and its $T_{2,j}$. If we set $t = 0$ and step out τ, then we obtain the echo envelope as a superposition of exponential decays corresponding to the different $T_{2,j}$ values from each DSP contributing appreciably to the signal. However, such a result would be difficult to disentangle. Instead, let us take advantage of the additional resolution provided by two-dimensional spectroscopy. Let us perform a double Fourier transform of Eq. 10, recognizing, however, that in the near-rigid-limit cw ESR spectrum the line width for each DSP will largely be masked by various sources of inhomogeneous broadening such as unresolved shf interactions and site variations in the spin-Hamiltonian parameters. We therefore assume a Gaussian inhomogeneous width $\Delta \gg T_{2,j}^{-1}$. This yields the two-dimensional spectrum given by

$$S(\omega, \omega') \propto \sum_j a_{jj} \frac{T_{2,j}}{1 + \omega^2 T_{2,j}^2} \exp\left[-\frac{(\omega' - \omega_j)^2}{\Delta^2}\right] \tag{11}$$

which is a sum of Lorentzians along the ω axis (the FT of τ) and the sum of Gaussians along the ω' axis (the FT of t). But more importantly, we have separated out the role of the relaxation of each spin packet given by its $T_{2,j}$, which is plotted along the ω axis, from its resonance position in the spectrum given along the ω' axis. In fact, for $\omega = 0$ we recover the expression for the cw line shape (with Gaussian inhomogeneous broadening) along the ω' axis (except for the factor $T_{2,j}$ in the sum over j). Thus, this separation allows us to *observe how the $T_{2,j}$ vary across the whole spectrum.* In other words, we have succeeded

in resolving the different dynamic behavior of the various spin packets, subject, however, to the resolution limit due to the inhomogeneous broadening, Δ. Examples of such 2D ESE spectra appear in Fig. 3.

The actual experimental technique that has been utilized by Millhauser and Freed (MF) [3] is to sweep through the static magnetic field B_0 very slowly, but with a microwave-field intensity B_1 small enough that only DSPs associated with widths well within the inhomogeneous width Δ are effectively rotated by the pulses. MF show that Eq. 11 applies to their experiment provided that the following set of inequalities apply:

$$\gamma B_s > \Delta \gg \gamma B_1 \gg T_{2,j}^{-1} \tag{12}$$

where γB_s is the full extent of the spectrum. In this format, one sweeps through B_0 and observes the echo height at 2τ; that is, one obtains an *echo-induced ESR spectrum* for each value of τ. This provides an $S(\tau, \omega')$ such that the FT in t is automatically obtained. Then an FT in τ is performed after the experiment is repeated for a sufficient number of values of τ to obtain the form of Eq. 11. This technique has the advantage of simplicity, a minimum of experimental artifacts, and only low-power microwave pulses are required. However, it is time-

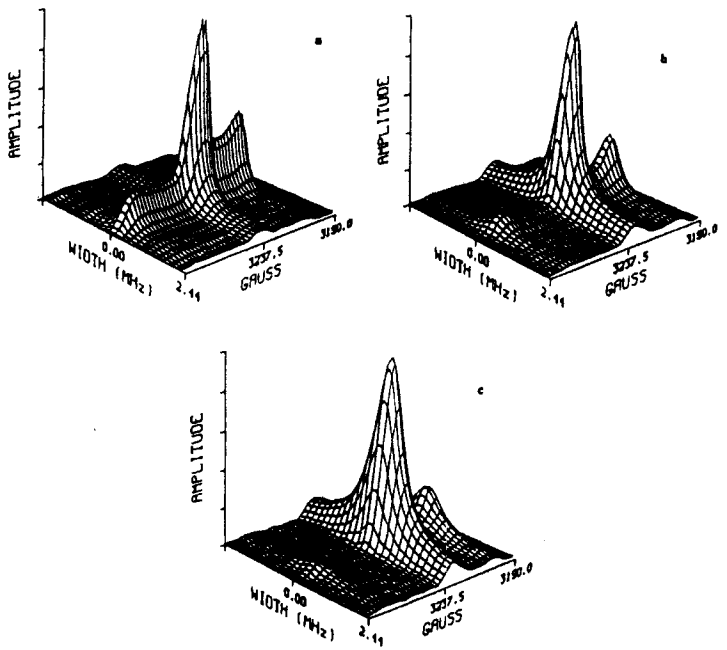

Fig. 3. Two-dimensional spectra for Tempone in 85% glycerol/H_2O at (*a*) − 100 °C, (*b*) − 75 °C, (*c*) 65 °C, after Fourier filtering and Fourier transforming. From Ref. 3.

consuming, typically requiring about 5–10 h for a complete set of 2D data. One may use a standard ESE spectrometer, or the more sophisticated one described in Section 6. We show in Section 5 that modern techniques now permit such an experiment to be performed with large enough B_+ pulses such that the whole spectrum can be irradiated. For this newest technique, the relevant inequalities would be

$$\gamma B_1 \geq \gamma B_+ > \Delta \gg T_{2,j}^{-1} \tag{13}$$

in order that Eq. 11 be obtained after a double FT in τ *and* t. This newest technique is more difficult. Nevertheless, by removing the need to sweep slowly through B_0, but instead to gather the *whole* spectrum after each echo sequence, at *the least* there is an order-of-magnitude savings in time.

3.2 Examples

The actual data are most usefully displayed not by the full 2D representation, but by normalized contours. These are produced by dividing $S(\omega, \omega')$ by the *zero MHz slice* (i.e., $S(0, \omega')$) to normalize the 2D spectrum and then to display the constant contour lines (and also the zero MHz slice). A set of horizontal lines imply that there is no T_2 variation across the spectrum, whereas contour lines with curvature indicate the presence of at least some variation. We show in Fig. 4 the contours and zero MHz slices obtained from the results in Fig. 3. Those for -100 °C represent the rigid limit and show no T_2 variation, whereas those for -75 and -65 °C, do show variation resulting from the molecular reorientation. One finds that these contours are very sensitive, not only to the rate of reorientation but also to the model of molecular reorientation, (e.g., whether it is by jumps, free diffusion, or Brownian motion) with different characteristic *patterns* for each! We show in Fig. 5 an actual experimental demonstration of the sensitivity to motional anisotropy by comparing the results for Tempone, which tumbles nearly isotropically versus that for CSL, whose motion is anisotropic. While the T_2's are comparable, the contour shapes are significantly different, emphasizing the large anisotropy for CSL.

It should also be emphasized that Fig. 5 shows patterns that are consistent with a Brownian reorientation model. In the general theoretical analysis of this experiment, MF show that Brownian reorientation, which occurs by infinitesimal steps, will lead to a T_2 variation, because of the different sensitivity of different spectral regions to a small change in molecular orientation (i.e., $dS(\omega')/d\theta$ varies across the spectrum). On the other hand, reorientation by substantial jumps would not show any T_2 variation.

We have also applied the 2D ESE technique to oriented phospholipid samples [26], and our analyses show them to be particularly sensitive to the orienting potential as well as details of the dynamics. We wish to emphasize the importance of this sensitivity. Our studies with CSL in the oriented lipid samples have shown that in the very slow-motional region, where cw-spectral simulations are only slightly sensitive to motion, it is very difficult to obtain a

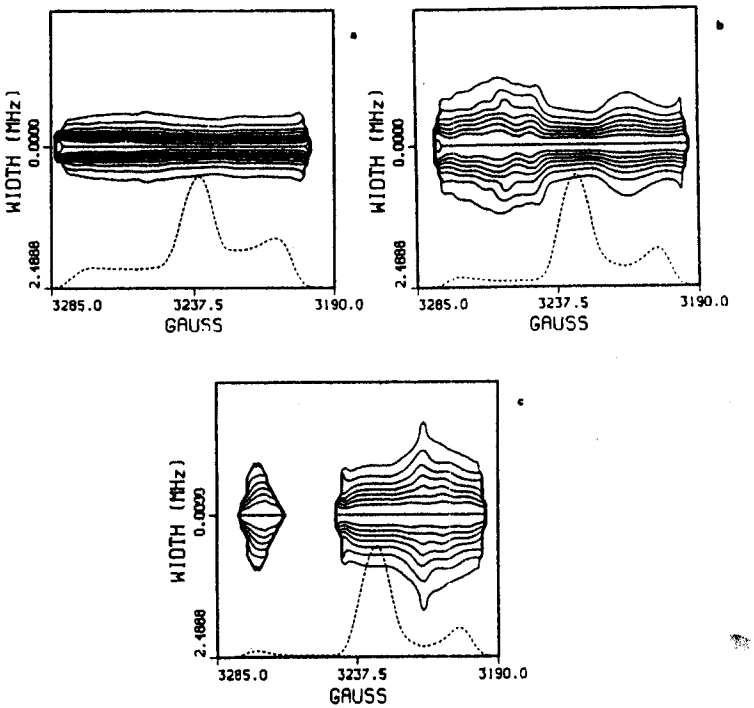

Fig. 4. The experimental normalized contours at (*a*) -100 °C, (*b*) -75 °C, (*c*) -65 °C. Each successive contour line represents a 10% change relative to the normalized maximum. Estimated T_2 values calculated from widths at 3235 G are 0.70, 0.44, 0.44, and 0.28 μs, respectively. Shown at the bottom of each plot is the 0 MHz spectrum (see text). In this and the succeeding figures the vertical lines at each end closing the contours are artifacts of the plotting routines and should be ignored. From Ref. 3.

unique set of parameters characterizing the system under study [26]. In fact, temperature-dependent inhomogeneous broadening may dominate the cw-ESR line shapes in the very slow-motional region. In the cw line-shape analysis, there is a danger of misinterpreting this effect as due to motion! The 2D ESE results are much more sensitive to these matters, as is illustrated in the simulations of Fig. 6. In Fig. 6*a* we show a cw-ESR simulation for high ordering ($S = 0.87$) and very slow motion $R \approx 10^4\ s^{-1}$. We superimpose the results for isotropic ($N = 1$) and very anisotropic ($N = 100$) motions to demonstrate that they are almost indistinguishable. However, in Fig. 6*b* and *c* we show the 2D ESE contours and 0 MHz slices for the same parameters. They clearly differ both in magnitude and shape and are very easily distinguishable!

We now address the question as to the relevance of ESEEM for 2D ESE experiments. We recall from Eq. 12 that these ESE experiments require a small

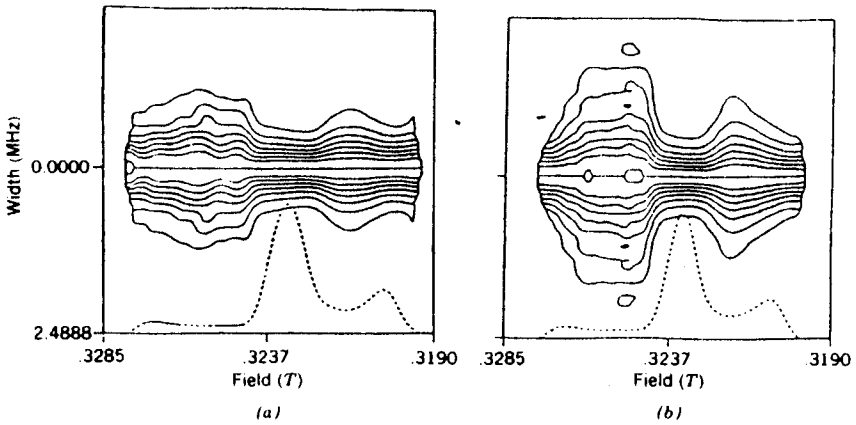

Fig. 5. Normalized contours and 0 MHz slices from spectra of two different nitroxides. (*a*) The spectrum of Tempone in 85% glycerol/H_2O at -75 °C. (*b*) The spectrum of CSL in *n*-butylbenzene at -135 °C. The T_M's for these spectra, under these conditions, are approximately the same.

B_1 such that $\gamma B_1 \ll \Delta$ the inhomogeneous width. However, it also requires that $B_1 \ll a_i/\gamma$, where a_i is the shf constant for the ith deuteron (or proton), in order that ESEEM *not* be excited. In actual fact, it is only practical to achieve this inequality for fully protonated samples, so only such samples were used. On the other hand, if $B_1 > a_1/\gamma$, then the 2D ESE experiments would include the effects of ESEEM, and, in fact, one could map out how the ESEEM varies across the ESR spectrum. This can be expected to enhance the interpretation of these patterns, both for structure and dynamics.

To proceed further with this 2D ESE technique, we wish to point out that an important experimental artifact has not been included in Eq. 11, namely, the effect of a nonzero deadtime τ_d after the second pulse. Millhauser and Freed [9] have shown that a modern technique of data analysis, namely, linear prediction with singular-value decomposition (LPSVD), enables one to back-extrapolate the 2D ESE data set to estimate the signal in the range $0 < \tau \leq \tau_d$. The LPSVD method also leads both to significantly improved resolution enhancement of the complex 2D line shapes as well as to the least-squares values characterizing the exponential decays consistent with Eqs. 10 and 11 [9]. Furthermore, it removes a difficulty with fast Fourier transform (FFT) methods. That is, to avoid so-called FFT window effects, it is necessary to collect data over a considerable time range, before performing an FFT. This means that a considerable amount of time is spent collecting data when the signal-to-noise ratio is low; hence, the spectral resolution is low. Instead, with LPSVD, one need collect data over only those time ranges for which there is a significant signal, thereby greatly increasing the efficiency of the data acquisition. These features are illustrated in Fig. 7. The LPSVD method is summarized in the appendix. Its

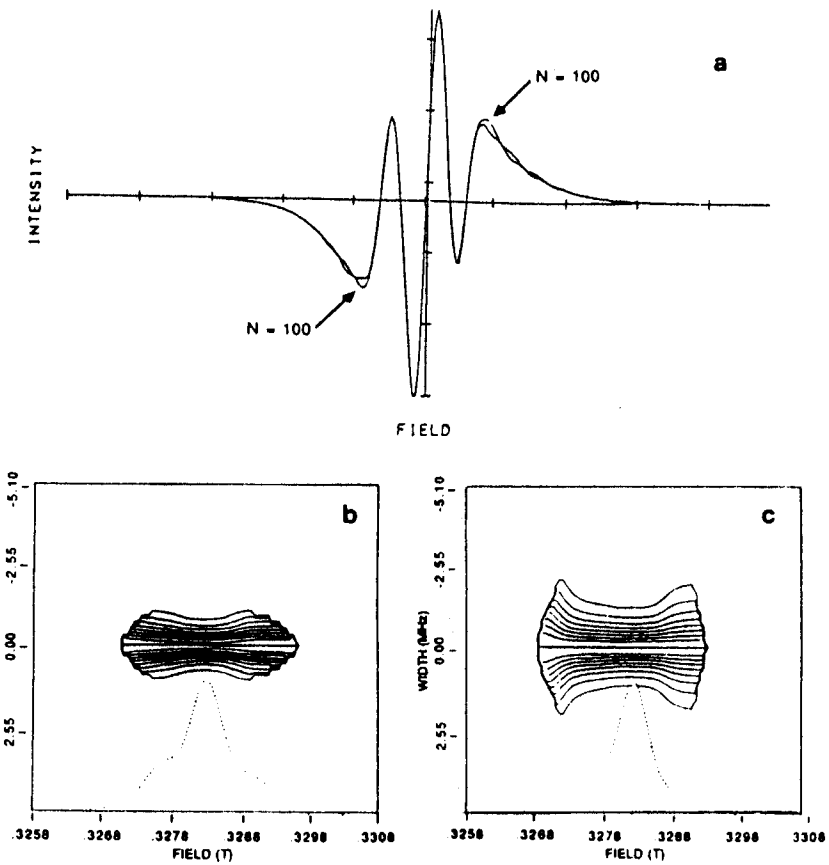

Fig. 6. A comparison of the relative sensitivity of cw vs. 2D ESE to motional anisotropy. (*a*) Two superimposed spectral simulations where one spectrum has $R_\perp = 10^{-4}\ s^{-1}$ and $N = 1$, and the other has the same $R_\perp$ but with $N = 100$. The markers on the x axis are 9.77×10^{-4} T apart. The normalized contours are simulated from the same parameters with (*b*) $N = 100$ and (*c*) $N = 1$. This is a case of high ordering, with order parameter $S = 0.87$ and $\theta = 0°$.

ability to recover signal from noise means that as long as one is able to obtain echoes yielding an estimate to T_M by usual procedures, then useful 2D ESE contours may be obtained with the use of LPSVD.

Given the good resolution of Fig. 7*c* it is appropriate to compare the results with theory. We show in Fig. 8 several simulations for this system based on Brownian motion, but for different amounts of rotational anisotropy. The best agreement is obtained for nearly isotropic motion.

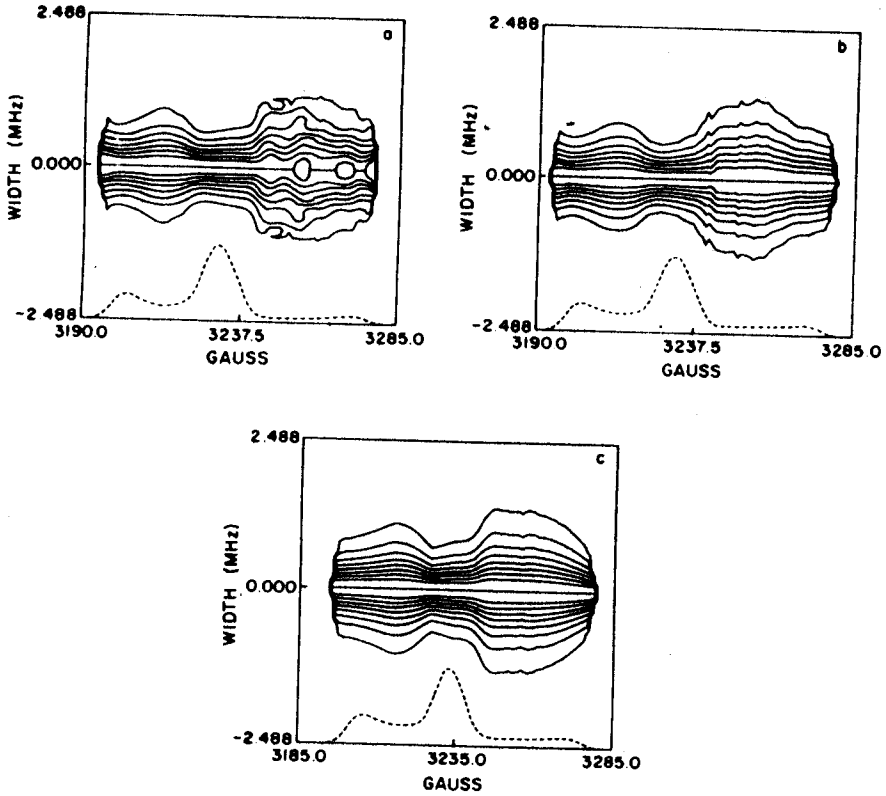

Fig. 7. Normalized contours showing the resolution enhancement obtained from the LPSVD treatment. (*a*) From data of Tempone in 85% glycerol/H_2O at -75 °C treated by conventional FFT. (*b*) From the same data set, but treated with LPSVD. (*c*) A different data set that was collected from the same system in a manner that maximizes the efficiency of the LPSVD algorithm. From Ref. 9.

Since this 2D ESE technique is very sensitive to slow motions, that is, $\tau_R < 10^{-3}$ s, it also has applications to the study of slow-motional reorientation of spin-labeled macromolecules such as proteins. 2D ESE spectra have now been obtained from spin-labeled (partially) immobilized proteins in two separate studies [27, 28]. They demonstrate the future importance of the 2D ESE method in such biologically relevant systems. The effects of the rotational motions are still visible in the 2D contours.

Finally, we note that saturation transfer [29] is a cw-ESR technique frequently used in a more qualitative fashion to study very slow motions. While relatively easy to perform, the analysis is quite complex. The analysis of 2D ESE, as discussed above, is more straightforward.

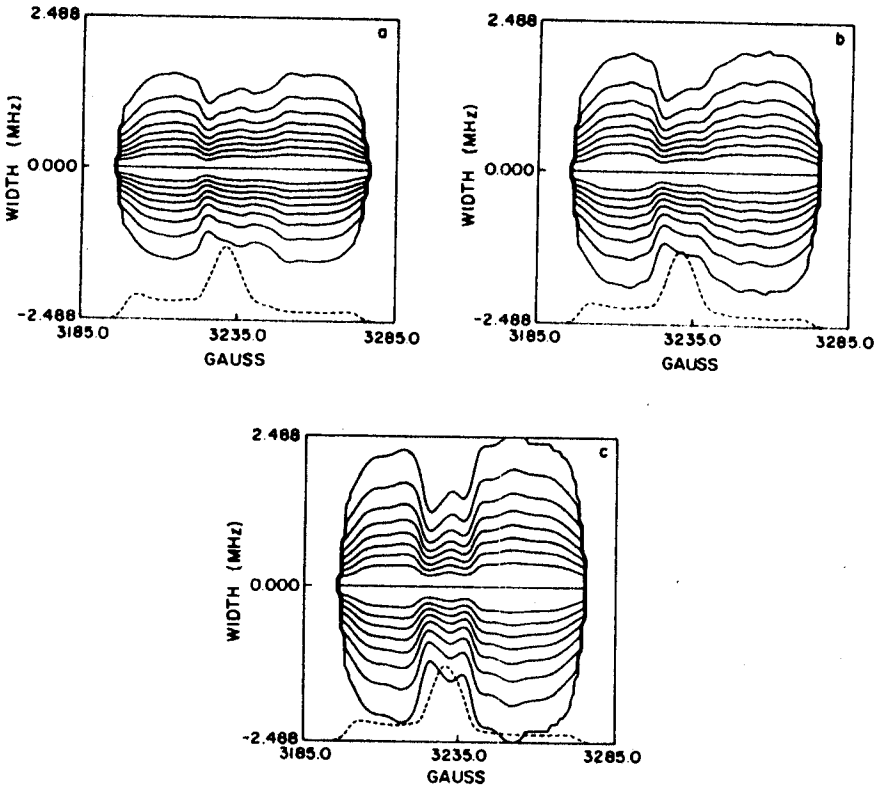

Fig. 8. Theoretical simulations of 2D ESE spectra for a model of Brownian motion for comparison with Fig. 7: (*a*) $N \equiv R_{\parallel}/R_{\perp} = 1$; (*b*) $N = 2$; (*c*) $N = 3$. $R_{\perp} = 6 \times 10^{3}\ s^{-1}$ in all cases, and $R_{\parallel}$ refers to rotation about the molecular y axis. The magnetic parameters utilized were $g_x = 2.0089$, $g_y = 2.0058$, $g_z = 2.002$ (except for (*a*) where $g_z = 2.0021$); $A_x = A_y = 5.27$ G, $A_z = 36.0$ G. The Lanczos convergence parameters [cf. G. Moro and J. H. Freed, *J. Chem. Phys.* **74**, 3757 (1981) and Ref. 15], were $L_{max} = 44$, $K_{max} = 2$, $n_1 = 300$. The inhomogeneous broadening is 3 G and $\tau_d = 0$. From Ref. 9.

4. 2D ESE STUDIES OF MAGNETIZATION-TRANSFER VARIATION ACROSS THE SPECTRUM

In the previous section we have demonstrated how, by the use of the standard two-pulse echo sequence, one could obtain a slow-motional 2D ESE spectrum, which is a plot of the spectrum as a function of both the natural line widths and the resonance positions of the DSPs. We now wish to describe an analogous experiment but in the context of T_1 measurements, which provides a "map" of the rates of *magnetization transfer* from each spectral region. However, we must

first provide the needed background on echo sequences designed to measure T_1's and more generally magnetization transfer. First, we review (Section 4.1) the standard T_1-type measurements, that is, the inversion recovery (IR) sequence π-T-$\pi/2$-τ-π-τ (cf. Fig. 1*c*) and the stimulated-echo (SE) sequence $\pi/2$-τ-$\pi/2$-T-$\pi/2$-τ (cf. Fig. 1*b*) [16, 20, 23, 30]. We also summarize their theoretical interpretation in terms of motional dynamics. We then describe (Section 4.2) the appropriate 2D techniques and provide an example.

4.1 Inversion Recovery and Stimulated-Echo Sequences: Full Irradiation

The IR sequence first inverts the z magnetization with a π pulse, and after a time T, the z magnetization is probed by a simple $\pi/2$–π echo sequence (cf. Fig. 1*c*). If the spectrum is fully irradiated by a *nonselective* pulse, then by stepping out T, one observes a simple exponential decay with decay constant T_1 equal to $(2W_e)^{-1}$, where W_e is the pure electron spin-flip rate, assumed for simplicity to be isotropic. This result is true both in the fast- and slow-motional regimes.

The SE sequence is more sophisticated (cf. Fig. 1*b*). The first pulse of this sequence (called the preparation pulse) nutates the dynamic spin packets first into the xy plane, where they precess at their individual Larmor frequencies for a time τ. During this evolution period the DSPs get out of phase, and the projection of each DSP onto the rotating y' axis at time τ, which will be nutated onto the z axis by the second pulse (taken as being about the x' axis), will depend upon its Larmor frequency. In this manner, the DSPs are *frequency-labeled* during this first τ interval. During the second (i.e., T) interval (referred to as the mixing period), electron spin flips will reduce the negative magnetization component M_z just as in the IR sequence, and this would be independent of the individual DSP labeling for an isotropic W_e. Unlike the situation in the IR sequence, motion and nuclear spin flips will also be effective during this mixing interval. This is because, as the molecules reorient or change their nuclear spin state, they change the DSPs to which they contribute. An echo will be formed at a time τ after the third (or detection) pulse only to the extent that the frequency labeling is still accurate at the end of the mixing interval. The more effective the motion and/or the nuclear spin flips at changing (during the mixing period) the DSPs to which a molecule contributes, the weaker will be the echo after the detection pulse.

At this point one might be concerned by the fact that DSPs are being *interconverted* by the molecular dynamics given that they are the normal modes. The answer to this matter lies in the fact that the DSPs as introduced above refer to normal-mode solutions for spin packets precessing in the rotating $x'y'$ plane; hence the designation of T_2-type behavior. When the spins are rotated to the (negative) z axis, then the effective stochastic Liouville operator (in particular the spin part) is different, so that the normal-mode solutions are different, *even though the molecular dynamics is unchanged.* These are the T_1-type normal modes [23, 30]. For example, for the case of a simple g-tensor spin Hamiltonian describing ultra-slow-motion near the rigid limit, the DSPs are to a first

approximation the rigid-limit spin packets (i.e., a continuum with each member representing a particular orientation), while the T_1-type normal modes are found to be the spherical harmonics (i.e., the eigenfunctions of the simple rotational diffusion operator that span the Hilbert space defined by the molecular orientations). This is why it is possible for the T_2-type DSPs to be interconverted during the period when T_1-type relaxation is occurring. The general theory [1, 23, 30, 31] allows one to consider the appropriate normal modes at each stage of the pulse sequence and their interconversion by each pulse.

The theoretical results therefore predict that the T_1-type relaxation in slow-motional magnetization-transfer (MT) experiments may be expressed as a weighted sum of exponential decays, whose time constants represent the T_1-type normal modes. Let us call them the MT modes. The weighting factors depend, in part, on τ, which measures how long the DSPs dephase by their precession in the xy plane after the first $\pi/2$ pulse.

As discussed above, the case of the IR sequence with full irradiation reduces to just a single exponential form:

$$s(T + 2\tau) = A[1 - 2\exp(-2W_e T)] \tag{14}$$

where $s(T + 2\tau)$, the signal at time $T + 2\tau$, is that of the echo maximum (cf. Fig. 1*c*). For SE with full irradiation, the result is written as

$$s(T + 2\tau) = \sum_p b_p(\tau)\exp(-\Lambda_{d,p} T) \tag{15}$$

where $\Lambda_{d,p}$ is the decay rate for the pth MT mode. While it would be difficult to detect many superimposed exponentials, we have found that in the limit of $W_e\tau_R \ll 1$ this expression is fit to a good approximation by a sum of only two exponential decays, that is, as

$$s(T + 2\tau) = A + B\exp(-2W_e T) + C\exp\left(-\frac{T}{T_A}\right) \tag{16}$$

where $T_A(\tau)$ is the MT time, which decreases with τ. One can show that at $\tau = 0$, $C = 0$, so there is only a single exponential decay in $2W_e$, since there is insufficient evolution time for the spins to precess appreciably in the xy plane, and the first two $\pi/2$ pulses thus add to a single π pulse. The more interesting limit is for $\tau > T_2^*$, the effective decay time of the free-induction decay (FID), (while also $\tau < T_2$), for which T_A approaches an asymptotic value such that $T_A < (2W_e)^{-1}$. Also B and C take on asymptotic values independent of τ that are in general of significant magnitude. In this limit the frequency labeling during the evolution period is complete, so that MT during the mixing period can have its maximum effectiveness. We find this asymptotic value to be $T_A \sim \tau_R/b$ where $b \approx 2.5$ for Brownian motion and $b \approx 1$ for jump motion

[23, 30]. In the limit $W_e\tau_R \gg 1$, the slow-motional MT is too weak, so the results are again simply described by Eq. 14.

4.2 2D ESE and Magnetization Transfer: Partial Irradiation

By analogy to the 2D technique providing T_2 variation across the spectrum, we can devise an experiment to provide the MT or T_A variation across the spectrum by employing partial irradiation. However, in the case of partial irradiation, *both* IR and SE sequences yield signals of the form of Eq. 15 which are well represented by Eq. 16 for all positions in the spectrum. There is now an extra MT mechanism, namely, MT shifts spins that are initially irradiated to frequencies outside the irradiated region. When this occurs, the spin is no longer detectable, and it is as though it has relaxed back to equilibrium. More precisely, spins rotated into the xy plane by the (frequency) selective preparation pulse will not even be affected by the second or mixing pulse and/or the detection pulse if they are transferred out of the irradiation "window." This mechanism is more important for IR than for SE, since in the latter case the basic spin-delabelling mechanism, described above, already supplies a closely related effect on T_A.

In summary, the relative effectiveness of MT out of the different spectral regions can be studied by such a partial irradiation technique, but first the two decays in $(2W_e)^{-1}$ and T_A^{-1} must be separated in the data processing. This is again accomplished by applying LPSVD.

We now consider mechanisms whereby T_A can vary across the spectrum. Suppose a molecule whose principal magnetic axis is parallel to the applied field ($\theta = 0°$) makes a small Brownian jump by $\Delta\theta$. Its new spectral frequency will hardly change, because the orientation-dependent part of the resonance frequency mainly goes as $3\cos^2\theta - 1$, which for $\theta = 0°$ or $90°$ gives a change of $\Delta\omega \propto (\Delta\theta)^2$. However, for a molecule oriented at $\theta \sim 45°$, that same Brownian jump will cause a corresponding spectral frequency change given by $\Delta\omega \propto \Delta\theta$. Thus, the spin packet at the $\theta = 45°$ orientation experiences the more effective MT out of an irradiated region. Similarly, if there is anisotropy of the diffusion tensor (e.g., if there is rapid rotation only about the molecular y axis), then DSPs associated with the perpendicular (i.e., x and z) orientations will experience more rapid MT than DSPs associated with the y orientation, thus yielding a greater T_A^{-1} for those DSPs associated with the perpendicular orientations.

The more general form of Eq. 15 for SE with partial irradiation is [1, 23, 30, 31]

$$s(T + 2\tau) = A' \exp(-2W_e T) \sum_p b_p^{\omega}(\tau) \exp\left(-\frac{T}{\tau_p}\right) \tag{17}$$

where

$$\tau_p^{-1} = \Lambda_{d,p}^{-1} - 2W_e \tag{18}$$

and

$$b_p^{\omega}(\tau) = \sum_{n',l',j'}^{\omega} \sum_{m,k,i} \sum_{s,q} O_{o,qn'} O_{o,mn'} O_{d,mp} O_{d,k,p} O_{o,kl'} [O_{o,il'} O_{o,ij'}^*] O_{o,sj'}^* \times \exp[-(\Lambda_{o,n'} + \Lambda_{o,j'}^*)\tau] \tag{19}$$

(For a nitroxide with three allowed transitions, s and q take on values -1, 0, and 1.) Here O_o is the orthogonal transformation introduced in the previous section, which diagonalizes the stochastic Liouville operator associated with the DSPs and O_d is the equivalent orthogonal transformation for the MT modes. The $\Lambda_{o,n'}$ are the eigenvalues of the DSPs while the $\Lambda_{d,r}$ are those for the MT modes. The primes appearing on the indices n', l', and j' imply that these are summed only over those DSPs that are within the irradiation window of the selective pulse, (i.e., they depend upon $\omega_j - \omega$). This gives an implicit dependence upon ω as indicated. We have actually used this form for the theoretical predictions given below [23, 30]. (In the near rigid limit, when Eq. 9 applies, we may let $\Sigma_i O_{o,il'} O_{o,ij'}^* \approx \delta_{l'j'}$ to achieve some simplification of Eq. 18.) Fortunately, the results are approximately fit by Eq. 16 at each position in the spectrum! Also, W_e is found to be constant, within experimental error, across the spectrum in the example below. (But we will encounter an expression like Eqs. 17–19 in Section 5.) Thus, after extracting the term in $\exp(-T/T_A)$ by LPSVD, and after FT, one obtains a plot of $T_A/(1 + \omega^2 T_A^2)$ across the spectrum with normalized contours showing the variation of T_A.

We illustrate this 2D MT experiment for the NO_2/vycor system in which the NO_2 is physisorbed on the vycor surface. We display in Fig. 9 the 2D normalized contours for T_A obtained at 35 K. Focusing on the $M_1 = 0$ region (the central region), we see that the broadening that corresponds to the x and z molecular axes being parallel to the field is quite dramatic. This is clear evidence for more rapid rotation about the y axis, which is the axis parallel to the line connecting the two oxygen atoms. The contours in the $M_1 = \pm 1$ regions indicate less clear trends, probably due to inhomogeneous broadening from site variation in the hf matrix.

This example indicates the potential utility of the 2D MT experiment, which can provide useful information about molecular dynamics even prior to a thorough quantitative spectral analysis. Furthermore, it appears that rotational motion is detectable at lower temperatures than with the T_2-type 2D ESE experiment described in Section 3. Theoretical predictions [23, 30], summarized in Fig. 10, show that this technique is very sensitive to the model of molecular reorientation. The relationship to the new 2D FT techniques will be discussed in Section 5.

4.3 Spin-Echo ELDOR

A spin-echo ELDOR technique has also been developed and has been applied to the study of slow motions [5]. While ELDOR has typically been applied in the

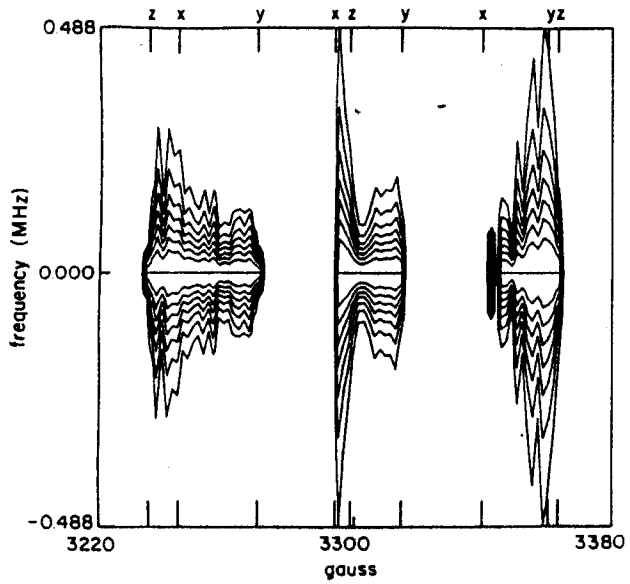

Fig. 9. Two-dimensional ESE contours from stimulated echo sequence for NO_2 on vycor at 35 K showing rates of magnetization transfer. It shows relatively rapid rotation about the molecular y axis (i.e., the axis parallel to oxygen–oxygen internuclear vector). From Ref. 30.

past as a cw technique [4], pulsed ELDOR is also possible [32]. The use of cw-ELDOR for the study of slow motions was suggested some time ago by Bruno and Freed [33], and detailed cw studies and analysis were performed by Hyde and Dalton [34]. The use of spin echoes in such studies was suggested previously [1]. The advantages of an echo technique for ELDOR are (1) the absence of the radiation fields (as well as any dc field modulation) during the evolution time of the spins and the (rotational) diffusion of the molecules, (2) the cancellation of effects of inhomogeneous broadening, and (3) the direct measurement of relaxation rates rather than just their ratios, such as obtained by cw-ELDOR. This latter advantage also exists for pulsed ELDOR based on saturation recovery techniques [35]. Thus, (1) permits a much simpler theoretical analysis (in terms of the stochastic Liouville equation), while (2) suggests greater accuracy in data analysis (without having to resort to deuteration of spin labels as we already noted) and (3) removes the need for additional techniques.

ELDOR may be regarded as the epitome of MT experiments by ESR. One first inverts the z magnetization of some spin packets, and at a later time, one "observes" whether this spin inversion has been transmitted to another part of the spectrum. Thus, whereas the previous MT methods merely observe the rate

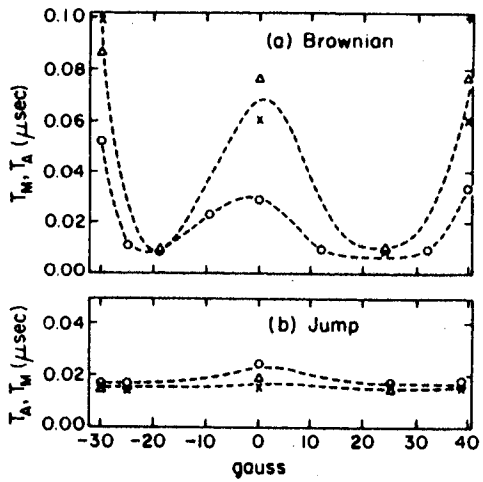

Fig. 10. Calculated time constants T_A and T_M versus dc field across the nitroxide spectrum for partial irradiation. The irradiation window is 4 G. ×, The T_A from the IR sequence; △, the T_A from the SE sequence; and ○, the T_M from a spin-echo sequence. (*a*) Brownian motion and $\tau_R = 170$ ns, $W_e = 0.05/\tau_R$. (*b*) Moderate jump model, $\tau_R = 17$ ns, $W_e = 0.05/\tau_R$. From Ref. 30.

of loss of magnetization from a given spectral region, ELDOR shows to which region(s) of the spectrum they are delivered.

The precise technique that was first used [5] is a stepped-field method in conjunction with a conventional three-pulse π–T–$\pi/2$–τ–π–τ sequence used to measure T_1's by IR (cf. Fig. 1*d*). We call this technique spin-echo ST-ELDOR. The first π pulse inverts the magnetization at one resonant field B_0 in the spectrum. Then B_0 is rapidly stepped by ΔB_0 to a new region of the spectrum, and the $\pi/2$–τ–π pulses are applied to yield the usual echo at time τ after the last π pulse. In this experiment T is varied, while τ is maintained at a fixed value. The echo amplitude, as a function of T gives the variation of the spin magnetization at the spectral region $B_0 + \Delta B_0$ due to the initial inversion of the spins at B_0. It is thus a direct measure of transfer of spin polarization. Similar experiments have also been performed by Tsvetkov and coworkers [6].

The characteristic feature of the results is the initial decrease in signal versus T to a minimum followed by a slower return to an equilibrium value (cf. Fig. 11*a*). The shape of $s(T)$ is consistent with a model in which a portion of the spins inverted in one region is transferred to another and then relaxes back to equilibrium. The transfer of spin polarization can be due to rotational reorientation, while W_e would then restore the spins to equilibrium.

A simplified analysis of this experiment, based on the model of strong jumps leads to the following discussion [5]. The orientation-dependent echo signal

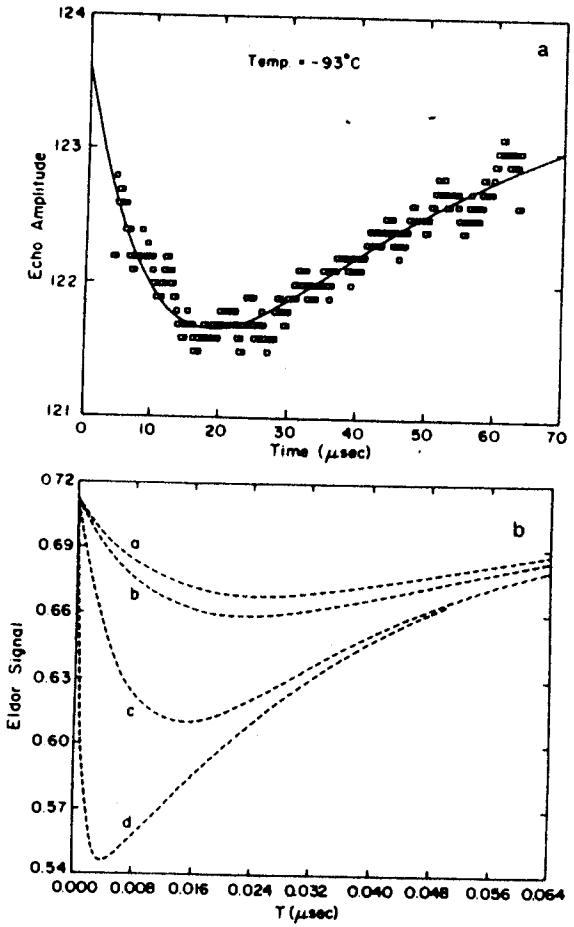

Fig. 11. (*a*) Experimental stepped-field ELDOR echo amplitude versus time between first π pulse and $\pi/2$ pulse for PD-Tempone in 85% glycerol/H_2O at -93 °C. Solid line: Best two-exponential fit to data. From Ref. 5. (*b*) Calculated ELDOR curves for slowly tumbling nitroxide. In sequence *a–d* orientation-independent nuclear spin-flip rate increased, thereby increasing the ELDOR effect. From Ref. 23.

$S(\Omega_i, T)$ at Euler angles specified by Ω_i due to initially irradiating the spectrum corresponding to Ω_j is given by

$$S(\Omega_i, T) \propto \frac{-1}{8\pi^2}\{e^{-T/T_1} + e^{-\omega' T}[8\pi^2\delta(\Omega_i - \Omega_j) - 1]\} \tag{20}$$

where $\omega' = T_1^{-1} + \tau_R^{-1}$, and $\delta(\Omega_i - \Omega_j)$ is the Dirac delta function. Here

$T_1 = 2W_e$, which is assumed to be largely independent of orientation. Thus, if $\Omega_i \neq \Omega_j$ one has

$$S(\Omega_i, t) \propto \frac{-1}{8\pi^2}(e^{-T/T_1} - e^{-\omega' T}) \qquad \Omega_i \neq \Omega_j \tag{21}$$

Equation 21 clearly shows that there will be a nonnegligible effect only if τ_R is not much longer than T_1. In actual fact, a range of Ω_j are affected by the first π pulse, while the detecting pulses "observe" a range of Ω_i. Thus, we may write

$$S(\Omega_i, T, \tau) = S_0(\Omega_i, \tau)[1 - C(\Omega_i, \Omega_j)(e^{-T/T_1} - e^{-\omega' T})] \qquad \Omega_i \neq \Omega_j \tag{22}$$

where $S_0(\Omega_i, \tau)$ measures the echo signal from a conventional $\pi/2\ \tau_2\ \pi\ \tau_2$ sequence that arises from the dynamic spin packets in the appropriate range of orientations centered about Ω_i. Also, $C(\Omega_i, \Omega_j)$ is a factor determined by the range of orientations centered about Ω_i, whose spins are initially inverted, and the range about Ω_j, whose spins are "observed". It is both an instrumental factor via B_1 and a function of the spectral line shape. This factor can be removed from the analysis by solving for T_{min} such that $S(\Omega_i, T, \tau)$ is a minimum. One easily obtains

$$\ln\left(1 + \frac{T_1}{\tau_R}\right) = \frac{T_{min}}{\tau_R} \tag{23}$$

However, the *integrating effect* over a range of orientations still remains in the technique. (2D FT-ELDOR described in Section 5 would *not* suffer from such integrating effects and would permit $\Omega_i - \Omega_j$ to be arbitrarily small.)

An extensive theoretical analysis of ELDOR spin echoes based upon the stochastic Liouville equation has been developed [23]. This analysis confirms the semiquantitative validity of the simple analysis for jump diffusion, but it also rigorously extends the theory to all types of motions. The general results can again be approximated by Eq. 22 with specific values of S_0 and C given as a function of the resonant frequencies initially inverted and then observed. Also, the precise definitions of T_1 and ω' are modified somewhat. However, a mechanism of orientation-independent nuclear spin flips was found to be potentially important in generating ELDOR effects (cf. Fig. 11*b*).

While there have been recent improvements in this technique, we defer discussion, especially since the 2D FT methods in Section 5 are potentially the more powerful.

5. TWO-DIMENSIONAL FOURIER TRANSFORM ESR

5.1 Introduction and Motivation

Jeener [36] first proposed the idea of two-dimensional correlation spectroscopy (2D COSY). In 2D COSY NMR the time-correlation function of the magnetization is obtained by utilizing two or more closely spaced rf pulses.

Ernst and coworkers [37] first demonstrated this concept utilizing two $\pi/2$ pulses in the basic 2D COSY NMR experiment. Since that original experiment, 2D NMR techniques have flourished [38]. However, that potential had not been realized experimentally in ESR, because of the requirement that the entire spin Hamiltonian be "rotated" by the radiation field, an experiment substantially more difficult in ESR than in NMR.

In terms of Fourier spectroscopy, other distinctions between electron spins and nuclear spins are that the electron spins typically resonate at much higher (i.e., microwave) frequencies with much greater spectral widths, and they exhibit much shorter relaxation times. These properties have imposed certain limitations on the application of Fourier spectroscopic techniques to ESR. The generation of extremely narrow (5 to 10-ns) microwave pulses necessary for Fourier transform ESR has only recently become practical. Digitizers with adequate sampling capability to record free induction decay signals of electron spins have also not been available until very recently. Now that such components are commercially available, the same techniques that were introduced to NMR beginning in the late 1960s are now being introduced to ESR. Simultaneously, Bowman and coworkers performed FT-ESR experiments of short-lived organic free radicals of spectral bandwidth ~ 40 MHz [39, 40] (cf. Chapter 1), and Gorcester and Freed performed FT-ESR experiments on the broader (~ 90 MHz) spectra of nitroxide radicals [41] based on earlier considerations of Hornak and Freed [42]. In a communication that followed shortly thereafter, Gorcester and Freed [7] first demonstrated 2D SECSY and 2D FT exchange ESR experiments on the same nitroxide radical samples. Since these initial demonstrations, there have been significant developments and improvements of 2D FT-ESR instrumentation and methodology [8, 43].

The principal application of 2D FT-ESR demonstrated thus far is to the ELDOR experiment. As we discussed in Section 4.3, ELDOR requires the use of two excitation fields: one to modify the populations (the pumping field at frequency ω_p) and another to detect the response (the observing field at frequency ω_o) elsewhere in the spectrum. In the slow-passage ELDOR experiment, one typically keeps the two constants at a precise frequency difference, while sweeping the dc magnetic field B_0 through the entire spectrum. One could repeat this experiment in which the difference between pumping and observing frequencies is varied and thereby obtain a two-dimensional spectrum with $\gamma_e B_0$ on one axis and $\omega_o - \omega_p$ on the other. Such a data set can be manipulated to produce the two-dimensional spectrum as a function of $\omega_o - \gamma_e B_0$ and of $\omega_p - \gamma_e B_0$, which are the *natural variables* for interpreting the spectrum. Alternatively, such a procedure can be applied in the time domain by utilizing the ST-ELDOR echo method discussed above. Such experiments would be very time-consuming and are typically not practical. However, such an experiment may be performed very efficiently with 2D FT-ESR methodology. With 2D FT-ELDOR [8], one obtains all of the combinations of pump and probe frequencies simultaneously in a single two-dimensional experiment! In fact, the matrix of 2D ELDOR peak intensities is rather simply related to the matrix of transitions

probabilities. Such an experiment can typically be performed in less than an hour and analyzed in a few minutes.

The analysis of 2D experiments, whether NMR or ESR, typically involves 2D Fourier transformation of a two-dimensional time series, followed by phase corrections and numerical determination of volume integrals. LPSVD presents an alternative to Fourier analysis [44, 45], and we do find that LPSVD may be very usefully applied to 2D FT-ESR [10]. Also, we have found a variation of this technique that is customized to exploit many of the symmetries in 2D FT-ESR or -NMR [10]. This is discussed in the appendix.

We now consider how the newly developed FT-ESR methods can improve and extend the range of 2D experiments on molecular dynamics. To date, this has been done for cases involving fast-motional nitroxide ESR spectra, but the principles and methods can be extended to slow motions.

5.2 Spin-Echo Correlated Spectroscopy (SECSY)

The 2D FT analog of the field-swept T_2-type 2D ESE experiment may be referred to as spin-echo correlation spectroscopy [7, 43] (SECSY). The basic pulse scheme for SECSY is illustrated in Fig. 12. The SECSY experiment involves acquisition of the electron spin echo during the t_2 time period for a series of equally spaced values of t_1. The 2D SECSY spectrum (Fig. 13) is obtained after making a small first-order phase correction in ω_2 and a linear amplitude correction. One observes the inhomogeneously broadened three-line hf pattern along ω_2 and the Lorentzian homogeneous line shapes along ω_1. (The dc magnetic field homogeneity was destroyed to suppress the FID from the second $\pi/2$ pulse. This would not be necessary for a slow-motional spectrum [3, 26, 30].)

The advantage of SECSY in comparison to field-swept 2D ESE is the order-of-magnitude shorter data acquisition time. In addition, SECSY has the

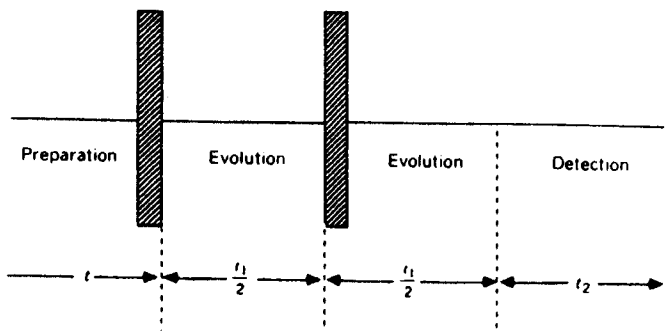

Fig. 12. SECSY pulse sequence. The homogeneous decay of the spin-echo occurs during the evolution period t_1; the inhomogeneous decay occurs in the detection period t_2.

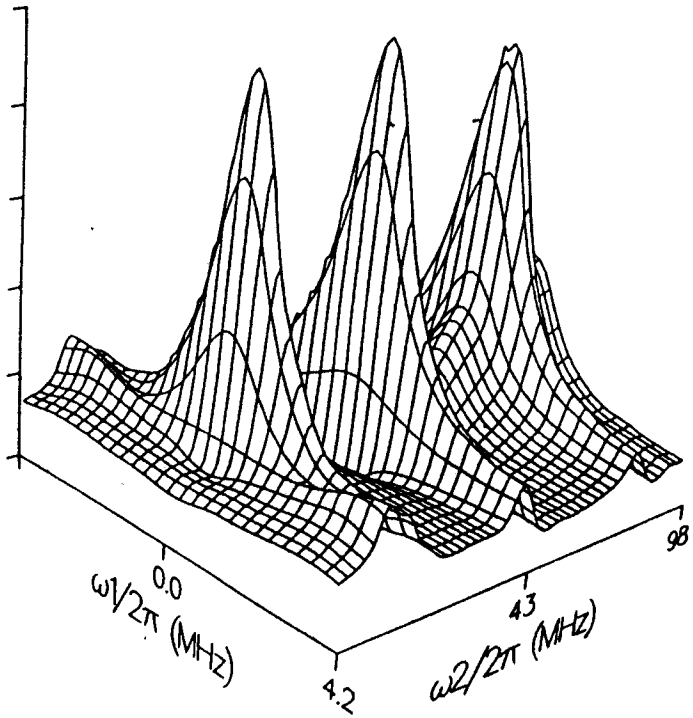

Fig. 13. SECSY spectrum of 1.17×10^{-3} M PD-Tempone in toluene-d_8 at 22 °C. $T_2^* \simeq 75$ ns; $T_2 \simeq 174$ ns; 0.86-ns resolution in t_2 providing 256 complex data points, each the average of 2048 transients. Time resolution in t_1 is 12 ns; pulse width is 15 ns; acquisition time is 60 min. From Ref. 7.

potential for observing (weak) cross-correlations that cannot be observed with techniques using narrow-band excitation.

The theory for this experiment [8, 43] is very similar to that of field-swept 2D ESE (cf. Section 3). One obtains

$$s'(t_1,t_2) = \sum_{k,m} c_{km} \exp(-\Lambda_k t_2) \operatorname{Re} \sum_j b_{mj} \exp \frac{(\Lambda_k - \Lambda_j^*) t_1}{2} \tag{24}$$

for the pulse sequence in Fig. 12, where

$$c_{km} = \sum_n U_n O_{o,nk} V_m O_{o,mk} \tag{25}$$

and

$$b_{mj} = \sum_l O^*_{o,mj} V_j^* O^*_{o,lj} U_l \tag{26}$$

We have neglected electron spin-echo envelope modulation (ESEEM) arising from cross-polarization of nuclei via the hf tensors. These terms are important in the slow-motional regime, as we have noted earlier.

The V_j give the correction for variation of effective B_1 across the spectrum for the $\pi/2$ pulse; that is, the jth DSP resonating at angular frequency ω_j experiences an effective rotation that depends on $\omega_j - \omega$ (with ω the irradiating frequency) and on B_1 [8, 42 46]. In comparing Eq. 24 with Eq. 6, we note that the a_{kj} of Eq. 6 is now replaced by $\Sigma_m c_{km} b_{mj}$. Also U is the vector of (appropriately averaged) spin transition moments.

After Fourier transformation with respect to t_1 and t_2 we obtain

$$S'(\omega_1,\omega_2) = \sum_{k,m} c_{km} \frac{1}{i\omega_2 - \Lambda_k} \operatorname{Re} \sum_j b_{mj} \frac{1}{i\omega_1 - \frac{1}{2}(\Lambda_k + \Lambda_j^*)} \tag{27}$$

Thus, inhomogeneous broadening is removed along the ω_1 axis.

A comparison of Eq. 27 with Eq. 11 shows that this full FT method provides both the in-phase and quadrature components with respect to ω_2. They are obtained from the two arms of the quadrature detector. It is also possible to obtain the out-of-phase part of the signal with respect to ω_1. First, let us refer to the pulse sequence yielding Eq. 27 as $(\pi/2)_x$–$(\pi/2)_x$, where the subscript x implies rotation of the spins by the microwave radiation along the rotating x axis. Then the out-of-phase part of the signal with respect to ω_1 is obtained by phase shifting the first $\omega/2$ pulse by 90°, which we then write as a $(\pi/2)_y$ $(\pi/2)_x$ sequence. It yields $S''(\omega_1,\omega_2)$, which is given by Eq. 27 but with the real part of the expression to the right of Re replaced by its imaginary part. We will refer to this approach as the 2D phase quadrature scheme.

5.3 Correlation Spectroscopy (COSY)

SECSY is based on detection of the echo signal. We now turn to FT-ESR experiments which are based upon detection of the free-induction decay (FID).

Two-dimensional correlation spectroscopy (2D COSY) in its various forms has gained widespread use in NMR as a method of observing coherence transfer between coupled spin transitions. The pulse sequence $\pi/2$ t_1 $\pi/2$ t_2 constitutes the simplest of the COSY experiments and is used in NMR in the separation of scalar interactions [37, 38]. A COSY-ESR spectrum is obtained in much the same manner as for NMR; the basic pulse scheme is illustrated in Fig. 14. The preparation period consists of a $\pi/2$ pulse to generate the initial transverse magnetization components. Free precession of the magnetization occurs during the evolution period of duration t_1 during which the components become amplitude encoded according to their precessional frequencies in the rotating frame. The FID is recorded during the detection period of duration t_2, which begins with the final $\pi/2$ pulse. For each t_1 the FID is collected, then the phase of the first pulse is advanced by 90°, and a second FID is collected. These two signals depend on terms oscillatory in t_1 that are in phase quadrature, that is, the

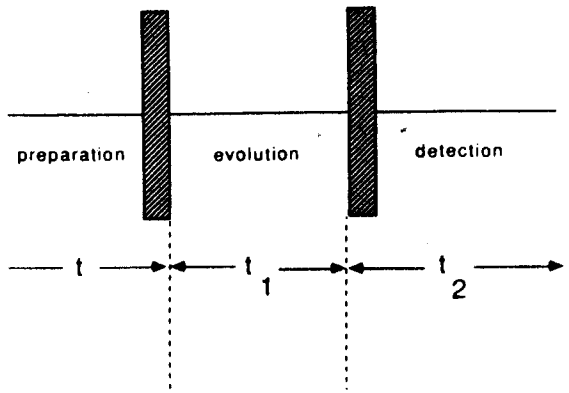

Fig. 14. 2D COSY pulse sequence.

2D phase quadrature scheme. The oscillatory behavior in t_1 is illustrated in Fig. 15 after Fourier transforming one of these signals with respect to t_2 only. Two-dimensional complex Fourier transformation generates a spectrum over the two frequency variables, ω_1 and ω_2.

This two-step phase-alternation sequence yields the required frequency discrimination in ω_1, and it provides the phase information necessary for the pure absorption representation of the 2D spectrum [47]. To cancel "images" resulting from imperfections in the quadrature detector, (cf. Section 6), we combine this two-step procedure with the four-step CYCLOPS image cancellation method [48] to obtain a sequence consisting of eight steps shown in Table 1 [8, 43]. A COSY-ESR spectrum of 5×10^{-4} M PD-Tempone in toluene-d_8 obtained in this manner is shown in Fig. 16. Resonances at positions for which $\omega_1 = \omega_2$ will be referred to in the standard fashion as autopeaks, because they represent autocorrelations. Cross-peaks representing cross-correlations are not found in the spectrum of Fig. 16 because the contributions of the electron electron dipolar and chemical or Heisenberg exchange interactions are too weak. Such mechanisms can induce *off-diagonal* relaxation between the different transitions [4, 49]. Additional peaks at positions for which $\omega_1 = 0$ arise because of electron spin flips during the evolution period; these peaks are referred to in the standard manner as axial peaks [37, 38].

5.4 2D ELDOR

We now describe the 2D FT experiment that displays the effects of MT. More precisely, it is a way of performing ELDOR but with only a single frequency source! The spectral band produced by a finite pulse is coherently related, and this is the basis for the power of the technique. 2D ELDOR involves a procedure similar to that of simple COSY except that three $\pi/2$ pulses are applied in the

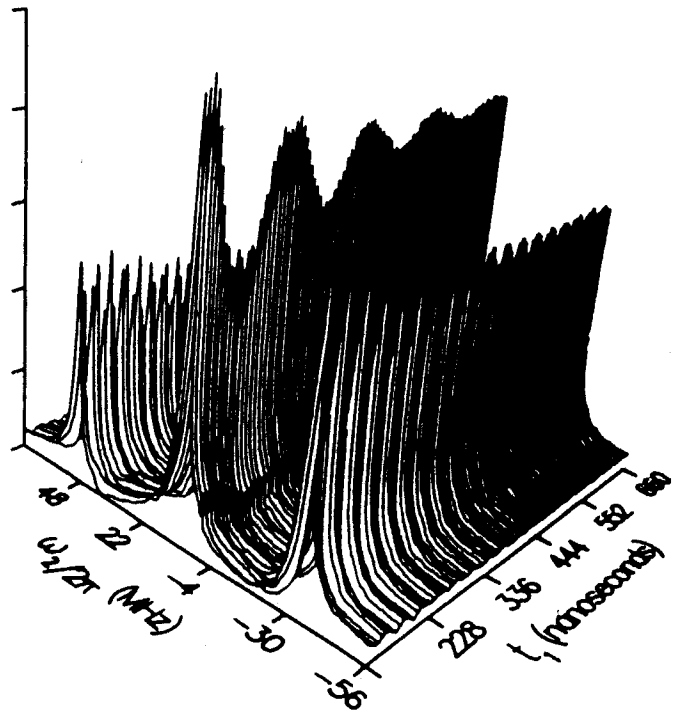

Fig. 15. 2D COSY-ESR spectrum of 5.1×10^{-4} M PD-Tempone in toluene-d_8 prior to FT in the t_1 domain showing the oscillatory behavior in t_1 (cf. Fig. 16 for a fully transformed 2D spectrum).

TABLE 1. Phase-Alternation Sequence for 2D COSY-ESR [from Ref. 7]

	Phase[a]		Memory Address[b]			
Step	ϕ_1	ϕ_2	1	2	3	4
1	x	x	+1	+2		
2	y	y	−2	+1		
3	$-x$	$-x$	−1	−2		
4	$-y$	$-y$	+2	−1		
5	y	x			+1	+2
6	$-x$	y			−2	+1
7	$-y$	$-x$			−1	−2
8	x	$-y$			+2	−1

[a] The phase of each mw pulse in the 2-pulse sequence.
[b] There are four distinct arrays into which data from the two digitizer channels (labeled 1 or 2) are either added (+) or subtracted (−).

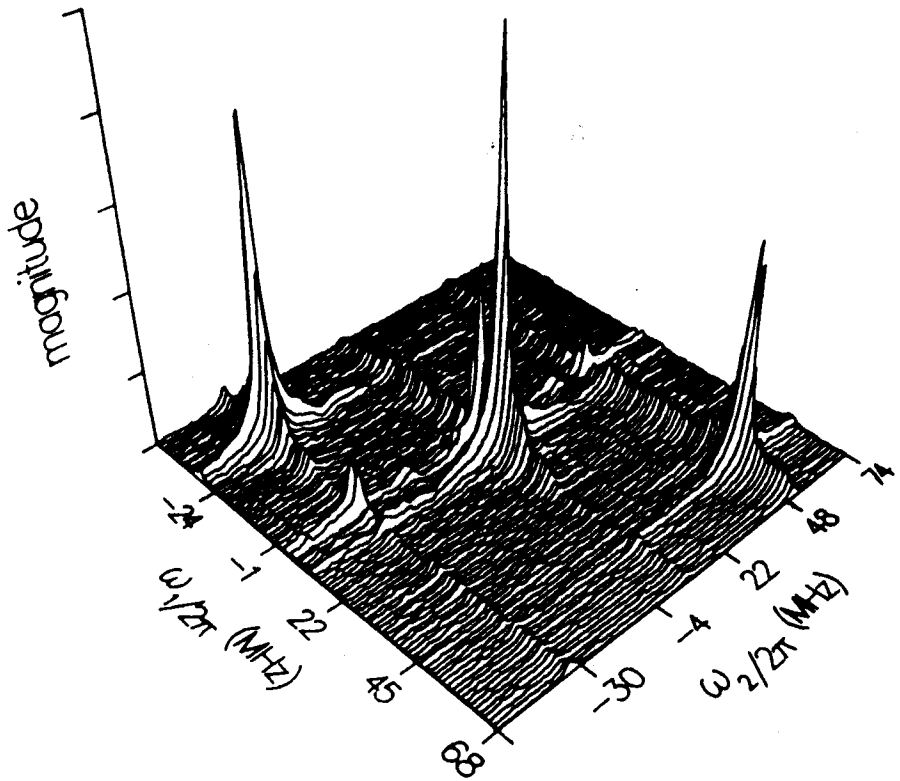

Fig. 16. Absolute value 2D COSY-ESR spectrum of 5.1×10^{-4} M PD-Tempone in toluene-d_8 at 21 °C; $\tau_p = 15.5$ ns; $\Delta t_1 = 3.9$ ns; 90 samplings in t_1; eight-step phase-alternation sequence with 30 averaged FID per step; deadtime in t_2, 100 ns; deadtime in t_1, 120 ns; acquisition time, 10.6 min. From Ref. 8.

sequence $\pi/2\text{-}t_1\text{-}\pi/2\text{-}T\text{-}\pi/2\text{-}t_2$ with the mixing time T being held constant. The application of this sequence (in NMR) to the study of chemically exchanging species was first illustrated by Jeener et al. [50]. The basic pulse scheme for 2D ELDOR is illustrated in Fig. 17. The preparation period consists of a $\pi/2$ pulse to generate the initial transverse magnetization. The phase of this pulse determines the phase of the amplitude modulation that results from the *frequency labeling* during the subsequent evolution period of duration t_1 as described above for the COSY-ESR experiment. The second $\pi/2$ pulse marks the beginning of the mixing period wherein the longitudinal magnetization components associated with each hf line can be exchanged, thereby mixing components carrying different precessional-frequency information (i.e., MT occurs). Thus, after rotating this magnetization into the xy plane for detection by the third $\pi/2$ pulse, components initially precessing with angular frequency

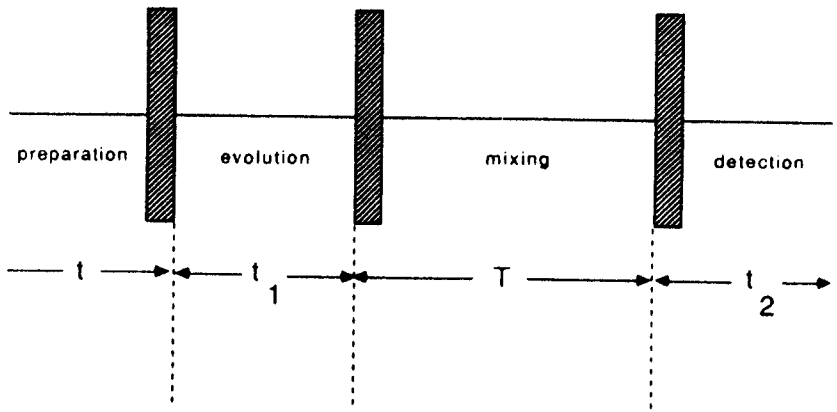

Fig. 17. 2D ELDOR pulse sequence, involving four time periods: preparation, evolution, mixing, and detection. After the preparation period, a $\pi/2$ pulse generates the initial transverse magnetization. Frequency labeling occurs during the evolution period t_1. The second $\pi/2$ pulse starts the mixing period, wherein the longitudinal magnetization components associated with each hf line can be exchanged with components having different precessional frequencies. When the magnetization is rotated into the xy plane for detection, components initially precessing with angular frequency $\omega_1 = \omega_a$ will, to the extent that magnetization transfer has occurred during mixing, precess with new angular frequency $\omega_2 = \omega_b$.

$\omega_1 = \omega_a$ will (to the extent that MT occurred by exchange during the mixing period) precess with new frequency $\omega_2 = \omega_b$. As in the COSY-ESR experiment, the pulse sequence is repeated for a series of equally spaced values of t_1, where for each t_1 the FID is collected and then the phase of the preparation pulse is advanced by 90°, followed by collection of a second FID.

A 2D ELDOR spectrum of 1×10^{-3} M PD-Tempone in toluene-d_8 [8] is shown in Fig. 18 with the corresponding contour map in Fig. 19. Magnetization transfer induced by Heisenberg spin exchange (HE) during the mixing period gives rise to cross-correlations and hence to the appearance of cross-peaks [7, 8, 43]. The cross-peaks in Fig. 18 have the characteristics predicted for an exchange process; that is, there are comparable cross-peaks between all pairs of auto-peaks. This arises because HE has no nuclear spin selection rules. Measurement of the relative intensities of auto-peaks and cross-peaks gives a direct determination of the Heisenberg exchange rate ω_{HE} (cf. Section 5.5).

Quantitative determination of exchange rates with 2D ELDOR is complicated by the presence of unwanted coherences which add intensity only to the auto-peaks of a motionally narrowed 2D spectrum, and in the slow-tumbling regime to the cross-peaks as well. This phenomenon, known as transverse interference [51], arises from transverse magnetization following the first $\pi/2$ pulse which freely precesses for the rest of the sequence and interferes

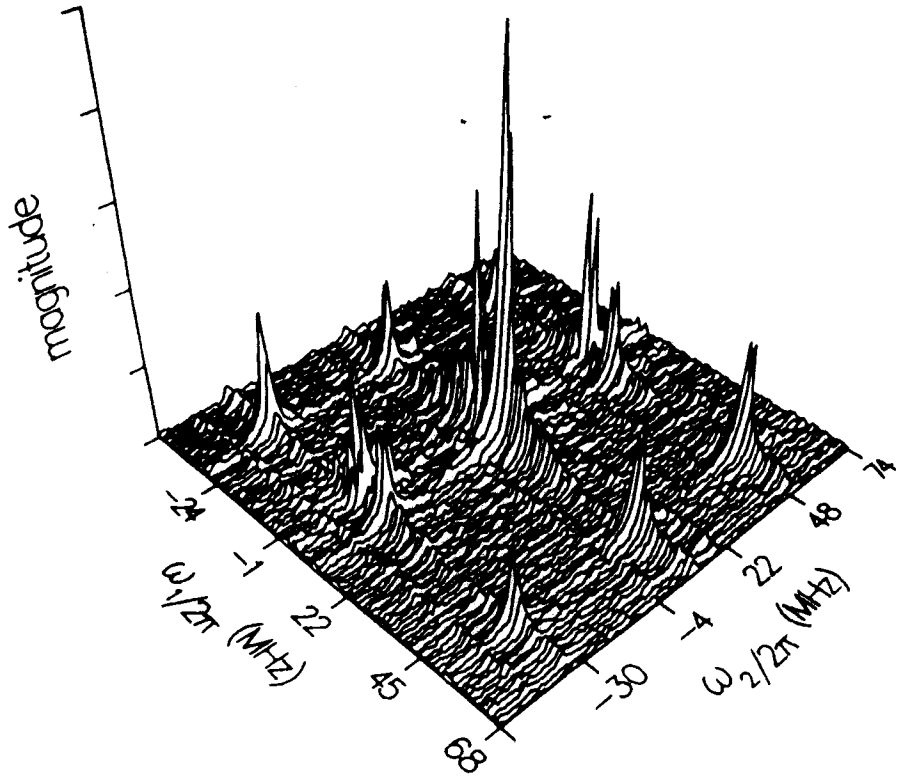

Fig. 18. Absolute value 2D ELDOR spectrum of 1.17×10^{-3} M PD-Tempone in toluene-d_8 at 21°C; $\tau_p = 15.2$ ns; $\Delta t_1 = 6$ ns; $\Delta t_2 = 3.9$ ns; 90 steps in t_1; 16-step phase-alternation sequence with 30 averaged FID per step; deadtime in t_2, 100 ns; deadtime in t_1, 120 ns; mixing time, $T = 3.10 \times 10^{-7}$ s; 256 complex data points per FID extending to 1 μs; acquisition time, 27 min. From Ref. 8.

with the FID recorded during the detection period. A two-step phase-alternation sequence has previously been suggested for the cancellation of transverse interference [51]. We can combine this sequence with our eight-step 2D image cancellation sequence to obtain a 16-step procedure tabulated elsewhere [8]. However, we have discovered a more compact phase-alternation sequence for 2D ELDOR which achieves the same result as the 16-step sequence but requires only eight steps. It is given in Table 2.

The 2D ELDOR spectra of 1×10^{-3} M PD-Tempone in toluene-d_8 were obtained with the 16-step phase-alternation sequence for four different mixing times. The ω_{HE} were determined by comparison of auto-peak and cross-peak magnitudes (e.g., volume) in each of these spectra according to the theory summarized below. These results could be compared to an ESE study in which

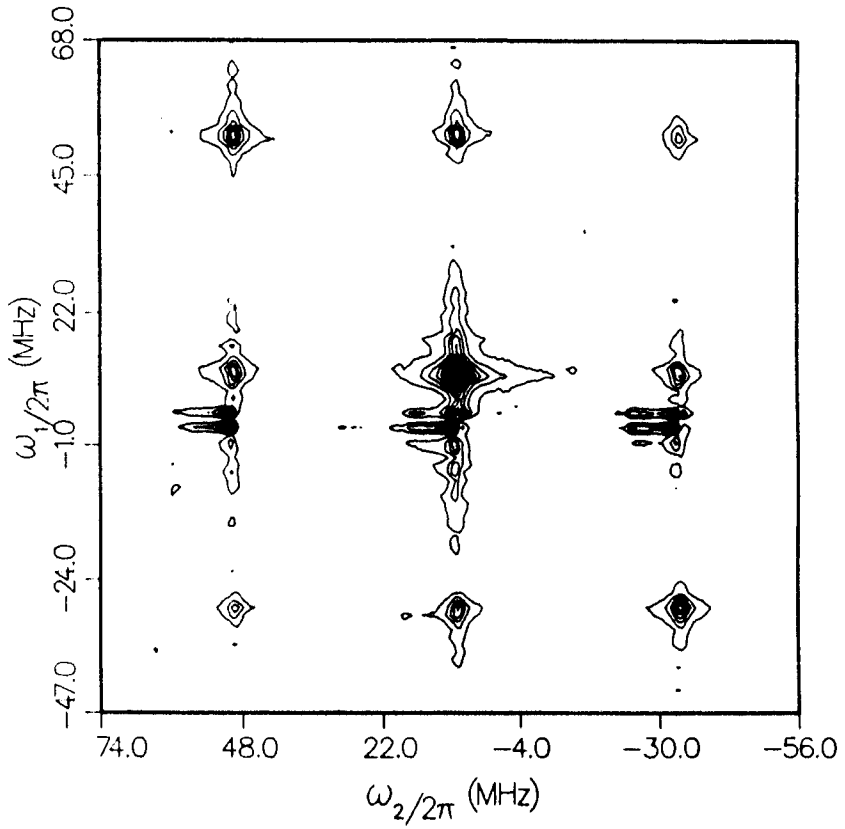

Fig. 19. 2D ELDOR contour map of spectrum of Fig. 18. Residual axial peaks appear as doublets centered on the line ω_1; the observed splitting is an artifact of the baseplane correction described in the text. From Ref. 8.

six different concentrations of PD-Tempone in toluene-d_8 were used, and T_2 ($M_1 = 0$) was determined for each by fitting the ESE envelope to a single exponential [8]. The exchange rate determined by ESE corresponds to the rate constant $\omega_{HE}/C \equiv k_{HE} = 3.63 \pm 0.63 \times 10^9\ M^{-1}\ s^{-1}$. The result is in agreement, within the experimental uncertainty, with the value determined by 2D ELDOR (cf. Fig. 28), corresponding to $k_{HE} = 3.97 \pm 0.43 \times 10^9\ M^{-1}\ s^{-1}$. This provided an important confirmation of the quantitative accuracy of the 2D ELDOR method.

The 2D ELDOR technique constitutes a direct observation of Heisenberg exchange on a single sample, whereas the ESE technique is somewhat indirect; that is, one usually fits T_2^{-1} to a linear dependence on concentration, but this is not always valid [52–54]. Electron–electron dipolar (EED) relaxation between probe molecules can also contribute to the observed T_2 in a concentration-dependent fashion. EED is "ELDOR active" [4] but its presence is reflected

TABLE 2. Eight-Step Phase-Alternation Sequence for 2D ELDOR [from Ref. 7]

	Phase[a]			Memory Address[b]			
Step	ϕ_1	ϕ_2	ϕ_3	1	2	3	4
1	x	x	x	+1	+2		
2	y	y	y	−2	+1		
3	x	x	$-x$	−1	−2		
4	y	y	$-y$	+2	−1		
5	y	x	x			+1	+2
6	$-x$	y	y			−2	+1
7	y	x	$-x$			−1	−2
8	$-x$	y	$-y$			+2	−1

[a] The phase of each mw pulse in the 3-pulse sequence.

[b] There are four distinct arrays into which data from the two digitizer channels (labeled 1 or 2) are either added (+) or subtracted (−). Note that $s'_{\mathrm{ELDOR}}(T, t_1, t_2)$ given by Eq. 35 is contained in memory addresses 1 (Re s'_{ELDOR}) and 2 (Im s'_{ELDOR}); $S''_{\mathrm{ELDOR}}(T, t_1, t_2)$ given by Eq. 36 is contained in addresses 3 (Re s''_{ELDOR}) and 4 (Im s''_{ELDOR}).

relatively more substantially in the T_2^{-1}, hence, also in the widths with respect to ω_1 and ω_2 of the 2D ELDOR resonance lines. This allows for discrimination between HE and EED in the 2D ELDOR experiment (EED was not important in this experiment in a nonviscous solvent [52, 55]). Also, we note that in an ELDOR experiment the sensitivity to ω_{HE} depends upon the ratio ω_{HE}/W_e (where W_e is again the electron spin-flip rate), whereas in a T_2 experiment it depends upon $\omega_{\mathrm{HE}} T_2(0)$ (where $T_2(0)$ is the concentration-independent T_2), so that when $W_e \ll T_2(0)^{-1}$, as is frequently the case, the ELDOR experiment would be the more sensitive to ω_{HE}. In this connection, one should note that whereas cw ELDOR yields only ratios, such as ω_{HE}/W_e, time-domain ELDOR, such as 2D ELDOR, yields the relaxation rates directly [1, 7, 8, 31, 56].

It is possible to use LPSVD methods to facilitate accurate projection of 2D absorption line shapes and to suppress certain artifacts that appear in 2D ELDOR spectra. For this purpose (as noted above) we have developed a new linear predictive technique, based on LPSVD [10], which models two-dimensional time series obtained in COSY-type experiments entirely in the time domain, that is without Fourier transformation. This new application of complex valued linear prediction facilitates the projection of 2D absorption line shapes as well as the rejection of residual axial peaks and much of the noise. We applied 2D linear prediction to the data set leading to Fig. 18. Projection of pure absorption line shapes was performed in both time domains (cf. Appendix). Extrapolation in t_1 eliminated artifacts caused by t_1 truncation and enabled a more accurate determination of baseplane offset. In Fig. 20 we illustrate the LPSVD result obtained after eliminating components for which $|\omega_1/2\pi| < 3$ MHz (i.e., narrow reject filtering of axial peaks); note the

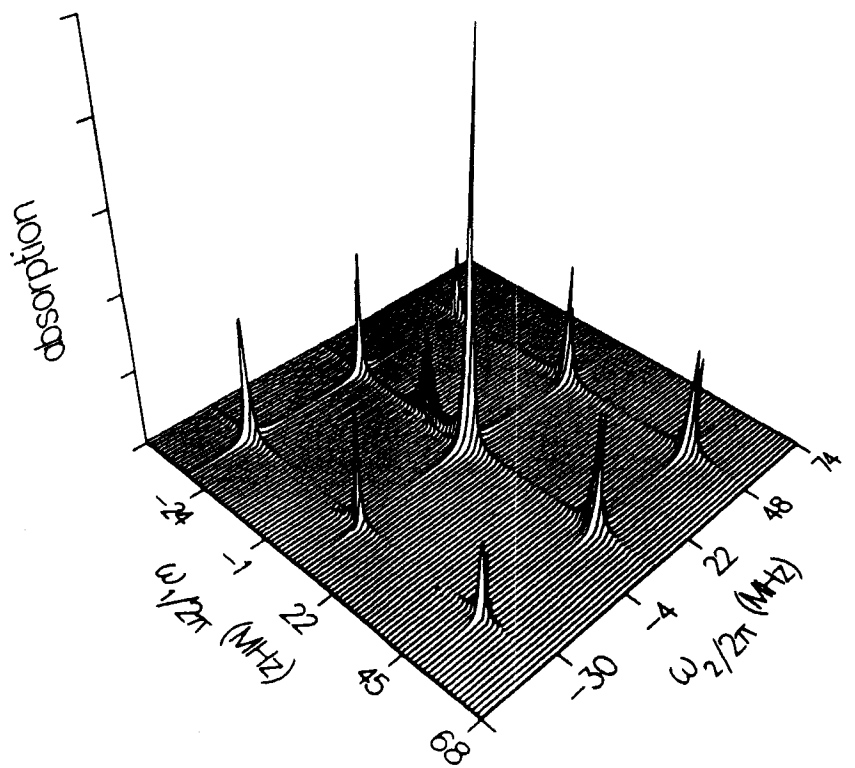

Fig. 20. LPSVD projected pure 2D absorption representation of the spectrum of Fig. 18. $M = 24$, $K = 6$ in the t_1 domain; $M = 60$, $K = 12$ in the t_2 domain; where M is the number of linear prediction coefficients and K is twice the number of signal peaks (cf. Section A.2). The broad peak near the center of the spectrum (at $\omega_1/2\pi = -8$ MHz) has zero width in ω_2 (hence, zero volume) and is apparently an artifact of the computation. From Ref. 10.

considerable improvement in signal/noise ratio. The volume integral of each 2D absorption line was measured by numerically integrating in the ω_2 domain and summing the results over the discrete values of ω_1. Estimation of the Heisenberg exchange rate from ratios of volume integrals with the use of Eq. 51 (cf. Section 5.5) gives the result $k_{\mathrm{HE}} = 3.92 \times 10^9\ \mathrm{M}^{-1}\ \mathrm{s}^{-1}$, in good agreement with the result obtained from Fig. 18.

In the experiment of Fig. 18, we have chosen a sample and temperature for which nuclear spin relaxation is very small [55]. If the nuclear spin-relaxation rate $2W_n$ constitutes a nonnegligible source of spin relaxation, then a more general analysis of the 2D ELDOR experiment is required. Note that W_n arises from rotational modulation of the electron nuclear dipolar interaction involving the ^{14}N nuclear spin, and it is an important parameter in the study of molecular dynamics [1, 55]. The 2D ELDOR spectrum of PD-Tempone in the

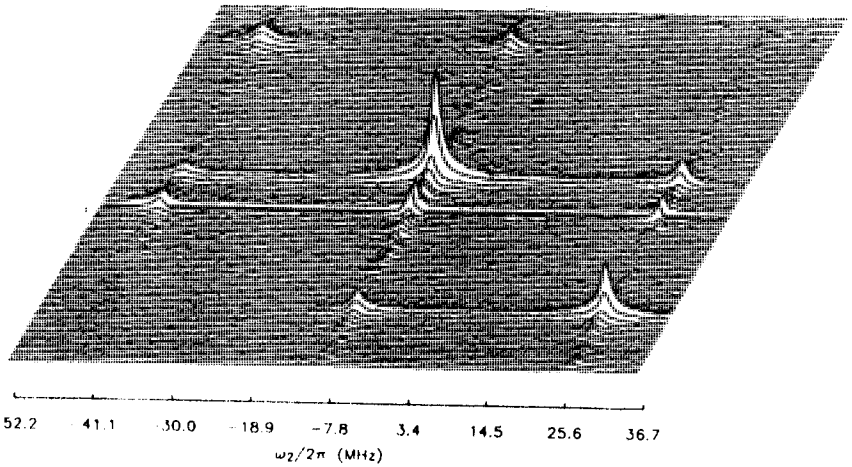

Fig. 21. Absolute value 2D ELDOR spectrum of 2.05×10^{-3} M PD-Tempone in liquid crystal S2 at 35.5 ± 0.5 °C obtained with the director aligned parallel to B_0; $\tau_p = 12$ ns; $\Delta t_1 = 7$ ns; $\Delta t_2 = 5.86$ ns; 128 samplings in t_1; eight-step phase-alternation sequence with 128 averages per step; deadtime in t_1, 66 ns; deadtime in t_2, 145 ns; mixing time, $T = 5.48 \times 10^{-7}$ s; 256 complex data points per FID extending to 1.5 μs; acquisition time, 51 min. From Ref. 46.

liquid-crystal S2 (Fig. 21) is an example of a 2D ELDOR experiment in which nuclear spin relaxation cannot be neglected. In this case Heisenberg exchange does not play a significant role in the transfer of magnetization. This is apparent by inspection of the contour map (Fig. 22) associated with the spectrum of Fig. 21 which shows no significant cross-peaks connecting the outer hf lines. This is consistent with a nuclear spin-relaxation mechanism where $\Delta M_I = \pm 1$, for example, from the electron nuclear dipolar interaction. The spectrum of Fig. 21 yielded the relaxation rate $2W_n = 4.25 \pm 0.25 \times 10^5\ s^{-1}$. The quantitative accuracy of this technique for determination of W_n was demonstrated by comparison with stimulated-echo (SE) results.

The quantitative agreement of 2D ELDOR and SE methods raises the question: Why perform 2D ELDOR experiments, which are significantly more sophisticated than stimulated echoes, when SE experiments yield the same results? The answer to this question is twofold. First, note that the SE experiment required the use of substantially larger sample volumes to obtain adequate sensitivity. This is because the stimulated echoes observed in these systems are about one order of magnitude smaller in signal voltage than the FIDs recorded in the 2D ELDOR experiment. Second, it is important to compare the methods of analysis required for the two types of data. In the case of 2D ELDOR, a direct determination of W_n and ω_{HE} is obtained by comparison of peak volumes (cf. below), whereas for SE a least-squares fit to a

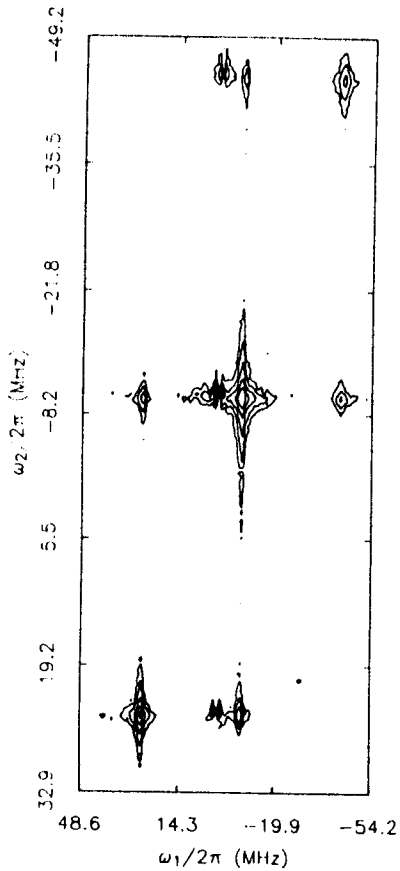

Fig. 22. 2D ELDOR contour map of the spectrum of Fig. 21. Note the absence of cross-peaks connecting the two outer hf lines, indicative of an ^{14}N nuclear spin-relaxation mechanism. From Ref. 46.

sum of exponentials is required. Unless extensive signal averaging is performed, the least-squares procedure will be susceptible to error, particularly in the case of $W_n/W_e \ll 1$ or $\omega_{HE}/W_e \ll 1$. This underscores the need for three SE experiments, each performed at a different hf line. The proper set of SE experiments therefore requires (1) substantially longer data acquisition times than 2D ELDOR; (2) greater minimum number of spins than 2D ELDOR; (3) a measurement of spectrometer deadtime; and (4) a five-parameter, nonlinear, least-squares fitting procedure. The SE experiment is nevertheless complementary to 2D ELDOR in that it provides a fairly accurate measurement of W_e that is not obtained in a single 2D ELDOR experiment, but can be obtained from 2D ELDOR results as a function of mixing time T, as discussed

below (or by studying "type E" axial peaks, cf. below and Ref. 43). (Note that these comments about SE also apply to saturation recovery (SR) [57]. In SE, however, the spins are first prepared in a well-defined state prior to studying their time evolution. Also, in SR one observes not an echo (nor an FID), but a low-power cw signal.)

Recently, a detailed study was completed utilizing 2D ELDOR and ESE to clarify more precisely the nature of rotational motion in a liquid crystalline smectic (lamellar) phase [12, 43]. This work demonstrates the power of the new methods in view of the more extensive and more accurate data they provide.

5.5 Theory of 2D ELDOR and COSY [8, 43, 46]

The FID following a single pulse is given by the expression

$$s(t) = B' \sum_j a_j \exp(-\Lambda_j t) \tag{28}$$

where the complex coefficients a_j are given by

$$a_j = \sum_{l,m} U_l O_{o,lj} O_{o,mj} U_m \tag{29}$$

according to the notation we have already introduced.

The expression for 2D ELDOR is

$$s'_{\text{ELDOR}}(T, t_1, t_2) = B' \sum_{l,m,n} c_{lmn} \exp(-\Lambda_n t_2) \left[\exp\left(-\frac{T}{\tau_m}\right)\right] \text{Re} \sum_j b_{lj} \exp(-\Lambda_j t_1) \tag{30}$$

where

$$c_{lmn} = \sum_{k,r} U_r O_{o,rn} O_{o,kn} O_{d,km} O_{d,lm} \tag{31}$$

and

$$b_{lj} = \sum_p O_{o,lj} O_{o,pj} U_p \tag{32}$$

where, for simplicity, we have ignored the V_j factors, corresponding to the assumption of uniform spectral rotation by the pulses. The result of Eqs. 30-32 is closely related to that of Eq. 19 for the field-swept MT experiment, except for the fact that an FID (rather than an echo is detected).

Equations 30-32 represent only one of several terms predicted by the theory; in particular, they represent the contribution to the 2D spectrum which provides the ELDOR information. We may identify four independent contributions to the time-domain spectral function $s(T, t_1, t_2)$:

$$s'_{(x,x,x)}(T, t_1, t_2) = s'_{\text{ELDOR}} + s'_{\text{Transverse}} + s'_{\text{Axial(E)}} + s'_{\text{Axial(M)}} \tag{33}$$

where (x, x, x) identifies, for each pulse, the axis of rotation by B_1. s'_{ELDOR} is the contribution given by Eqs. 30-32, while $s'_{\text{Transverse}}$ is the contribution associated with the transverse interference discussed above, and $s'_{\text{Axial(E)}}$ and $s'_{\text{Axial(M)}}$ are the terms associated with axial peaks [37]. The quadrature component is written analogously as

$$s''_{(y,x,x)}(T, t_1, t_2) = s''_{\text{ELDOR}} + s''_{\text{Transverse}} + s''_{\text{Axial(E)}} + s''_{\text{Axial(M)}} \tag{34}$$

The phase-cycling sequences cancel out $s_{\text{Transverse}}$ and $s_{\text{Axial(E)}}$. The $s_{\text{Axial(M)}}$ are removed by first measuring the constant baseplane offset described below.

In the case of Figs. 16 and 19, corresponding to the motional narrowing regime with three well-separated hf lines, our expressions are greatly simplified by the fact that $\mathbf{O}_o = \mathbf{1}$, the unit matrix, and we can write the ELDOR signal as

$$s'_{\text{ELDOR}}(T, t_1, t_2) = B' \sum_{n,m,j} c_{nmj} A_n(t_2) \left[\exp\left(-\frac{T}{\tau_m}\right)\right] \text{Re}[A_j(t_1)] \tag{35}$$

and

$$s''_{\text{ELDOR}}(T, t_1, t_2) = B' \sum_{n,m,j} c_{nmj} A_n(t_2) \left[\exp\left(-\frac{T}{\tau_m}\right)\right] \text{Im}[A_j(t_1)] \tag{36}$$

where $A_i(t)$ is defined by

$$A_i(t) = \exp(-\Lambda_i t) \tag{37}$$

The real coefficients c_{nmj} are defined by

$$c_{nmj} = U_n O_{d,nm} O_{d,jm} U_j \tag{38}$$

with

$$O_{d,nm} = \begin{array}{c} \\ -1 \\ 0 \\ +1 \end{array} \begin{array}{c} \begin{array}{ccc} 1 & 2 & 3 \end{array} \\ \begin{bmatrix} 3^{-1/2} & 2^{1/2} & 6^{-1/2} \\ 3^{-1/2} & 0 & -2(6)^{-1/2} \\ 3^{-1/2} & -2^{-1/2} & 6^{-1/2} \end{bmatrix} \end{array} \tag{39}$$

and with $n = M_1 = -1, 0, 1$ and

$$\tau_1^{-1} = 2W_e \tag{40}$$

$$\tau_2^{-1} = 2W_e + 2W_n + \omega_{\text{HE}} \tag{41}$$

$$\tau_3^{-1} = 2W_e + 6W_n + \omega_{\text{HE}} \tag{42}$$

(The presence of chemical exchange and/or pseudo-secular EED terms would lead to an effective exchange frequency ω_{EX} replacing ω_{HE} in these expressions (1, 4, 49).)

The U_n in Eq. 38 are given by $U_n = i\varepsilon/2$, where $-\varepsilon$ is the equilibrium population difference for an isotropic system, given by $g\beta_e B_0/k_B T$ in the high-field limit. Equations 39–42 are appropriate when the nonsecular contributions from the g tensor, hf tensor, and EED tensor may be neglected. More generally, up to five τ_m would be required for a nitroxide. This case is discussed in detail elsewhere [43, 46].

We see immediately from Eqs. 35 and 36 that the effect of the 2D quadrature phase-alternation scheme is to select the real part of the time-domain spectral function $A_j(t_1)$ in the case of s' and the imaginary part in the case of s''.

Upon FT with respect to t_2 we obtain $\hat{s}_{(x,x,x)}(T, t_1, \omega_2)$ and $\hat{s}_{(y,x,x)}(T, t_1, \omega_2)$ at which time we form [7]

$$\hat{s}(T, t_1, \omega_2) = \mathrm{Re}(\hat{s}_{(x,x,x)}) + i\mathrm{Re}(\hat{s}_{(y,x,x)}) \tag{43}$$

Then FT with respect to t_1 yields the 2D spectrum given by

$$S_{\mathrm{ELDOR}} = S'_{\mathrm{ELDOR}}(T, \omega_1, \omega_2) + iS''_{\mathrm{ELDOR}}(T, \omega_1, \omega_2) \tag{44}$$

with

$$S'_{\mathrm{ELDOR}}(T, \omega_1, \omega_2) = B' \sum_{n,m,j} c_{nmj} \frac{1}{i\omega_1 - \Lambda_j}\left[\exp\left(-\frac{T}{\tau_m}\right)\right]\mathrm{Re}\frac{1}{i\omega_2 - \Lambda_n} \tag{45}$$

and with $S''_{\mathrm{ELDOR}}(T, \omega_1, \omega_2)$ given by Eq. 45 but with Re replaced by Im.

As noted above, we are left with the one remaining unwanted $S_{\mathrm{Axial(M)}}$ after phase cycling, and it is removed during data analysis. One finds [8, 43] that $s'_{\mathrm{Axial(M)}}(T, t_2)$ is independent of t_1, and it constitutes the only contribution to $s'_{(x,x,x)}(T, t_1, t_2)$ with this property. Thus, we first estimate a constant baseplane offset in $\hat{s}'_{(x,x,x)}(T, t_1, \omega_2)$, which we identify with $\hat{s}'_{\mathrm{Axial(M)}}(T, \omega_2)$. Then we subtract this baseplane from $\hat{s}'_{(x,x,x)}(T, t_1, \omega_2)$, and repeat this procedure with $\hat{s}''_{(y,x,x)}$ prior to FT with respect to t_1. The experimental implementation is not perfect. There is residual amplitude associated with axial peak contributions, and it gives rise to the distortions seen along $\omega_1 = 0$ in the spectra of Figs. 14, 16, and 19. (Additional distortions near $\omega_1 = 0$ arise from the extra amplitude modulation in t_1 due to distortions in the second mw pulse (causing a variation of the rotation angle for this pulse) as a function of interpulse delay t_1, which is a problem analogous to that in NMR [58] and from drifts in B_0 occurring as t_1 is stepped out.) By combining Eqs. 38 and 45 and introducing the factors V_j, we obtain

$$\mathrm{Re}\, S'_{\mathrm{ELDOR}}(T, \omega_1, \omega_2) = B' \sum_{n,m,j} U_n V_n \frac{T_{2,n}}{1 + (\omega_2 - \omega_n)^2 T_{2,n}^2} \times U_j^2 V_j^2 \frac{T_{2,j}}{1 + (\omega_1 - \omega_j)^2 T_{2,j}^2} O_{\mathrm{d},nm} O_{\mathrm{d},jm} \exp\left(-\frac{T}{\tau_m}\right) \tag{46}$$

applicable in the motional narrowing regime with well-separated hf lines. Here, $T_{2,j}$ and ω_j are the T_2 and resonant frequency of the jth hf line. For the purpose of simulation one need only compute Eq. 46.

We have neglected inhomogeneous broadening in the above analysis, since it does not play a significant role in the interpretation of 2D ELDOR data in the motional narrowing regime (other than to broaden each resonance line by a small amount). The effect of including significant inhomogeneous broadening in the theory is that there would be several types of spin echo, namely, three spin echoes, i.e., one from each pair of pulses, plus a stimulated echo and a twice refocused echo. (These matters are discussed elsewhere [23, 30].) These are the terms that would be important for slow-motional 2D ELDOR spectra, where $T_2^* < \tau_d$, so an FID technique would not be appropriate. Instead, one could observe the stimulated echo, which has a structure very similar to that of Eqs. 30–32, whereas the others would be canceled by phase cycling.

Before discussing 2D ELDOR further, we note that a similar analysis leads to motional narrowing expressions for COSY-ESR:

$$s'_{\mathrm{COSY}}(t_1, t_2) = B' \sum_n U_n^2 A_n(t_2)\mathrm{Re}[A_n(t_1)] \tag{47}$$

and

$$s''_{\mathrm{COSY}}(t_1, t_2) = B' \sum_n U_n^2 A_n(t_2)\,\mathrm{Im}[A_n(t_1)] \tag{48}$$

Equations 47 and 48 predict a COSY spectrum without cross-peaks, consistent with the experimental result of Fig. 16. However, given sufficiently rapid exchange (e.g., ω_{HE} comparable to the hyperfine splittings), $\mathbf{O}_o$ is no longer simply the identity operator $\mathbf{I}$, and cross-peaks are predicted to appear in the COSY spectrum. It is also true in general that $\mathbf{O}_o \neq \mathbf{I}$ in the slow-motional regime; hence, one finds cross-terms in the appropriate slow-motional analogs of Eqs. 47 and 48.

We now consider the analysis of the 2D ELDOR experiment for a motionally narrowed nitroxide spectrum with three well-separated hf lines characteristic of a nitroxide. We obtain from the experiment the 3×3 matrix $\mathbf{Q}(T)$ consisting of the volume integrals. (The matrix $\mathbf{Q}(T)$ is defined such that Q_{mj} is the volume integral of the cross-peak located at coordinates $(\omega_1, \omega_2) = (\omega_j, \omega_m)$.) According to Eq. 46 we can write

$$Q_{nj}(T) = E \sum_m O_{\mathrm{d},nm} O_{\mathrm{d},jm} \exp\left(-\frac{T}{\tau_m}\right) \tag{49}$$

where E is a spectrometer constant. The expressions for the matrix elements Q_{nj} (within the spectrometer constant) are given in Table 3 for the case when Eqs. 39 and 40 are applicable. In the analysis of experiments, one utilizes ratios: $f_{mj} \equiv Q_{mj}/Q_{jj}$, thereby canceling the spectrometer constant, E.

In the very simplest case where W_e is negligible and Heisenberg exchange is the only source of magnetization transfer, one obtains, after some algebra,

TABLE 3. Matrix Elements $E^{-1}Q_{nm}(T)$[a]

Auto-peaks[b]	
$E^{-1}Q_{\pm1,\pm1}$	$\frac{1}{3}\exp\left(-\frac{T}{\tau_1}\right)+\frac{1}{2}\exp\left(-\frac{T}{\tau_2}\right)+\frac{1}{6}\exp\left(-\frac{T}{\tau_3}\right)$
$E^{-1}Q_{0,0}$	$\frac{1}{3}\exp\left(-\frac{T}{\tau_1}\right)+\frac{2}{3}\exp\left(-\frac{T}{\tau_3}\right)$
Cross-peaks	
$E^{-1}Q_{0,\pm1}=E^{-1}Q_{\pm1,0}$	$\frac{1}{3}\exp\left(-\frac{T}{\tau_1}\right)-\frac{1}{3}\exp\left(-\frac{T}{\tau_3}\right)$
$E^{-1}Q_{\pm1,\mp1}$	$\frac{1}{3}\exp\left(-\frac{T}{\tau_2}\right)-\frac{1}{2}\exp\left(-\frac{T}{\tau_2}\right)+\frac{1}{6}\exp\left(-\frac{T}{\tau_3}\right)$

[a] This is the case of negligible nonsecular terms.
[b] These apply both to 2D ELDOR and to stimulated echoes from the three hyperfine lines.

$$\omega_{HE}=\frac{1}{T}\ln\frac{2f_{mj}V_jr_{2j}+V_mr_{2m}}{V_mr_{2m}-f_{mj}V_jr_{2j}} \tag{50}$$

Here the r_{2j} measure the deadtime reduction factors (as well as the filtering effects of the resonator with its finite Q) on the FIDs collected as a function of t_2. The products V_jr_{2j} are determined by measuring the normalized peak areas obtained from a single-pulse FID collected under the same conditions (i.e., same deadtime, pulse length, etc.) as the 2D ELDOR spectrum.

Note that Eq. 50 predicts that all six cross-peaks equivalently reflect the exchange process, and hence that six independent measurements of the exchange rate ω_{HE} are obtained from a single 2D spectrum. The equivalence of the six cross-peaks is a manifestation of the lack of a selection rule for the exchange mechanism [49]; that is, both $\Delta M_I=\pm1$ and $\Delta M_I=\pm2$ transitions are equally probable (cf. Figs. 18 and 19).

The W_n mechanism and the exchange mechanism may be distinguished in these spectra as a result of their different selection rules as we have already noted. Unlike exchange, the W_n mechanism obeys the selection rule $\Delta M_I=\pm1$ and thus gives rise predominantly to cross-peaks connecting only adjacent hf lines (cf. Fig. 21), but see below. Thus, the geometrical pattern of the spectral

contours may be utilized to obtain information regarding the mechanism of magnetization transfer prior to the application of Eq. 43 or its analogs for $W_n\neq0$. If we consider, for example, a case where only cross-peaks for which $\Delta M_I=\pm1$ are significant, we can write by analogy to Eq. 43.

$$6W_n=\frac{1}{T}\ln\frac{2\hat{Q}_{mj}V_jr_{2j}+V_mr_{2m}}{V_mr_{2m}-\hat{Q}_{mj}V_jr_{2j}} \tag{51}$$

which applies to the two cross-peaks for which $m=\pm1$ and $j=0$. In Eq. 51, $\hat{Q}_{mj}\equiv Q_{mj}/Q_{\infty}$. Thus, in the event that $\omega_{HE}=0$ one can obtain W_n directly from two of the four cross-peaks with the application of Eq. 51. The expression for the other two cross-peaks (i.e. $m=0$, $j=\pm1$), is somewhat more complicated. These cross-peaks nevertheless directly yield W_n, provided exchange is absent. If cross-peaks for which $\Delta M_I=\pm2$ are significant, then the left side of Eq. 51 requires an additive factor involving ω_{HE}. The full set of linear equations applicable when $\omega_{HE}\neq W_n\neq0$ has been given elsewhere for all six cross-peaks [43, 46].

The overdetermined set of six linear equations may be used to obtain both W_n and ω_{HE}. Note that the presence of cross-peak intensity at $\Delta M_I=\pm2$ does not always imply the presence of Heisenberg exchange; the W_n mechanism may also contribute intensity to these peaks by a small amount, but only for sufficiently long mixing times T; that is, when $W_nT>1$ (cf. Table 3). The absence of $\Delta M_I=\pm2$ peaks for shorter mixing times is easily shown by expanding $Q_{\pm1,\mp1}$ given in Table 3 to lowest power in W_nT.

These expressions for relative peak volumes for a given mixing time T do not by any means exhaust the available sources of data from the 2D ELDOR experiment. There is, after all, a third dimension available, that of mixing time T. From a series of 2D ELDOR spectra at different values of T, one can map out the T dependence of all nine auto- and cross-peaks. Thus, for example, from Table 3 in the simple special case of $W_n=0$, we obtain for the auto-peaks

$$Q_{nn}(T)\propto\exp(-2W_eT)+2\exp[-(2W_e+\omega_{HE})T]\qquad n=-1,0,1 \tag{52}$$

and for the cross-peaks

$$Q_{nm}(T)\propto\exp(-2W_eT)-\exp[-(2W_e+\omega_{HE})T]\qquad n\neq m \tag{53}$$

In general, each peak shows a time evolution given by a sum of exponentials which may be fit to provide W_e, W_n, and ω_{HE}. The Q_{nn} versus T represents equivalent information to that of stimulated echoes, whereas the Q_{nm} versus T for $n\neq m$ are equivalent to that from ELDOR echoes. We have found that for accurate and reliable estimation of relaxation rates, it is a good idea to obtain 2D ELDOR at 3 or 4 values of T for which all the peaks are prominent. As 2D ELDOR techniques improve and data acquisition rates are increased, it should

become practical to obtain 2D ELDOR for significantly more values of T, which would then more truly represent a 3D experiment.

5.6 Future Uses of 2D FT-ESR

We have illustrated how FT-ESR is capable of routine use in several applications involving motionally narrowed spectra. We have shown the utility of two-dimensional FT spectroscopy as a double-resonance technique that yields quantitative information without necessarily requiring simulation or least-squares fitting of the data. We did find, however, that least-squares fitting in the form of linear prediction is a convenient method for projection of the pure 2D absorption representation of 2D ELDOR data necessary for determining volume integrals of the 2D absorption lines. It can also be effectively utilized to remove artifacts, such as residual axial peaks, and to significantly improve the signal-to-noise ratio.

In the application of this technique to slow-tumbling motions of, for example, nitroxides, one would obtain all of the ELDOR data in a single 2D spectrum. Such spectra would yield information about the couplings between dynamic spin packets corresponding to different molecular orientations which can provide considerable insight into the microscopic details of the motional process [1, 5, 14, 23, 30, 59]. The implementation of a 2D ELDOR experiment for the study of slow-tumbling motions would be somewhat different than what is described for motionally narrowed systems. FIDs in these systems are, in general, rapidly damped as a result of the large inhomogeneous line widths, which are not averaged by the motion as in the motionally narrowed spectra. The FID will, in general, be lost in the dead time following a microwave pulse. In these instances, the transverse magnetization can still be refocused into a spin echo. In the 2D ELDOR experiment one would have the option of applying an additional refocusing pulse or of recording the stimulated echo following the third pulse. The latter method would have the advantage that axial peaks will not be refocused and therefore cannot contribute intensity to the 2D ELDOR spectrum.

In another application, the implementation of SECSY to slow-tumbling nitroxides would be identical to the method described in Section 5.2 for motionally narrowed spectra, except that reduction of the dc magnetic field homogeneity is not required. This SECSY application would be the 2D FT analog of the field-swept 2D experiment described in Section 3. It would have the advantages of (1) greatly reduced data acquisition times; and (2) pulse widths significantly shorter than the relevant T_2's.

In general, for slow-motional studies by 2D ESR, one must be concerned about the effects of nuclear modulation (e.g., ESEEM). On the other hand, these effects could provide useful information, (cf. Chapter 5). We have examined in detail [60], the patterns predicted for SECSY, COSY, and 2D ELDOR in the rigid limit. SECSY provides a 2D representation of the ESEEM. In the rigid limit, COSY and 2D ELDOR are predicted to yield very similar results that are

quite different from SECSY. In COSY and 2D ELDOR the modulation leads to the appearance of "forbidden" auto-peaks as well as the appearance of cross-peaks, due to coherence transfer by the hyperfine interaction. In all cases, these effects are maximized when the hyperfine coupling is roughly the same order-of-magnitude as the nuclear Zeeman energy. We illustrate the relative features of SECSY and 2D ELDOR (or COSY) with a series of simulated polycrystalline 2D spectra (Fig. 23). Figure 23*a* shows the 2D ELDOR spectrum of a polycrystalline sample, where a single proton is coupled to the unpaired electron. In addition to the "allowed" peaks on the diagonal, the spectrum exhibits some structure of weaker peaks, off-diagonal and on the diagonal. If significant inhomogeneous broadening is present, this structure may be partly or even completely hidden by the broadening. This problem can be eliminated by using the SECSY experiment (Fig. 23*b*). If there are two nuclei, the 2D ELDOR method can give information on their relative orientation. If both nuclei have exactly the same orientation with respect to the magnetic field, the spectrum of a polycrystalline sample consists of a single peak at zero frequency for the magnetic parameters utilized (Fig. 23*c*). But if they are oriented differently, the spectrum changes, depending on the relative angle. Figure 23*d* is the 2D ELDOR spectrum of a polycrystalline sample of molecules in which the relevant nuclei are two protons, the relative angle being a tetrahedral angle. The ESR-SECSY line shape for this case is shown in Fig. 23*e*. (When we consider a nitroxide at X band we find virtually no nuclear modulation effects in 2D ESR for ^{14}N, because $\omega_N \ll a_N$, whereas proton or deuteron shf yields significant nuclear modulation effects, provided there are substantial numbers of equivalent nuclei.) Also, we mention that new phase cycling sequences have been found which are predicted to significantly simplify the 2D ESR spectra containing nuclear modulation [60]. This also includes new phase cycling methods for the removal of axial peaks [60]. There are many possibilities for pulse sequences [e.g., 61, 62], to explore in terms of the 2D FT-ESR format.

Many other possibilities exist for the application of other two-dimensional spectroscopies to ESR. One potential application of COSY-ESR could be to the study of distances in macromolecules. Suppose an ^{14}N and an ^{15}N label are placed at two distinct sites in a protein, and in a rigid-limit spectrum they are coupled by the dipolar interaction between the two electron spins. Then from the COSY cross-peaks between the ^{14}N and ^{15}N spectra, one could, in principle, measure the dipolar interaction from which $1/r^3$ could be obtained.

In cases where B_1 field strengths are insufficient for total spectral coverage, variations of the techniques described here may be of interest. These are techniques of two-dimensional correlation spectroscopy that require that only a limited region of the spectrum be irradiated (called "soft COSY" techniques [63]). A soft 2D ELDOR spectra would provide information about the couplings among only those dynamic spin packets rotated by the microwave pulse. In these experiments one could collect several such 2D spectra, each focusing on a different region of the spectrum, and then combine the data during

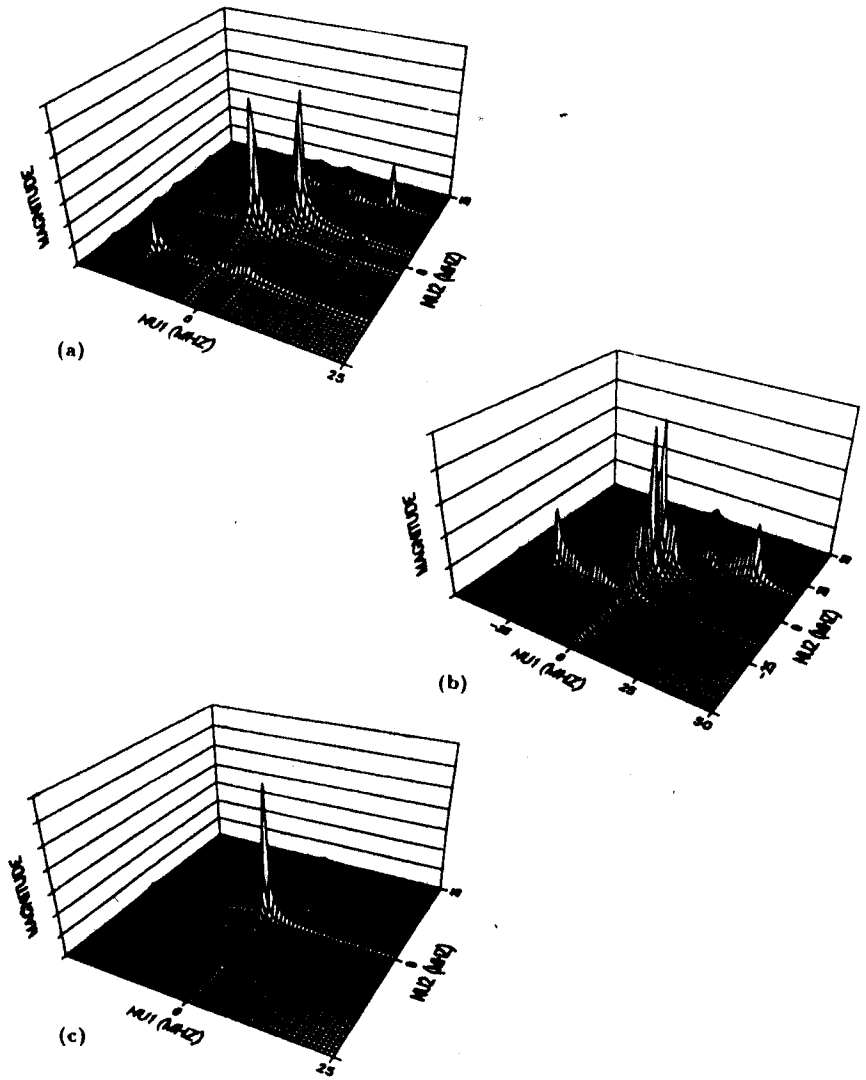

Fig. 23. Simulations of effects of nuclear modulation in 2D ESR for polycrystalline samples. Cases shown are for protons with axially symmetric hf tensor: $A_{\parallel} = 8.14$ G, $A_{\perp} = -2.03$ G (corresponding to $\bar{a} = 3.8$ MHz, $D = 19.0$ MHz, $B_0 = 3300$ G ($\omega_1 = 14.0$ MHz), $T_2 = 540$ ns. (These results are readily scaled to other hf values and B_0 by keeping $A_{\parallel}/B_0$ and $A_{\perp}/B_0$ constant.) The appropriate phase alternation sequences as discussed in Sections 5.3 and 5.4 were utilized. (*a*) 2D ELDOR: one proton; (*b*) SECSY-ESR: one proton; (*c*) 2D-ELDOR: two protons; identical orientation of hf tensor.

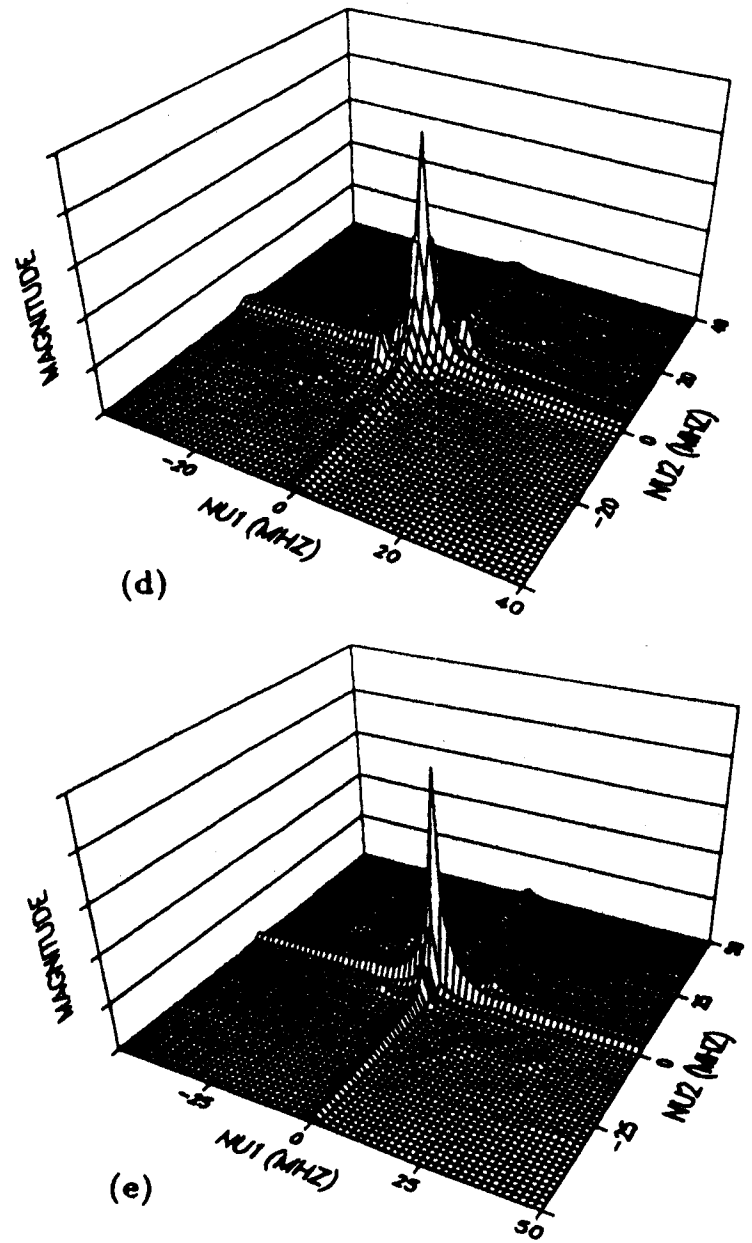

Fig. 23 (continued). (*d*) 2D ELDOR: two protons, hf tensors 109.5° relative to each other; (*e*) SECSY-ESR: two protons, hf tensors as in (*d*).

data analysis. Related techniques are already frequently utilized in NMR for 2D nuclear Overhauser spectroscopy.

It is clear that full bandwidth irradiation techniques will be limited to specific suitable applications in ESR. These will probably not, for the foreseeable future, include transition metals in liquid solution. Transition metal spectra have bandwidths of up to several gigahertz, requiring B_1's of 10^2–10^3 G, and their T_2's in liquids are too short (typically less than or on the order of nanoseconds). Nevertheless, solid-state experiments on inorganic ions by field-swept 2D ESE (e.g., Sections 3 and 4) are quite feasible. The methods described in this section are generally applicable to studies of organic free radicals, because their spectral bandwidths usually do not exceed 100–200 MHz, and their T_2's are usually significantly greater than a nanosecond.

6. INSTRUMENTATION

6.1 Microwave Section of Spectrometer

A block diagram of the spectrometer, which may be used either for 2D FT or 2D swept-field experiments, is given in Fig. 24. The microwave (mw) source consists of a reflex klystron that has been phase locked to a 15-MHz crystal oscillator providing long-term frequency stability of better than 1 part in 10^7. The mw radiation is passed through a calibrated variable attenuator and a 2-bit PIN diode phase shifter that has been optimized for operation at 9.25 GHz. The phase shifter has mw transition times of 7 ns (10–90% mw) and a 20-ns insertion delay (50% TTL–10% mw). Mw pulse waveforms are generated with the aid of two reflective PIN diode switches biased with emitter coupled logic (ECL) compatible drivers giving 1-ns rise times with 60-dB isolation.

For generating mw power we employ a traveling wave tube (TWT) amplifier which has been modified to facilitate rapid direct anode modulation. Rapid anode switching eliminates the substantial noise power associated with the TWT amplifier after the mw pulse, which otherwise corrupts detection and increases spectrometer deadtime. This system is capable of producing well-defined pulses of 5-ns duration. The anode modulator is described in Section 6.3.

The 1-kW mw pulses pass through a rotary-vane attenuator and are routed by a four-port circulator to a microwave resonator. We initially utilized a TE102 mode rectangular cavity but more recently we have found a specially designed bridged loop gap resonator [43] more desirable (cf. Section 7.2). We describe the cavity here. The cavity coupling hole (a centered circular iris) was enlarged to reduce the loaded Q factor of the resonator (loaded Q will henceforth be referred to as just Q). A brass screw inserted into the B field of the cavity allows tunability of the resonant frequency. The Q is ~ 100, consistent with a half-power full bandwidth of 90 MHz (at 9.25 GHz) and a time constant of 3.4 ns; such a resonator will admit a pulse of duration as short as ~ 7 ns [64]. After loading the cavity, the resonant frequency is adjusted to 9.25 GHz for which the spectrometer operating conditions have been optimized.

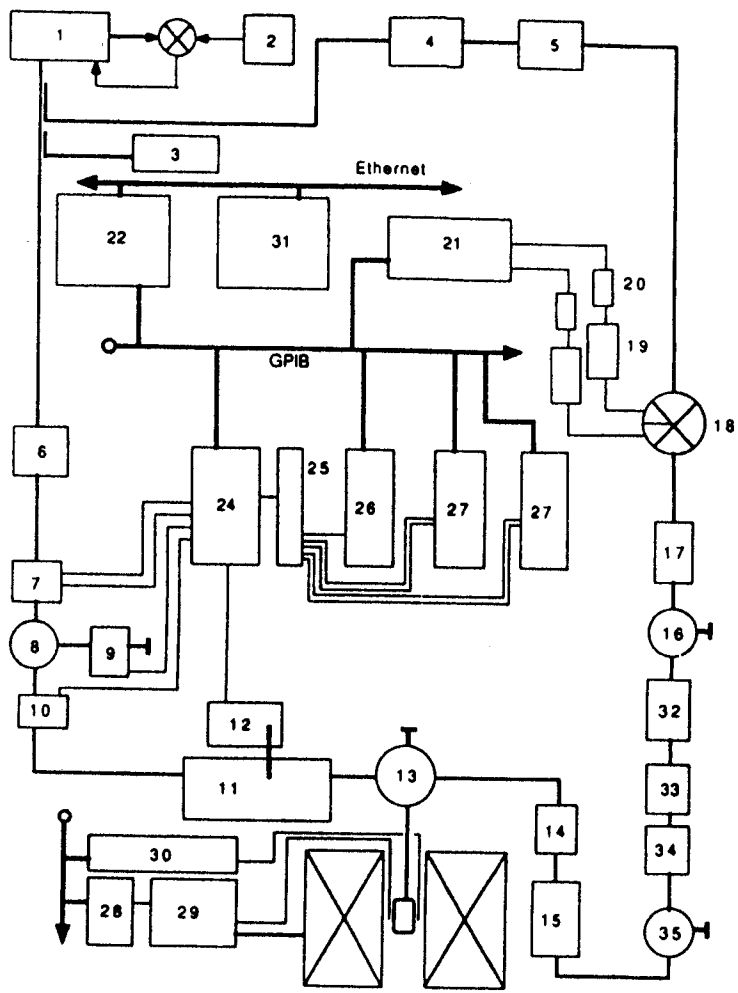

Fig. 24. 2D FT-ESR spectrometer block diagram. 1, Varian VA-297V klystron; 2, Microwave Systems MOS frequency stabilizer; 3, Systron Donner 1255A frequency meter; 4, Systron Donner DBG-915 variable phase shifter; 5, Wave line 611 variable attenuator; 6, Waveline 612 variable attenuator; 7, Vectronix Microwave DP629.25HS digital phase shifter; 8, Western Microwave circulator; 9, 10, M/A-COM 96341 PIN diode SPST switches; 11, Litton 624 TWT amplifier; 12, modulator; 13, Junction Devices 115XHD circulator; 14, Hewlett Packard 33711A PIN diode limiter; 15, Narda Microwave N6244S-95 GaAsFET amplifier; 16, Western Microwave isolater; 17, Narda Microwave 4563 DC block; 18, Anaren 250270 quadrature IF mixer; 19, Comlinear CLC100 IF amplifiers; 20, Mini-Circuits BLP-300 low-pass filters; 21, Hewlett Packard

Mw signal is directed by the four-port circulator into a PIN diode limiter. The limiter clips the waveform at 17 dBm to protect the GaAsFET amplifier from reflected power during a pulse. The low-noise amplifier (3.5 dB noise figure) provides 35-dB gain with saturated signal power exceeding 15 dBm. A second stage of amplification consists of a 12-dB GaAsFET amplifier with saturated signal power of 20 dBm, preceded by a limiter and variable attenuator. (More recently this two-stage GaAsFET amplifier arrangement has been replaced by a single 50-dB GaAsFET amplifier.) The amplified signal enters the mw port of a quadrature IF mixer (QIFM). The attenuator/amplifier network facilitates adjustment of the QIFM signal input power to efficiently drive the mixer diodes. The QIFM splits the mw with a 3-dB quadrature hybrid power divider, each output of which enters a mixer. The two mixers share the local oscillator (LO) signal derived from the homodyne reference arm.

The IF outputs of the mixers should ideally be of equal amplitude and in phase quadrature; in practice, however, phase and amplifier imbalances in the hybrids and mixers result in deviations from phase quadrature and amplitude equality. The appearance of image peaks (reflections about the IF origin) in the ESR spectrum is a manifestation of phase and amplitude imbalances. An image peak may interfere with another resonance and cause a distortion of the ESR spectrum. The magnitude of an image peak relative to its parent peak defines the image rejection of the QIFM [65]. Typical commercial QIFMs specify an image rejection of -20 dB, a value we have found to be insufficient for ESR applications. To circumvent the shortcomings of the quadrature detector we apply the image-cancellation phase-alteration sequence known as CYCLOPS [48]. We record four FIDs with relative mw phases of 0, 90, 180, and 270°. An appropriate linear combination of the four complex time series amounts to an orthonormalization of the FID, provided that the mw phase shifts are very precise, and the insertion loss of each PIN diode phase shifter is not too severe. To guarantee the precision of the phase shifts, we operate the spectrometer within a frequency band (9.25 ± 0.05 GHz) for which the digital phase shifter has been optimized. Within this range, we obtain image rejection of -40 dB.

HP54100A digitizing oscilloscope; 22, Digital Equipment LSI11/73 minicomputer; GPIB, National Instruments GPIBV11-2 DMA interface controller; 24, pulse control unit (PCU); 25, ECL OR gate and TTL → ECL converter; 26, Precision Instruments 9650 digital delay generator, modified for ECL output; 27, Berkeley Nucleonics 7030A digital delay generators; 28, Fieldial interface module (FIM); 29, Varian Fieldial Mark II field regulated magnet power supply; 30, Varian 929801 NMR gaussmeter; 31, SUN Microsystems 3/60 workstation; 32, Avantek AFT-12662 GaAsFET amplifier; 33, Hewlett Packard 33711A PIN diode limiter; 34, Narda Microwave 4768 variable attenuator; 35, Western Microwave isolator. From Refs. 8 and 43.

6.2 Digital Electronics

A block diagram of the spectrometer data acquisition system is given in Fig. 25. A general purpose interface bus (GPIB, IEEE std. 488-1978) interconnects an 18-MHz LSI11/73 minicomputer with the spectrometer instrumentation. Communication between the LSI11 bus and the GPIB is facilitated by a direct memory access (DMA) interface controller supporting data transfer rates of 500 kbyte/s. Because of the large amount of data collected in a 2D experiment, the data transfer time constitutes a significant fraction of the total data

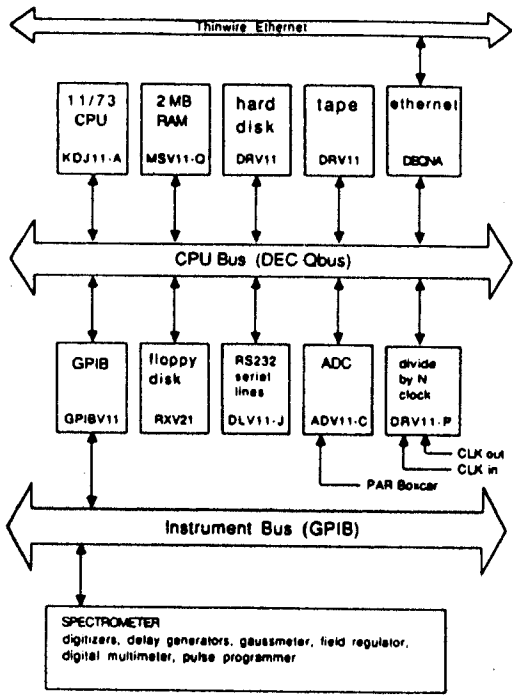

Fig. 25. Data acquisition system (top left to bottom right): Thinwire ethernet (RG-58U coax); DEC KDJ11-A PDP11/73 CPU; DEC MSV11-QB 2 Mbyte MOS memory; USDC 1101 host adapter (RK07 disk controller); USDC 1101 host adapter (TU10 tape controller); DEC DEQNA ethernet controller; DEC LSI bus ('Q' bus); National Instruments GPIBV11-2 DMA GPIB controller; Data Systems Design DSD 440 interface (RX02 floppy disk controller); Sigma Information Systems SCD-DLV11J 4-channel RS232 serial line interface; DEC ADV11-C analog-to-digital converter, divide-by-N clock (cf. Section 6.2) on DEC DRV11-P Qbus interface; General purpose interface bus; spectrometer instrumentation. From Ref. 43.

collection time. Transient recorders are usually limited to data transfer rates of well below 500 kbyte/s and should be selected with attention to this specification. 2D data acquired on the LSI11 is transferred to a 32-bit Sun Microsystems 3/60 workstation via thinwire ethernet. A 2D data file containing 256 complex FIDs can be transferred in 50 s. Fourier transformation and graphical presentation of 2D data is performed by the Sun workstation, thereby freeing the LSI11 for further data acquisition.

*6.2.1 **Pulse Programmer*** Timing of the logic control pulses to the PIN diode switches, modulator, and digital phase shifters is facilitated by a pulse control unit (PCU). The PCU is interfaced to the minicomputer via the GPIB with the aid of a Berkeley Nucleonics 8088 GPIB/BCD protocol converter. The interface allows rapid programmability of the number of mw pulses (as many as 15) and a four-bit pattern associated with each pulse, which determines the TTL logic states of four external devices during that pulse. Data are stored in successive locations of a 16 × 4, 15-ns RAM. A four-bit word is retrieved from location n synchronously with the trailing edge of mw pulse number $n - 1$. In this way the PCU can modify the external signals well before the mw pulse. The RAM address pointer is reset following the final pulse of a sequence by a one-shot timeout circuit. Two of the external logic signals are reserved for the digital phase shifter, while the other two are for options such as a digital attenuator. The timebase of the PCU is established by a train of ECL pulses from the digital delay generators.

*6.2.2 **Field Regulator Interface*** Computer control of the dc magnetic field is facilitated by a Fieldial interface module (FIM). The FIM receives two bits of data from the 11/73. Each bit controls a relay connected in parallel with the sweep-up or sweep-down front-panel switches on the Fieldial Mark II. By monitoring the absolute field with a GPIB-interfaced NMR gaussmeter, we obtain a field setability of 1 part in 10^5, or roughly 30 mG at X band. Photodiodes provide optical isolation between the relays and the FIM to protect the FIM against spikes generated by relay contact closures.

*6.2.3 **ESE Acquisition Subsystem*** In many applications of electron spin-echo spectroscopy it is sufficient that the mw pulses excite only a narrow portion of the ESR spectrum (cf. Section 2). The amplitude of the spin echo is recorded as a function of the interpulse delay, and, if desired, the experiment is repeated after incrementing the dc magnetic field (cf. Sections 3 and 4). An acceptable technique for recording partial excitation echoes is to gate the echo with a sample-and-hold aperture, accumulating charge on a capacitance over many repetitions of the pulse sequence. This is the concept of the familiar "boxcar" integrator. For data acquisition using the gated integrator we have constructed an LSI11 bus divide-by-N clock which synchronizes the spectrometer (i.e., the PCU) with the 11/73. The CPU enters the requested count into the clock

interface via the LSI bus. Clock pulses from the external timebase pass through the divide-by-N clock en route to the boxcar sample-and-hold aperture trigger. When the count reaches the preprogrammed value, trigger pulses to the boxcar are suspended, the divide-by-N clock interrupts the 11/74, and a conversion of the analog boxcar output is performed by a 12-bit LSI11 bus analog-to-digital converter. Time delays and phases are updated via the GPIB before the next countdown sequence is initiated. For acquisition of a two-pulse envelope, we alternate the phases of the mw pulses between 0°, 0° and 180°, 0° following each analog-to-digital conversion to achieve optimal cancellation of unwanted coherents (such as FID) that do not refocus with the spin echo. Device handlers for the narrowband excitation experiments were written in PDP11 assembly language for efficient pulse synchronization and data retrieval.

6.3 TWT Anode Modulator

Electron spin-echo (ESE) and Fourier transform ESR measurements are typically performed at frequencies in the range 1–18 GHz with high-power pulses requiring the use of TWT amplifiers. Duty cycle limitations of high-power TWT amplifiers usually require modulation of the TWT anode to produce an envelope of gain surrounding the low-power microwave pulse. Commercial modulators typically produce pulses to the anode with 150-ns transition times. In pulsed ESR applications it is usually necessary to record the intensity of the echo as soon as possible following the refocusing pulse in order to maximize the signal/noise ratio and to prevent the loss of rapidly decaying signal components. This same principle applies to detection of an FID following a single $\pi/2$ pulse (or multiple pulses in two-dimensional spectroscopy). One limitation on the spectrometer deadtime (i.e., the time delay after the pulse before the onset of detection) is the speed at which the anode voltage may be shut off following the mw pulse. Detection of the echo or FID is corrupted by noise emitted by the TWT when there is positive anode voltage but no mw power at the input to the amplifier. This is the case when using commercial TWT amplifiers during the ~ 150-ns transition period associated with the turnoff of the anode. Any reduction of this transition time should enable a reduction of spectrometer deadtime.

In an effort to enhance TWT amplifier performance in pulsed ESR applications, we have developed a fast interstage driver capable of operating at high slew rates into a capacitive load [43]. A schematic diagram is given in Fig. 26. The importance of the driver section to overall modulator performance may be understood by envisioning the driver as an active network that interfaces a TTL-compatible input to the gate of a power MOSFET device without introducing additional edge transition time. In the process of translating switching thresholds and providing substantial power gain over a very wide bandwidth, the driver is capable of sourcing and sinking high peak currents across a highly reactive load without instability. The modulator output rise and fall times are in the 7-ns range, and the anode voltage rise and fall times are in

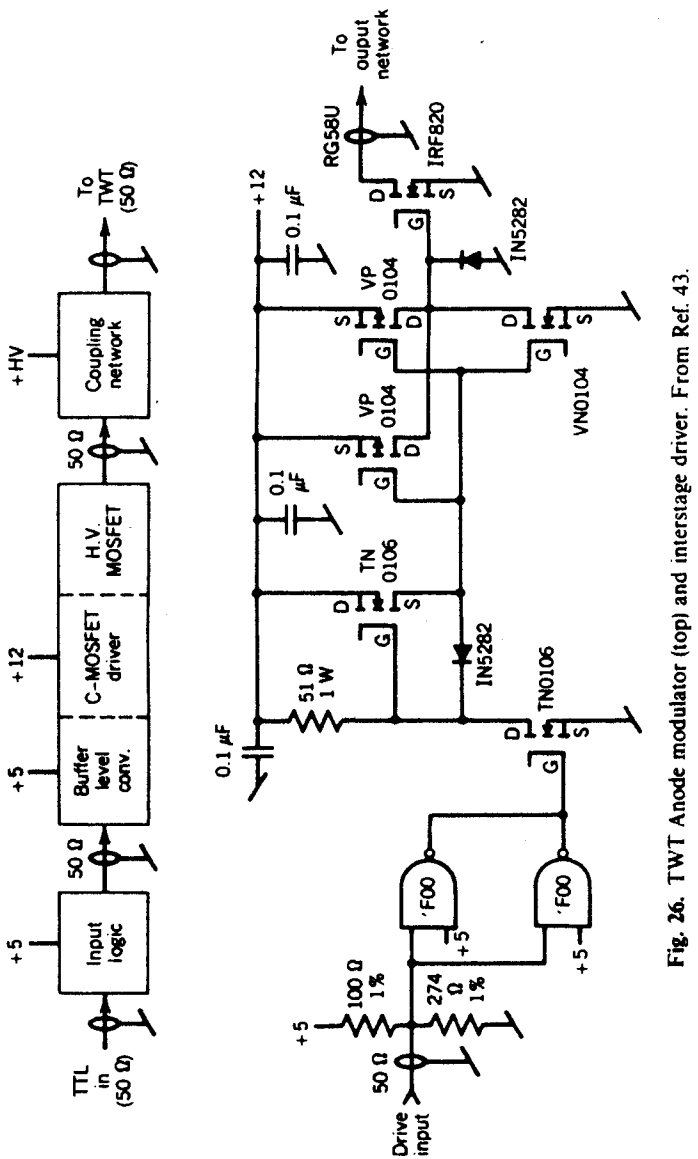

Fig. 26. TWT Anode modulator (top) and interstage driver. From Ref. 43.

the 3- to 4-ns range. As a result of this modulator performance, the TWTA output drops from 1 kW to below 1 mW in 7 ns. However, a small low-level broad-band signal decays, to the thermal noise level of -90 dBm (10^{-12} W) in 100 ns. We have designed a fast high-power microwave switch following the TWTA, which is estimated to reduce this additional noise signal by over 35 dB to further reduce dead time. The driver for this switch is similar in concept to that for the TWT anode modulator.

7. EXPERIMENTAL ASPECTS

7.1 Data Acquisition

The fundamental theorem in the discrete representation of continuous functions is the familiar Nyquist sampling theorem [66]. Consider the case of the undamped sinusoid, that is, a signal represented by a single Fourier component. The discrete representation of a sinusoid of frequency f_s Hz requires that we sample the function at least every $1/2f_s$ s, giving a sampling rate f_{smp} of $2f_s$. It is standard practice to define the Nyquist frequency f_{Nq} to be the highest frequency Fourier component that can be accurately reconstructed with a given sampling rate. Thus, $f_{Nq} = \frac{1}{2} f_{smp}$. Damping of the sinusoid introduces Fourier components at frequencies higher than f_s, thereby increasing the necessary sampling rate.

The sampling theorem establishes a lower bound to f_{smp}, but does not address determination of an optimum sampling rate. Optimal sensitivity will be attained with strict application of the sampling theorem only in the hypothetical case of a noiseless signal sampled with infinite analog-to-digital converter (ADC) resolution. Sampling in excess of the required rate reduces the rms noise power associated with digitization (analogous to the use of several channels to record the same signal). Now consider noise at the input to the ADC accompanying FID signal components of frequency no greater than f_s. Stationary white noise consists of Fourier components that extend in frequency well beyond f_s. Noise components at frequencies beyond f_{Nq} will be folded into the spectrum (the phenomenon of *aliasing*), thereby increasing the noise power in the vicinity of the signal components. This will be the case, in practice, when the Nyquist frequency, established by the sampling rate, is lower than the IF frequency cutoff of the spectrometer detection system. Thus, if the IF bandwidth of the spectrometer is limited by the analog bandwidth f_{tr} of the transient recorders, then a Nyquist frequency $f_{Nq} = f_{tr}$ would give the optimum noise rejection. An alternative to adjustment of the sampling rate is limitation of the detector bandwidth. This is easily accomplished by placement of a low-pass filter at each IF output of the quadrature mixer.

Some digitizing oscilloscopes can interleave successive sweeps, thereby increasing the effective sampling rate. In the case of the HP scope used in our experiments, the technique of interleaving has been implemented in a manner that allows continuous variability of the effective dwell time over the range 10 ps to ~ 1 s. Interleaving of repetitive waveforms is performed at the cost of

reducing the *effective sweep rate* of the digitizers (i.e., the number of averages of the fully interleaved data per unit time). Unlike the case for NMR, where the experimental repetition rate is usually established by the nuclear T_1, the repetition rate for an ESR experiment is most often determined by the (real time) sweep rate of the transient recorders. Finally we note that, even if the sampling rate can be continuously varied, it is nevertheless advantageous to bandwidth limit the detector to maintain a high effective sweep rate.

The HP scope we have used provides a real time sampling rate of 40 megasamples/s (25-ns dwell time), which limits the accessible single-shot spectral bandwidth to 40 MHz (with quadrature detection). It is most often the case for ESR of nitroxides that spectral bandwidths exceed this limit. To achieve higher effective sampling rates the HP scope, as already noted, interleaves many successive sweeps to represent a single-shot waveform. The FIDs described in this chapter typically consist of Fourier components as high in frequency as $\pm$ 60 MHz, so that we typically use an effective dwell time of between 5 and 10 ns.

A transient recorder, which performs conversions at rates of 200 megasamples/s or greater, will adequately record such FIDs in a single sweep. Such digitizers have just become available from DSP Technology, but are untested as yet. Their Model 2102SA signal averager provides very high sweep rates (5000 sweeps/s), and may be used in pairs for recording the quadrature signals. The DSP transient recorder provides very good performance for dedicated data acquisition if one requires no more than $\pm$ 100 MHz bandwidth (for spectra $\sim$ 200 MHz in width). The HP scope has a much higher analog bandwidth (1 GHz), so that with its variable effective dwell time, it is a more flexible instrument suitable for a wider range of applications. Ideally, one should have several instruments, for example, DSP recorders for data conversion, and a 1-GHz sampling oscilloscope (such as the HP54100A) for test and measurement (e.g., of the mw pulse shapes) and for recording spectra exceeding 200 MHz bandwidth.

Free precession of the electron spin magnetization follows irradiation of the sample with a short 9.25-GHz mw pulse. The signal appears at the GaAsFET amplifier as an amplitude-modulated 9.25-GHz waveform. Down-conversion of the free precession signal yields time-varying voltages at the IF ports of the quadrature detector which are digitized by the sampling oscilloscope. Signal averaging is performed within the HP scope and the average FID is dumped directly to LSI11 memory via the GPIB and DMA interface. A 256-point/channel FID recorded with a dwell time of 5.0 ns, averaged 128 times (i.e., averaging of fully interleaved FIDs), can be recorded in 3.8 s from command line entry into the computer to storage of the data on the disk. This is more than sufficient signal averaging for collection of a spectrum such as that shown in Fig. 27. However, use of the DSP Model 2102SA would significantly reduce collection time or alternatively allow considerably greater (50–100) averages in the same time.

Two-dimensional spectroscopy requires that one apply several mw pulses and record the FID or ESE following the final pulse, during the detection period (cf.

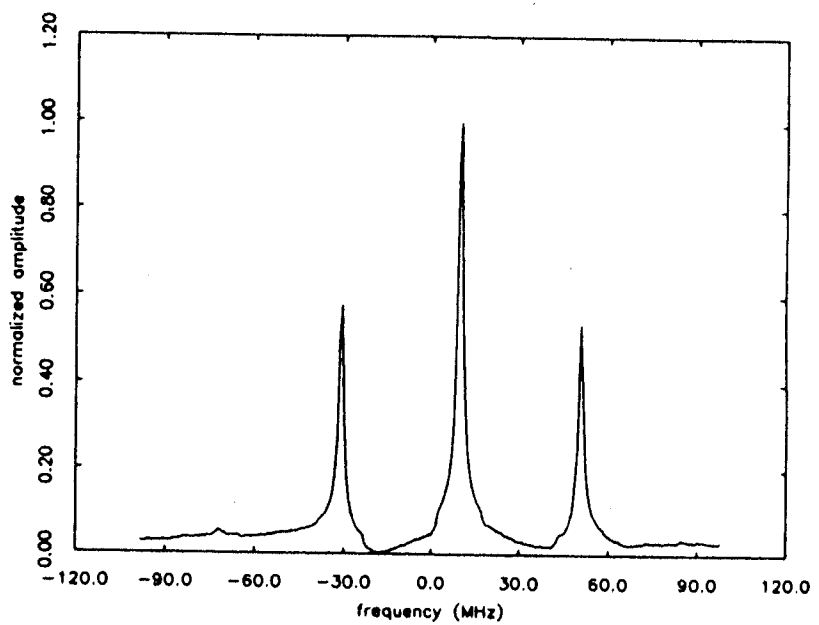

Fig. 27. Absolute value FT spectrum of 5.1×10^{-4} M PD-Tempone in toluene-d_8 at 21 °C, obtained from the average of 40 FIDs, each consisting of 256 complex data points extending to 1.2 μs; $t_p = 14$ ns corresponding to $B_1 \sim 6$ G. The data have not been amplitude corrected. From Ref. 43.

Fig. 17). The sampling theorem must again be employed in selecting an appropriate incremental t_1 (which is the time between the first and second mw pulses). It is desirable to have the same sampling rate in both t_1 and t_2 (cf. Fig. 17) so that the frequency resolution is the same (assuming the same zero-filled extension) in both dimensions of the 2D spectrum. Because of constraints on computer storage and data collection time, it is often preferable to use the maximum incremental t_1 consistent with the sampling theorem. CYCLOPS and other phase-alternation sequences are performed at each t_1 time step, with the appropriate linear combinations of FIDs computed at run time to minimize storage requirements. A typical 2D experiment involves sophisticated phase-alternation schemes (cf. Section 5), requiring the collection of about 3000 averaged FIDs, each consisting of 256 complex data words. This sequence of operations is controlled by the LSI11 minicomputer and currently requires 15–30 min per 2D spectrum. Details about the software may be found in Ref. 43.

7.2 Fourier Spectroscopy: Resonators

In the ideal single pulse experiment, a mw pulse of duration t_p rotates the equilibrium magnetization through an angle

$$\beta = \gamma_e B_1 t_p = \frac{\pi}{2} \tag{54}$$

about the direction of the applied field B_1, irrespective of the resonance offset. This is approximately the case when the resonance offset does not exceed the strength of the mw field, that is, when

$$|\omega_0 - \omega_{rf}| < |\gamma_e B_1| \tag{55}$$

and when $t_p \ll T_2$. The spectral bandwidth at X band is usually determined by the hf coupling and may be as large as 220 MHz (e.g., for very slow motional nitroxide spectra). The isotropic hf coupling in nitroxides is about 15 G, implying a total (motionally narrowed, isotropic) spectral bandwidth of about 90 MHz. Because of the large resonance offsets typically encountered in nitroxides, it is important to consider off-resonance effects. The magnetization is rotated about an effective B_1 that is tilted with respect to the z axis by an angle

$$\theta = \tan^{-1} \frac{B_1}{B_0 - \omega_{rf}/\gamma_e} \tag{56}$$

and has the amplitude

$$B_{eff} = \sqrt{B_1^2 + (B_0 - \omega_{rf}/\gamma_e)^2} \tag{57}$$

With a low Q cavity resonator, we find that we are limited in practice to a pulse width of no less than 14 ns because of insufficient transmitter power to satisfy Eq. 54 in the case of shorter t_p. (The choice of an optimum Q is discussed in the next section.) Although we can generate 5-ns mw pulses with 1.2-kW peak power, only small pulse rotations ($\beta < \pi/2$) may be achieved because of the inefficient conversion to incident power into B_1 at the sample in a cavity. A 14-ns pulse with $\beta = \pi/2$ on resonance and optimum Q corresponds to a B_1 of about 6 G, or uniform spectral rotation over a bandwidth of about 34 MHz ($2\gamma_e B_1$). It would seem that a 6-G B_1 would be insufficient for wideband excitation of nitroxides. Good results for motionally narrowed spectra can be obtained, because of the slow fall off of the amplitude response $(M_x^2 + M_y^2)^{1/2}$ as the resonance offset is increased beyond $\gamma_e B_1$ [38, 42]. The amplitude response predicted by Eqs. 56 and 57 falls off to 50% at an offset of about $2.7\gamma_e B_1$, implying a *half-amplitude response* bandwidth of $5.4\gamma_e B_1$, or about 90 MHz for a B_1 of 6 G. Amplitude and phase distortions that occur when the total spectral bandwidth exceeds $2\gamma_e B_1$ can be corrected numerically. Figure 27 illustrates a spectrum obtained from the FID; the same spectrum recorded by the slow-passage technique has three hf lines of nearly equal amplitude; each of the outer hf lines of the FT spectrum are reduced $\sim$ 50% in amplitude. Also, in general there are large phase corrections, which are discussed elsewhere [10, 43; see also Section A.2].

The conversion efficiency may be improved by confinement of the B_1 field [67] by means of a loop–gap resonator, which has been stabilized against electric breakdown [68–70]. We have found that the bridged loop–gap

resonator (BLGR) design by Pfenninger et al. [71] is appropriate for these purposes. We modified the construction [72], to provide the lower Q values and to permit easy adjustment of its resonant frequency and Q (in the range 20–100). We have obtained a B_{1max} of 14 G, which was uniform to within 20% over the length of the BLGR, with a matched Q_L of about 45. The predicted half-amplitude response is about 210 MHz. Such a combination of high B_1 and wide bandwidths yields nearly uniform excitation of isotropic motionally narrowed spectra such as PD-tempone in toluene-d_8 (cf. Fig. 28) or PD-tempone in the nematic phase V (cf. Fig. 29). It has also permitted us to obtain the FT of a slow-motional nitroxide (^{15}N) of $\sim$160 MHz spectral width from the echo decay, as well as the 2D-ELDOR from a model membrane sample [12].

7.3 Sensitivity versus Bandwidth

The sensitivity advantage of Fourier spectroscopy in comparison with slow-passage experiments in NMR is well documented [73, 74]. We illustrate the sensitivity of our spectrometer with the FID of Fig. 30 using a cavity resonator ($Q \sim 100$). Using a 6-bit, 1-gigasample/s digitizer, we recorded a single-shot FID of 5×10^{-4} M PD-tempone in toluene-d_8 with 2048 samples and a 1-ns

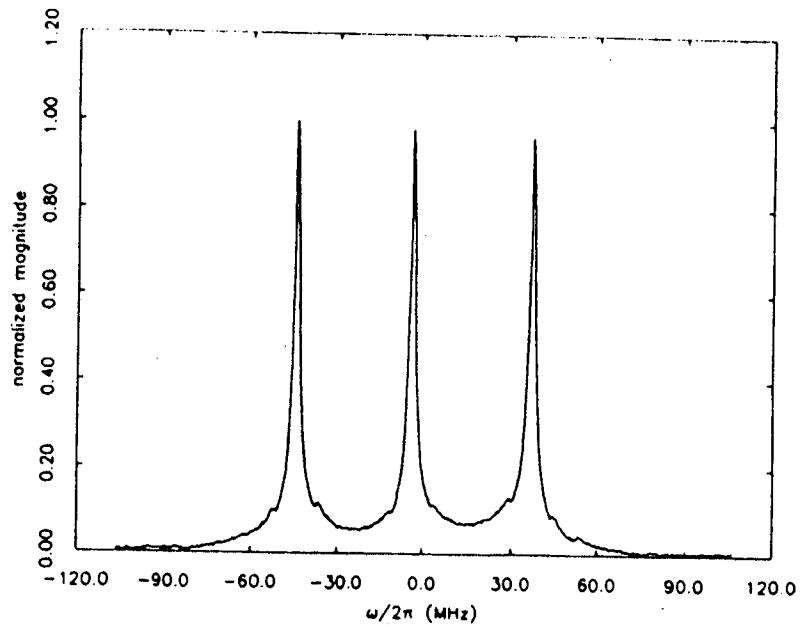

Fig. 28. FT spectrum of 5.0×10^{-4} M PD-Tempone in toluene-d_8 at 22 °C obtained with a bridged loop–gap resonator. $\pi/2$ pulse width was 6.7 ns, resolution in t_2 is 4.69 ns, 2048 averages, 256 complex data points zero-filled to 1024 prior to Fourier transformation. From Ref. 43.

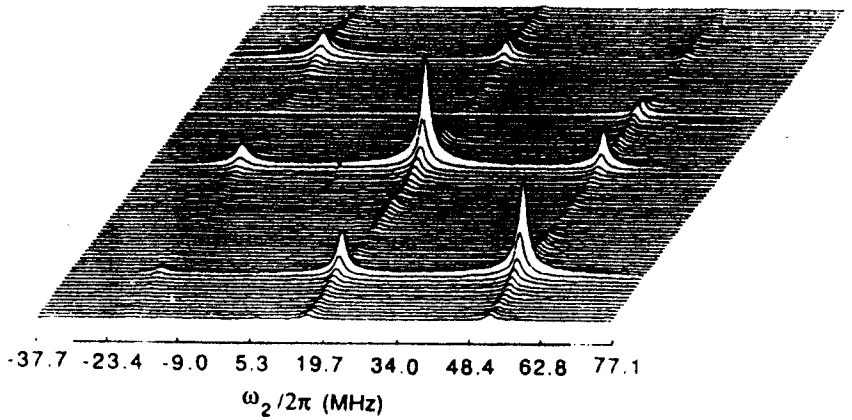

Fig. 29. Absolute value 2D ELDOR spectrum of 5.0×10^{-4} PD-Tempone in phase V at 24 °C obtained with a bridged loop–gap resonator; $\tau_p = 9.5$ ns; $\Delta t_1 = 7$ ns; $\Delta t_2 = 3.9$ ns; 8-step phase-alternation sequence; deadtime in t_2, 150 ns; deadtime in t_1, 100 ns; mixing time, $T = 6.0 \times 10^{-7}$ s; acquisition time, 49 min. From Ref. 43.

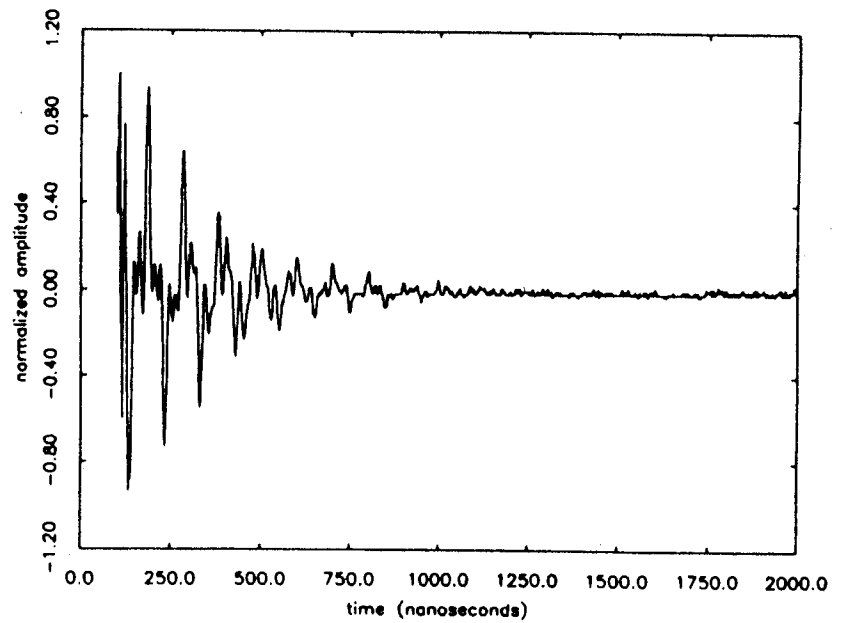

Fig. 30. Single-shot FID of 5.1×10^{-4} M PD-Tempone in toluene-d_8 at 21 °C; obtained with 1-ns time resolution with a deadtime of ~ 90 ns; $t_p = 12$ ns. The signal/noise ratio of this FID is found to be 86. From Ref. 8.

dwell time; the signal/noise ratio of this FID (i.e., the ratio of the maximum FID signal voltage to the rms noise voltage determined from the baseline) was found to be 86. The signal/noise ratio of the spectrum obtained upon FT of this FID was estimated to be 100, taking the height of the properly phased absorption line nearest resonance as the signal amplitude, and the rms value of the baseline as the noise amplitude [8]. We estimated that the FT spectrum after 30 s of signal averaging (with the HP54100 scope) has a $S/N \sim 4200$; this is to be compared with a $S/N \sim 400$ that we have obtained from the same sample solution by conventional cw methods with a 30-s scan time. Recent results with a BLGR ($Q \sim 40$) containing 19 μL of 5×10^{-4} M PD-Tempone in toluene-d_8 using our HP5400A digitizer yielded a $S/N \sim 1680$ with 30 s of signal averaging. This corresponds to a $S/N = 1$ for a total of 3.4×10^{12} spins after 30 s of signal averaging. The use of a pair of DSP Model 2102SA signal averagers can be expected to yield a $S/N = 1$ (30 s averaging time) for 2.4×10^{11} spins (or 2×10^{-8} M solution).

In comparing the sensitivity of Fourier spectroscopy with that of conventional slow passage techniques, the former is considered analogous to having a multichannel cw spectrometer. Each Fourier component of the mw pulse produces an impulse response determined by the value of the spectrum at its frequency [38]. The sensitivity advantage of Fourier spectroscopy is in a qualitative sense governed by the number of channels that simultaneously record a spectral component. We do not attempt to formulate a quantitative sensitivity comparison of the two techniques, since we are mainly concerned with methods of 2D ESR correlation spectroscopy. These require that coherence be simultaneously introduced to all spectral components. We briefly consider sensitivity as it pertains to experimental optimization in 2D ESR. Gorcester and Freed obtain for the sensitivity S, defined as the square root of the power signal/noise ratio per unit time,

$$S = \frac{M_0 E}{5p}\sqrt{\frac{2Mn\tau}{T_{rep}}}\sqrt{Q}\exp\left(-\frac{\tau_d}{T_2^*}\right) \tag{58}$$

In Eq. 58, E is again the spectrometer constant and M_0 is the equilibrium magnetization. We have assumed that M equidistant samplings have been made between 0 and τ, and n complex FIDs have been averaged. Also T_{rep} is the time between successive repetitions of the pulse sequence, and we assume that the rms noise voltage $V_n = p f_c^{1/2}$, where f_c is the frequency cutoff of the low-pass filter taken as the Nyquist frequency.

We now assume that a decay m (dB) typically of the order of 140 dB is needed to reduce the power level to that of noise [67]. The power in the resonator decays as $\exp(-\omega_{rf} t/Q)$, where the resonator is tuned to ω_{rf}. Thus, we obtain

$$\tau_d \simeq (m/10)\ln(Q/\omega_{rf}) \simeq 32\,Q/\omega_{rf} \tag{59}$$

For the case where resonator ring-down time dominates τ_d, substituting for τ_d in Eq. 58 and optimizing with respect to Q gives the expression

$$Q_{opt} = \omega_{rf} T_2^*/64 \tag{60}$$

It follows from Eq. 59 that at Q_{opt}, $\tau \simeq T_2^*/2$ (independent of m). Hence, for a resonance line of $T_2^* = 100$ ns, with $\nu = 10$ GHz, we expect optimal sensitivity in the FID experiment with $Q = 100$ and $\tau_d \simeq 50$ ns. (For the echo we have $S \propto Q^{1/2}\exp(-2\tau_d/T_2)$ consistent with $Q_{opt} = \omega_{rf} T_2/128$, or $Q_{opt} = 50$ and $\tau_d \simeq 25$ ns for $T_2 = 100$ ns and $\nu = 10$ GHz.) If the spectrum consists of more than one resonance line we impose the additional constraint that the resonator half-power bandwidth be at least as large as the spectral bandwidth. (The signal voltage at the detector associated with an FID Fourier component of frequency ω (call it $V_s(\omega)$) is reduced by a factor of $1/\sqrt{2}$ for ω equal to a frequency for which the resonator is at half-power: $\omega_{rf} \pm \omega_{rf}/2Q$; i.e., $V_s(\omega_{rf} \pm \omega_{rf}/2Q) = V_s(\omega_{rf})/\sqrt{2}$.) Hence for the case of a motionally narrowed nitroxide spectrum of full width 100 MHz, with $T_2^* = 200$ ns (for each hf line) and $\nu = 10$ GHz, we must reduce the Q from $Q_{opt} = 200$ to a Q of 100 to ensure adequate sensitivity to off-resonance spectral components.

Implementation of these concepts requires that Q, B_1, and hence transmitter power be continuously variable over a range that is not always experimentally feasible. To maintain a constant B_1 at the sample, halving the Q requires an associated doubling of the power to the resonator, a step that is ultimately limited by saturation of the mw transmitter amplifier. The transmitter power and resonator Q needed to achieve coverage of a spectrum of given bandwidth can be deduced from steady-state arguments from the expression

$$P_0 = \mu_0 V_c B_1^2 \nu/2Q \tag{61}$$

relating B_1 at the sample to mw power P_0 dissipated by the resonator. In Eq. 61 ν is the resonator frequency and V_c is the effective cavity volume [67, 75]. P_0 is equal to the mw power incident on the resonator if the resonator is matched. The half-power full bandwidth of the resonator is given approximately by ν/Q, while the half-amplitude response bandwidth is estimated by $\Delta\nu \sim 5.4\gamma_e B_1/2\pi$. Thus, we see from this and Eq. 61 that the required transmitter power is cubic in the desired bandwidth. Fixing the available transmitter power, we achieve optimal spectrometer performance by adjusting t_p and Q until the half-power resonator bandwidth is equal to the half-amplitude response bandwidth. However, for the low Q cavity resonator, this corresponds to the maximum B_1 of 6 G ($t_p = 14$ ns) and a Q of 100 when operating with the maximum available transmitter power of 1.2 kW (cf. Section 7.2). To double the spectrometer bandwidth we would need an increase in transmitter power by a factor of 8. Alternatively, we can decrease the effective cavity volume by the same factor, which is easily accomplished with the BLGR as described above.

7.4 Composite Pulses

It is possible to shape pulses to produce more uniform coverage across the spectrum than simple rectangular pulses. Pulse shaping, particularly composite

pulses, is well known in NMR [76]. Composite pulse technology is much more challenging for ESR, requiring microwave (rather than rf) technology, and the elementary pulses in a composite pulse, which must be very accurate, are on the nanosecond timescale. Furthermore, the short FID T_2^*'s (and T_2's) limit the length of time available for a composite pulse made up of many elementary pulses.

To select pulse shapes that would meet the constraints of pulsed-ESR technology, Crepeau et al. [72] first considered the problem theoretically, by numerically solving the standard Bloch equations in the presence of an irradiating field either with T_1 and T_2 relaxation present or else absent for simplicity. The rotating field $B_1(t)$ was allowed to have an arbitrary time dependence both in amplitude $|B_1(t)|$ and in phase, and account was taken of the filtering effect of the finite Q_L of the resonator by convoluting $B_1(t)$ with the function $\exp(-\omega t/2Q_L)$. The resulting Bloch equations with time-varying irradiation were integrated numerically at each frequency offset. An efficient algorithm [77] allowed the introduction of a nonlinear constrained optimization scheme [78] to optimize the pulse shape. The principal constraint is in the maximum amplitude B_{1max} of the available magnetic field $|B_1(t)|$.

Composite pulses produced from a sequence of elementary square pulses (with correction for finite Q_L) of the same amplitude, B_{1max}, were primarily considered. Each elementary pulse varies only in its phase, either 0° or 180°, and its duration. Simple composite pulses of this type can be realized experimentally with current ESR technology. A maximum of $n = 5$ elementary pulses was considered, since that corresponded to the current experimental limit. Such a procedure did uncover composite pulses with significantly extended coverage.

The 2D FT-ESR spectrometer of Fig. 24 was modified to permit composite pulsing. This required the installation of a microwave circuit enabling rapid phase shifting by 180° within a single overall pulse. The composite pulse generation hardware, shown in Fig. 31*a* was installed between the microwave klystron and the phase shifter (shown in Fig. 24). The klystron signal is first routed, by means of a three-port circulator, to a fast ECL driven switch. This switch either passes the cw signal to a continuously adjustable phase shifter followed by the 0° port of a combiner, or reflects it back through the circulator to a second path through a variable attenuator to the 90° port of the combiner. With proper adjustment of the attenuator and phase shifter, the signals from the two paths differ by only a 180° phase shift after recombination.

The ECL control for the switch was provided by combining the pulse outputs from a four-channel digital delay generator. The leading edges of each of the four pulse outputs can signal a 180° phase shift, and the existing logic and switching capability of the spectrometer provide for the rising and falling edges of the composite pulse. Thus, this combination could provide a pulse of $n \leq 5$. The switch transition time is about 1–2 ns, and the delay adjustment can be made in 10-ps steps. It is possible to carefully examine the detailed shape of the composite pulses to better than 100-ps time resolution by utilizing the HP54100A as a sampling oscilloscope and by sending the composite pulse

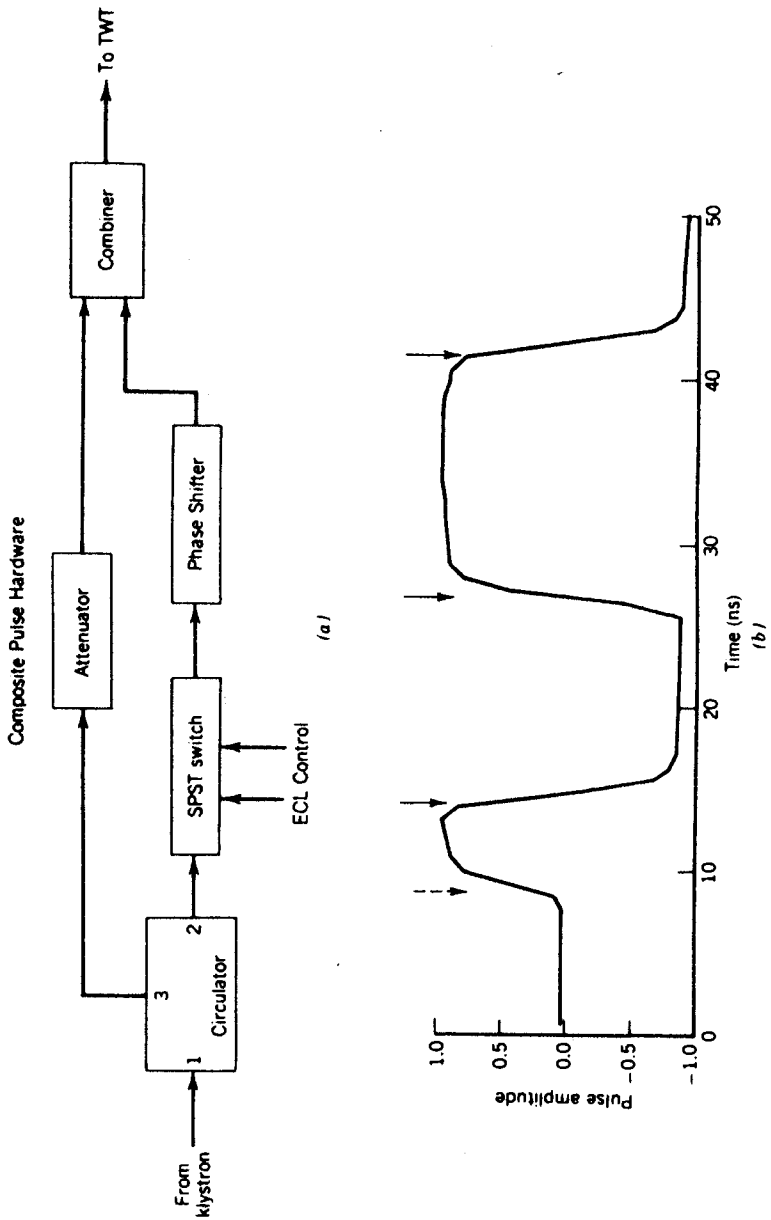

Fig. 31. (*a*) Layout of the hardware used to produce the composite pulses. The reflective microwave switch was from New England Microwave, and the required complementary ECL logic inputs were obtained from a Precision Instruments, Inc. four-channel digital delay generator. (*b*) Phase-sensitive detection of a typical composite pulse supplied to the input to the TWT. The vertical solid arrows indicate 180° phase shifts; the vertical dashed arrow represents the turning on of the microwave power. From Ref. 72.

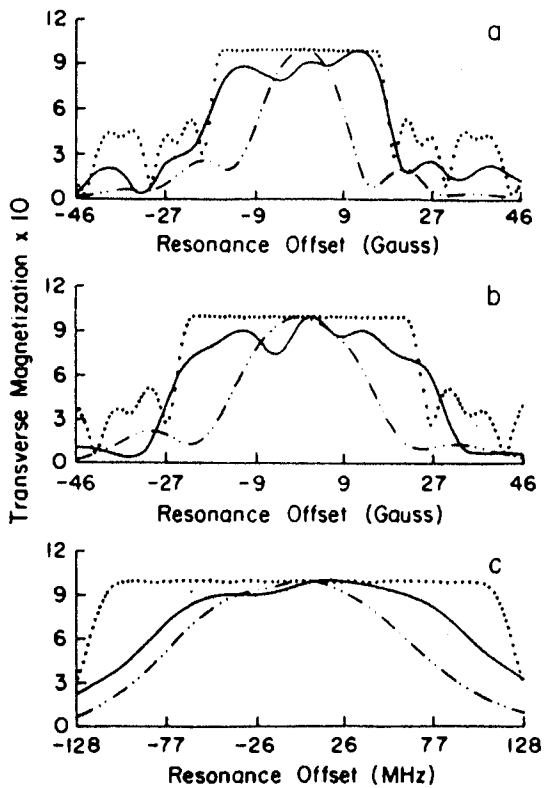

Fig. 32. A comparison of the extent of magnetization rotated into the xy plane (i.e., $M_{xy} \equiv |M_x^2 + M_y^2|^{1/2}$) by a simulated composite $\pi/2$ pulse ($\cdots$), experimentally generated composite pulse (——), and an experimental single-component pulse (– · · –) at different B_1 levels. (*a*) B_1 of 4.23 G: experimental composite pulse (30 ns, $\overline{15}$ ns, 12 ns, $\overline{6}$ ns), simulated composite pulse (29.3 ns, $\overline{15.2}$ ns, 12.5 ns, $\overline{7.8}$ ns), single-component $\pi/2$ pulse (27 ns). (*b*) B_1 of 6.0 G: experimental (19 ns, $\bar{9}$ ns, 8 ns, $\bar{4}$ ns), simulated (21.0 ns, $\overline{11.0}$ ns, 9.2 ns, $\overline{6.2}$ ns), single-component (19 ns). (*c*) B_1 of 11.0 G: experimental (9 ns, 5 ns, 4 ns, $\bar{3}$ ns), simulated (11.8 ns, $\overline{6.2}$ ns, 5.4 ns, $\overline{4.4}$ ns), single-component (9.4 ns). The component widths are given in the order in which they are applied to the BLGR, and an overbar indicates a 180° phase shift. The B_1 values are estimated from the pulse durations required to rotate the spins on resonance by $\pi/2$. Note that the experimental results (but not the simulated ones) show the effects of the finite Q on the signal *from* the BLGR. The abscissa is scaled equally for all three plots and labeled in gauss or megahertz for comparison. From Ref. 72.

directly to the quadrature mixer. A typical observation is shown in Fig. 31*b* for the in-phase arm (with the reference phase of the quadrature mixer appropriately adjusted to optimize this arm). The clean transitions (seen in Fig. 31*b*) when the microwave signal is turned on, and when the phase is shifted by 180°, are consistent with the specifications of the component and there is very little phase noise or ringing either in the input to or output from the high-power TWT. Also, the BLGR described above was utilized.

We show in Fig. 32 results for three different composite pulses of $n = 4$, each with different B_1 and optimized to maximize the rotation of spins into the xy plane across a $\pm 2.8B_1$ spectrum. In each case the computed composite pulse shows significantly improved spectral coverage as compared to a single experimental $\pi/2$ pulse. Also, in each case, the experimental result from the $n = 4$ composite pulse shows a clear improvement over the experimental single-pulse result. In general, however, the relative effectiveness of the composite pulse is less than the greater the value of B_1. This is largely due to the Q of the BLGR with its halfpower *halfwidth* of 100 MHz. The theoretical computations do not include the effect of the finite Q on the signal *from* the resonator (just the effect on the pulse shape into the resonator), and hence will show what appears to be greater coverage. The finite (1ns) switching times of the ECL driven switch may also contribute, as well as the (small) $B_{1\max}$ variation in the BLGR.

One should note that it would be difficult to produce high-power pulses of varying amplitude. It is not difficult to vary the amplitude of the microwave signal to the TWT pulse amplifier, but this amplifier is usually operated at saturation (to minimize amplitude noise) and is thus rather insensitive to amplitude variations in the input microwave signal.

Thus, we see that one can now provide effective (though nonuniform) coverage over at least a 200-MHz spectrum. Considerable further improvement in coverage may be expected from these simple phase-alternating composite pulses based upon the theoretical predictions with careful choice of resonator Q and (perhaps) improved switching times.

APPENDIX: LPSVD IN ONE AND TWO DIMENSIONS

Linear prediction based on singular value decomposition (LPSVD) was developed by Kumaresan and Tufts [44] and introduced to magnetic resonance by Barkhuijsen et al. [45]. In that initial application to magnetic resonance, the emphasis was on obtaining good frequency information in one-dimensional data. Millhauser and Freed [9] demonstrated the application of these essentially one-dimensional methods to two-dimensional electron spin-echo (2D ESE) spectroscopy as discussed in Sections 3 and 4. That is, real valued linear prediction was applied to the ESE envelope at each field position in the 2D ESE spectrum. Here, we give a brief overview of the Kumaresan–Tufts method (but, for a more comprehensive description, see Refs. 44 and 45). We then discuss the combined use of complex valued linear prediction and Fourier transformation

in both axes of a 2D ELDOR spectrum, which may be used to project 2D absorption line shapes as well as to reject residual axis peaks and much of the noise (cf. Ref. 10 and Section 5). We then describe a new linear predictive approach, based on LPSVD, which treats two-dimensional time series obtained in COSY-type experiments entirely in the time domain, that is, without Fourier transformation [10, 43].

A.1 LPSVD in One Dimension

The basis for (autoregressive) linear prediction is that a discrete time series

$$\{x_1, x_2, \ldots, x_N\} \tag{62}$$

can be modeled by the expression

$$x_n = \sum_{i=1}^{M} b_i x_{n-i} \tag{63}$$

where the set $\{b_i\}$ are the forward linear prediction (l.p.) coefficients, and the prediction order M is less than N. The implication of Eq. 63 is that each sampling of the time series can be expressed as a linear combination of the M previous ones. With the application of backward l.p., described by writing Eq. 63 in the reverse sense, that is,

$$x_n = \sum_{i=1}^{M} a_i x_{n+i} \tag{64}$$

one can model an FID in terms of exponentially damped sinusoids and determine all of the relevant parameters: frequency, time constant, amplitude, and phase [79].

In the LPSVD procedure one first generates a set of coupled equations obtained on writing Eq. 64 for the $N - M$ possible values of n. The least-squares solution for the set of l.p. coefficients, in terms of the N complex data points is written as

$$\begin{bmatrix} x_2 & x_3 & \cdots & x_{M+1} \\ x_3 & x_4 & \cdots & x_{M+2} \\ \vdots & \vdots & & \vdots \\ x_{N-M+1} & x_{N-M+2} & \cdots & x_N \end{bmatrix} \begin{bmatrix} a_1 \\ a_2 \\ \vdots \\ a_M \end{bmatrix} = \begin{bmatrix} x_1 \\ x_2 \\ \vdots \\ x_{N-M} \end{bmatrix} \tag{65}$$

or equivalently

$$\mathbf{X}_a = y \tag{66}$$

The rank deficient least-squares problem is solved by computing the singular value decomposition of the Hankel data matrix $\mathbf{X} \in C^{N-M \times M}$, that is,

$$\mathbf{X} = \mathbf{U}\Sigma\mathbf{V}^{\dagger} \tag{67}$$

where $\mathbf{U} \in \mathbf{C}^{(N-M)\times(N-M)}$ and $\mathbf{V} \in \mathbf{C}^{M\times M}$ are the (unitary) matrices of left and right singular vectors, and $\Sigma \in \mathbf{R}^{N-M\times M}$ is defined by

$$\Sigma = \mathrm{diag}(\sigma_1 > \sigma_2 > \cdots > \sigma_M) \tag{68}$$

where the σ_i are the (real positive) singular values of X. Noise rejection is achieved by subtraction of the root-mean-square of the singular values attributed to noise from the K singular values associated with signal. (It can be shown that for a noiseless signal comprised of L exponentially damped sinusoids, $2L$ singular values are nonzero [45].) An estimate of K is obtained by plotting the singular values in descending order; then a distinction between signal-related and noise-related singular values can be made [45] provided the signal/noise ratio is not too small. The $M - K$ noisy singular values are zeroed to obtain

$$\tilde{\Sigma} = \mathrm{diag}(\sigma_1, \sigma_2, \ldots, \sigma_K, 0, \ldots, 0) \tag{69}$$

and the rank K approximation $\tilde{\mathbf{X}}$ to the data matrix X is obtained from

$$\tilde{\mathbf{X}} = \mathbf{U}\tilde{\Sigma}\mathbf{V}^{\dagger} \tag{70}$$

The M l.p. coefficients are then obtained from the minimum 2-norm least-squares solution of Eq. 65; that is,

$$a = \mathbf{V}\tilde{\Sigma}^{-1}\mathbf{U}^{\dagger}y \tag{71}$$

The frequencies and widths are obtained upon determination of the M complex roots of the characteristic polynomial equation

$$z^M - \sum_{m=1}^{M} a_m z^{M-m} = 0 \tag{72}$$

retaining only those ℓ roots of magnitude greater than one. From these ℓ remaining roots, $L = \ell/2$ exponentially damped sinusoids are obtained.

There are two parameters that must be selected to model the FID: (1) the number of l.p. coefficients (i.e., the prediction order M) and (2) the number K of singular values attributable to signal (i.e., the effective rank). Linear prediction yields the frequencies and widths, after which a second least-squares (LS) procedure is used to obtain amplitudes and phases. Once the frequency, width, amplitude, and phase of each FID component are known, reconstruction of the FID may be obtained from the expression

$$x'_n \equiv x'(n\Delta t) = \sum_{j=1}^{L} c_j \exp\left(-\frac{n\Delta t}{T_{2j}}\right)\cos(\omega_j n\Delta t + \phi_j) \tag{73}$$

for one quadrature component, and an analogous expression for the other quadrature component. This type of linear prediction analysis (but without quadrature detection), was applied to 2D ESE yielding results shown in Fig. 7. These experiments [9] have 100 time series (each one a 50 point echo decay envelope) taken at a different magnetic field location. Up to 16 l.p. coefficients were used, attributing up to 12 of the singular values to signal, and repeating the treatment for all of the 100 decay envelopes. In regions where there was resolvable signal, l.p. typically recovered between one and eight sinusoid components. However, upon examination we found that there were rarely more than three components of significant amplitude.

A.2 LPSVD and FT Spectra

In FT-ESR, with quadrature detection the phases ϕ_j may vary substantially across the spectrum due to the finite dead time so that the spectrum obtained upon FT of the reconstructed FID described by Eq. 73 is an admixture of absorption and dispersion. To remedy this problem we zero the L phases in Eq. 74, $\{\phi_j, j = 1, L\}$, prior to reconstruction of the FID, so that upon FT of the LPSVD result the pure absorption line shapes are obtained [10]. The LPSVD procedure is easily generalized to *two* frequency dimensions by applying complex LPSVD to each FID prior to FT with respect to t_2 (cf. Eq. 28 or 29) collecting the results of the FT as described by Eq. 36, then applying complex LPSVD once again in the t_1 domain [10]. If the phases ϕ_j are zeroed at each call to LPSVD, the pure absorption representation of the 2D spectrum is retrieved. This is the approach utilized to obtain Fig. 20.

A.3 2D LPSVD for COSY-type Experiments

In the above approach, linear prediction was applied to 2D data simply by applying LPSVD to the constituent 1D spectra in both t_1 and t_2 time domains. We now present a substantially different approach, which can truly be considered 2D linear prediction, because it exploits all of the symmetries of 2D COSY-type spectra and yields all of the 2D spectral information while performing the analysis entirely in the time domain, that is, without any Fourier transformation [10, 43]. The procedure, which we refer to as 2D LPSVD, is carried out as follows. (1) Calculate the M l.p. coefficients in Eq. 65 with the FID obtained at the initial t_1 (for convenience) and determine the frequencies and widths. (2) Recognizing that the frequencies and widths are the same for *all* of the FIDs irrespective of t_1, perform just the linear LS procedure on each FID to just determine the amplitudes and phases at each t_1 (and for the quadrature components in t_1 (cf. Eq. 36). In the procedure, one utilizes the frequencies and widths obtained in step 1. We now define a time series by the expression

$$x'_{nm} \equiv x(n\Delta t_1, m\Delta t_2) = \sum_{j=1}^{L} c_j(n\Delta t_1)\exp\left(-\frac{m\Delta t_2}{T_{2j}}\right)\cos(\omega_{2j} m\Delta t_2 + \phi_{2j}) \tag{74}$$

which reflects the dependence upon t_1 of the complex valued amplitudes c_j, determined in step 2. (3) Now recognize that the $c_j(n\Delta t_1)$ in Eq. 74 are themselves time series of the same form as $x'(n\Delta t)$ in Eq. 73 (cf. Eq. 28 or 30), and therefore perform LPSVD on the $c_j(n\Delta t_1)$ for every component j (corresponding to the different frequency components in the ω_2 frequency domain). Finally, (4) reconstruct the 2D time-domain data with the expression

$$x_{nm} \equiv x(n\Delta t_1, m\Delta t_2) = \sum_{j=1}^{L_2} \sum_{i=1}^{L_1(j)} c_{ij} \exp\left(-\frac{n\Delta t_1}{T_{2,1i}}\right) \cos(\omega_{1i} n t_1 + \phi_{1i}) \times \exp\left(-\frac{m\Delta t_2}{T_{2,2j}}\right) \cos(\omega_{2j} m\Delta t_2 + \phi_{2j}) \quad (75)$$

which is the 2D LPSVD analog of Eq. 73, where c_{ij}, $T_{2,1i}$, $T_{2,2j}$, ω_{1i}, ϕ_{1i}, and ϕ_{2j} are the spectral parameters returned by 2D LPSVD, L_2 is the number of sinusoids obtained in t_2, and $L_1(j)$ is the number of sinusoids obtained in t_1 for the jth spectral component in t_2. Equation 75 represents one quadrant of the 2D quadrature data, and analogous expressions may be written for the other three quadrants. Note that the amplitudes c_{ij} of these time-domain correlations are just the volume integrals that would be obtained upon 2D (quadrature) Fourier transformation of Eq. 75 followed by integration. Thus, one need not actually construct the 2D time series according to Eq. 75, as suggested in step 4, to obtain volumes of 2D spectral lines. A table of 2D spectral parameters contains all of the relevant information (i.e., frequencies, widths, and volume integrals). Note also that one need not necessarily perform more than a single SVD. Once the frequencies and T_2's are established in step 1, they could be applied in step 3 in the same fashion as in step 2; that is, the linear LS problem for the time series $c_j(n\Delta t_1)$ would be solved using the set of frequencies and T_2's obtained in step 1. We have chosen to perform the SVD at each component j in t_1 because of the generally poor signal/noise ratio in that time domain, requiring somewhat more careful application of the methods outlined above for 1D LPSVD.

The results of 2D LPSVD, applied to a spectrum of PD-tempone in *S2* are tabulated in Table 4. 2D LPSVD accurately located all of the observed spectral features, namely, three auto-peaks (identified by [c]) and four cross-peaks (identified by [b]). In addition there are other components in Table 4 that warrant careful examination. These components may be identified as originating from one of two sources: (1) broad baseline distortions, characterized by short T_2; and (2) axial peaks, characterized by their proximity to the ω_1 origin. These components are not artifacts of the LPSVD; they are present in the 2D FT spectrum. In some cases these features are not adequately represented as single exponentially damped sinusoids, and one obtains only their approximate amplitude and location. The example given in Table 4 is *not* representative of one of the better 2D LPSVD results. Typically, one finds a substantially "cleaner" table of spectral parameters, that is, one consisting of auto-peaks, cross-peaks, and a few axial peaks. This example was chosen

TABLE 4. Spectral Components for 2.05×10^{-3} M PD-Tempone in Liquid-Crystal Solvent S2 obtained by 2D LPSVD[a]

Amplitude	$\omega_2/2\pi$ (MHz)	$\omega_1/2\pi$ (MHz)	$T_{2,2}$ (ns)	$T_{2,1}$ (ns)
0.1268	− 3.292	− 0.8372	86.2	3066
0.0524	− 3.292	11.264	86.2	349 6
0.0259	− 3.292	50.163	86.2	1494.8
0.0277	− 3.292	− 36.371	86.2	1241
0.0217	25.579	3.956	303.2	1328
0.1196[b]	25.579	− 10.862	303.2	250.2
0.0201	25.579	− 3.928	303.2	1926.
0.3381[c]	25.579	25.302	303.2	320.9
0.1325	− 9.749	− 9.356	87.6	807.7
0.1131	− 9.749	− 11.091	87.59	1005
0.1699[b]	− 10.740	− 47.283	284.5	124.8
0.4776	− 10.740	0.5046	284.5	477.2
1.000[c]	− 10.740	− 10.935	284.5	326.5
0.0809[b]	− 10.740	25.260	284.5	203.2
0.2997	− 10.740	− 0.5289	284.5	1169
0.1157[b]	− 47.055	− 10.842	196.9	293.5
0.0308	− 47.055	1.639	196.9	1208
0.5532[c]	− 47.055	− 47.212	196.8	182.2
0.7644	− 47.055	− 1.476	196.8	442.4
0.3106	− 0.0912	− 0.504	420.5	1379

[a] Here $N = 256$, $M = 150$, and $K = 10$ in t_2; $N = 128$, $M = 96$, and $K = 10$ in t_1, $T = 495$ ns; $\Delta t_2 = 5.86$ ns; $\Delta t_1 = 7$ ns; temperature = 42.61 °C; $\angle(\mathbf{n}, \mathbf{B}_0) = 8.44°$ ($\mathbf{n}$ is the nematic director).
[b] Cross-peak.
[c] Auto-peak.

intentionally to demonstrate the kinds of components obtained by 2D LPSVD that may be misconstrued as artifacts. It should also be noted that the presence of some or all of these components may be influenced by the chosen effective rank K (i.e., the number of singular values attributed to signal) in the t_1 and t_2 time domains. However, it is not always advisable to reduce K to eliminate these components, since this will usually negatively influence the ability of LPSVD to accurately represent the more relevant signal components.

With a vectorized version of the 2D LPSVD algorithm on a Convex C1 superminicomputer, the calculation of Table 4 required 108 s. Because of the speed of this calculation, we find it feasible to adopt the criterion of Kumarasen-Tufts that the prediction order M should be three-fourths the number of data points; that is, $M = 0.75N$. In fact we consistently use this criterion in the t_1 domain, because of the small signal/noise ratio. In the t_2 domain a smaller prediction order is permissible because of the superior signal/noise ratio.

Many possibilities exist for further improvement of computational efficiency of the methods presented in this section. The SVD algorithm is certainly the most stable method of solving the rank-deficient least-squares problem of Eq. 65, but it is also the most computationally inefficient. An alternative approach is to solve for the eigenvalues of the matrix $\mathbf{X}^\dagger\mathbf{X}$, which are simply related to the singular values of $\mathbf{X}$ [80]. This method is computationally more efficient than SVD, but may become unstable in the case of a large prediction order M (the condition number increases with M). Barkhuijsen et al. have nevertheless found this technique to be generally successful in LPSVD applications [45, 81]. Related computational methods for the solution of Eq. 65 and variations on the linear prediction theme have been demonstrated by Tang et al. [82]. We have found to be useful an iterative Lanczos method for singular value decomposition, which very rapidly and accurately predicts the large singular values and which exploits the Hankel structure of $\mathbf{X}$ [83].

ACKNOWLEDGMENTS

We thank David Budil and Betsey Van Sickle for assistance with the final manuscript. This research was supported by NSF Grants CHE87-03014 and DMR 8901718, NIH Grant GM25862, and the Cornell Materials Science Center.

REFERENCES

1. J. H. Freed, in *Time Domain Electron Spin Resonance* (L. Kevan and R. N. Schwartz, eds.), Chapter 2. Wiley (Interscience), New York, 1979.
2. A. E. Stillman and R. N. Schwartz, in *Time Domain Electron Spin Resonance* (L. Kevan and R. N. Schwartz, eds.), Chapter 5. Wiley (Interscience), New York, 1979.
3. G. L. Millhauser and J. H. Freed, *J. Chem. Phys.* **81**, 37–48 (1984).
4. M. Dorio and J. H. Freed, eds., *Multiple Electron Resonance Spectroscopy*. Plenum, New York, 1979.
5. J. P. Hornak and J. H. Freed, *Chem. Phys. Lett.* **101**, 115–119 (1983).
6. S. A. Dzuba, A. G. Maryasov, K. M. Salikhov, and Yu. D. Tsvetkov, *J. Magn. Reson.* **58**, 95–117 (1984).
7. J. Gorcester and J. H. Freed, *J. Chem. Phys.* **85**, 5375–5377 (1986).
8. J. Gorcester and J. H. Freed, *J. Chem. Phys.* **88**, 4678–4693 (1988).
9. G. L. Millhauser and J. H. Freed, *J. Chem. Phys.* **85**, 63–67 (1986).
10. J. Gorcester and J. H. Freed, *J. Magn. Reson.* **78**, 291–301 (1988).
11. G. L. Millhauser, J. Gorcester, and J. H. Freed, in *Electronic Magnetic Resonance of the Solid State* (J. A. Weil, M. K. Bowman, J. R. Morton, and K. F. Preston, eds.), pp. 571–597. *Can. Soc. Chem.*, Ottawa, 1987.
12. J. Gorcester, G. L. Millhauser, and J. H. Freed, in *Advanced EPR: Applications in Biology and Biochemistry* (A. Hoff, ed.), Chapter 5. Elsevier, Amsterdam, 1989.

13. J. H. Freed, in *Rotational Dynamics of Small and Macromolecules in Liquids* (T. Dorfmüller and R. Pecora, eds.), pp. 89–142. Springer-Verlag, New York, 1987.
14. D. J. Schneider and J. H. Freed, *Adv. Chem. Phys.* **73**, 387–527.
15. D. J. Schneider and J. H. Freed, *Biol. Magn. Reson.* **8**, 1–76 (1989).
16. L. Kevan and R. N. Schwartz, eds., *Time Domain Electron Spin Resonance*. Wiley (Interscience), New York, 1979.
17. K. M. Salikhov, A. G. Sevenov, and Yu. D. Tsvetkov *Electron Spin Echoes and Their Applications*. Nauka, Novosibirsk, 1976.
18. W. B. Mims and J. Peisach, *Biol. Magn. Reson.* **3**, 213–263 (1981).
19. J. R. Norris, M. C. Thurnauer, and M. K. Bowman, *Adv. Biol. Med. Phys.* **17**, 365–415 (1980).
20. A. E. Stillman and R. N. Schwartz, *J. Phys. Chem.* **85**, 3031–3040 (1981).
21. A. E. Stillman, L. J. Schwartz, and J. H. Freed, *J. Chem. Phys.* **73**, 3502–3503 (1980).
22. L. J. Schwartz, A. E. Stillman, and J. H. Freed, *J. Chem. Phys.* **77**, 5410–5425 (1982).
23. L. J. Schwartz, Ph.D. Thesis, Cornell University, Ithaca, NY (1984).
24. U. Eliav and J. H. Freed, *Rev. Sci. Instrum.* **54**, 1416–1417 (1983).
25. V. F. Yudanov, S. A. Dikanov, Yu. A. Grishin, and Yu. D. Tsvetkov, *J. Struct. Chem.* **17**, 387–392 (1976); A. A. Shubin and S. A. Dikanov, *J. Magn. Reson.* **52**, 1–12 (1983).
26. L. J. Kar, G. L. Millhauser, and J. H. Freed, *J. Phys. Chem.* **88**, 3951–3956 (1984).
27. G. L. Millhauser, D. S. Clark, and J. H. Freed, unpublished; G. A. Marg, G. L. Millhauser, P. S. Skerkev, and D. S. Clark, *Ann. N.Y. Acad. Sci.* **469**, 253–258 (1986).
28. L. Kar, M. E. Johnson, and M. K. Bowman, *J. Magn. Reson.* **75**, 397–413 (1987).
29. J. S. Hyde and L. R. Dalton, in *Spin Labeling: Theory and Applications* (L. J. Berliner, ed.), Vol. 2, Chapter 1. Academic Press, New York, 1979.
30. L. J. Schwartz, G. L. Millhauser, and J. H. Freed, *Chem. Phys. Lett.* **127**, 60–66 (1986).
31. J. H. Freed, *J. Phys. Chem.* **78**, 1155–1167 (1974).
32. M. Nechtschein and J. S. Hyde, *Phys. Rev. Lett.* **24**, 672–674 (1970).
33. G. V. Bruno and J. H. Freed, *Chem. Phys. Lett.* **25**, 328–332 (1974); G. V. Bruno, Ph.D. Thesis, Cornell University, Ithaca, NY (1972).
34. J. S. Hyde, M. D. Smigel, L. R. Dalton, and L. A. Dalton, *J. Chem. Phys.* **62**, 1655–1667 (1975); L. R. Dalton, B. H. Robinson, L. A. Dalton, and P. Coffey, *Adv. Magn. Reson.* **8**, 149–259 (1976); L. A. Dalton and L. R. Dalton, in *Multiple Electron Resonance Spectroscopy* (M. Dorio and J. H. Freed, eds.), Chapter 5. Plenum, New York, 1979.
35. J. S. Hyde, W. Froncisz, and C. Mottley, *Chem. Phys. Lett.* **110**, 621–625 (1984).
36. J. Jeener, *Magn. Reson. Chem. Biol., Lect. Ampère Int. Summer Sch., 1971* (1975).
37. W. P. Aue, E. Bartholdi, and R. R. Ernst, *J. Chem. Phys.* **64**, 2229–2246 (1976).
38. R. R. Ernst, G. Bodenhausen, and A. Wokaun, *Principles of Nuclear Magnetic Resonance in One and Two Dimensions*. Oxford Univ. Press, New York, 1987.
39. M. Bowman, *Bull. Am. Phys. Soc.*, [2] **31**, 524 (1986).
40. R. J. Massoth, Ph.D. Thesis, University of Kansas, Lawrence (1987).
41. J. Gorcester, G. L. Millhauser, and J. H. Freed, *Magn. Reson. Relat. Phenom., Proc. Congr. Ampère, 23rd, 1986*, pp. 562–563 (1986).
42. J. P. Hornak and J. H. Freed, *J. Magn. Reson.* **67**, 501–518 (1986).

43. J. Gorcester, Ph.D. Thesis, Cornell University, Ithaca, NY (1989).
44. R. Kumaresan and D. W. Tufts, *IEEE Trans. Acoust., Speech Signal Process.* ASSP-30, 671–675 (1982).
45. H. Barkhuijsen, R. de Beer, W. M. M. Bovee, and D. van Ormondt, *J. Magn. Reson.* 61, 465–481 (1985).
46. J. Gorcester, S. Rananavare, and J. H. Freed, *J. Chem. Phys.* 90, 5764–5786 (1989).
47. D. J. States, R. A. Haberkorn, and D. J. Ruben, *J. Magn. Reson.* 48, 286–292 (1982).
48. D. I. Hoult and R. E. Richards, *Proc. R. Soc. London, Ser. A* 344, 311 (1975).
49. J. H. Freed, *J. Phys. Chem.* 71, 38–51 (1967).
50. J. Jeener, B. H. Meier, P. Bachmann, and R. R. Ernst, *J. Chem. Phys.* 71, 4546–4553 (1979).
51. S. Macura and R. R. Ernst, *Mol. Phys.* 41, 95–117 (1980).
52. M. P. Eastman, R. G. Kooser, M. R. Das, and J. H. Freed, *J. Chem. Phys.* 51, 2690–2709 (1969).
53. A. E. Stillman and R. N. Schwartz, *J. Magn. Reson.* 22, 269–277 (1976).
54. A. Nayeem, Ph.D. Thesis, Cornell University, Ithaca, NY (1986); A. Nayeem, S. Rananavare, V. S. S. Sastry and J. H. Freed, *J. Chem. Phys.* 91, (1989), (in press).
55. J. S. Hwang, R. P. Mason, L. P. Hwang, and J. H. Freed, *J. Phys. Chem.* 79, 489–511 (1975).
56. J. Yin, M. Pasenkiewicz-Gierula, and J. S. Hyde, *Proc. Natl. Acad. Sci. U.S.A.* 84, 964–968 (1987).
57. J. S. Hyde, in *Time Domain Electron Spin Resonance* (L. Kevan and R. N. Schwartz, eds.), Chapter 1. Wiley (Interscience), New York, 1979.
58. A. F. Mehlkopf, D. Korbee, T. A. Tiggelman, and R. Freeman, *J. Magn. Reson.* 58, 315–323 (1984).
59. G. L. Millhauser, Ph.D. Thesis, Cornell University, Ithaca, NY (1986).
60. D. Gamliel and J. H. Freed, to be published.
61. R. P. J. Merks and R. de Beer, *J. Phys. Chem.* 83, 3319–3322 (1979).
62. P. Höfer, A. Grupp, H. Nebenführ, and M. Mehring, *Chem. Phys. Lett.* 132, 279–282 (1986).
63. R. Brüschweiler, J. C. Madsen, C. Griesinger, O. W. Sørensen, and R. R. Ernst, *J. Magn. Reson.* 73, 380–385 (1987).
64. W. B. Mims, *Rev. Sci. Instrum.* 36, 1472 (1965).
65. B. C. Henderson and J. A. Cook, *Microwave Syst. News* 17, 75 (1987).
66. R. M. Bracewell, *The Fourier Transform and Its Applications*, 2nd ed. McGraw-Hill, New York, 1986.
67. W. B. Mims, in *Electron Paramagnetic Resonance* (S. Geschwind, ed.). Plenum, New York, 1972.
68. B. R. Johnson, Ph.D. Thesis, Cornell University, Ithaca, NY (1984); B. R. Johnson, J. S. Denker, N. Bigelow, L. P. Levy, J. H. Freed, and D. M. Lee, *Phys. Rev. Lett.* 52, 1508–1511 (1984).
69. W. Froncisz and J. S. Hyde, *J. Magn. Reson.* 47, 515 (1982); J. P. Hornak and J. H. Freed, *ibid.* 62, 311–313 (1985).
70. W. Froncisz, private communication.

71. S. Pfenninger, J. Forrer, A. Schweiger, and T. H. Weiland, *Rev. Sci. Instrum.* 59, 752 (1988).
72. R. H. Crepeau, A. Dulcic, J. Gorcester, T. Saarinen, and J. Freed, *J. Magn. Reson.* 84, 184–190 (1989).
73. R. Ernst and W. A. Anderson, *Rev. Sci. Instrum.* 37, 93 (1966).
74. R. Ernst, *Adv. Magn. Reson.* 2, 1 (1966).
75. R. G. Kooser, W. V. Volland, and J. H. Freed, *J. Chem. Phys.* 50, 5243–5257 (1969)
76. M. H. Levitt and R. Freeman, *J. Magn. Reson.* 33, 453 (1979); R. Freeman, S. P. Kempsell, and M. H. Levitt, *ibid.* 38, 473 (1980).
77. C. W. Gear, *Numerical Initial Value Problems in Ordinary Differential Equations.* Prentice-Hall, Englewood Cliffs, NJ, 1971.
78. R. Fletcher, *Practical Methods of Optimization*, Vol. 2. Wiley, New York, 1981.
79. S. M. Kay and S. L. Marple, Jr., *Proc. IEEE* 69, 1380 (1981).
80. G. H. Golub and C. F. van Loan, *Matrix Computations.* Johns Hopkins Univ. Press, Baltimore, Maryland, 1983.
81. H. Barkhuijsen, R. de Beer, and D. van Ormondt, *J. Magn. Reson.* 64, 343 (1985).
82. J. Tang, C. P. Lin, M. K. Bowman, and J. R. Norris, *J. Magn. Reson.* 62, 167 (1985); J. Tang and J. R. Norris, *J. Chem. Phys.* 84, 5210 (1986).
83. G. L. Millhauser, A. A. Carter, D. J. Schneider, J. H. Freed, and R. E. Oswald, *J. Magn. Reson.* 82, 150–155 (1989).